

ARTUR SANTOS MIRANDA

ALTERAÇÕES ELÉTRICAS E TECIDUAIS DURANTE A INFECÇÃO PELO *T. CRUZI* E AVANÇOS COMBINADOS PARA A CARACTERIZAÇÃO FUNCIONAL DAS JUNÇÕES GAP CARDIOVASCULARES E DOS EFEITOS DIRETOS DA HIPERCOLESTEROLEMIA NO CORAÇÃO: ALVOS DE NOVAS FERRAMENTAS PARA O ESTUDO DA DOENÇA DE CHAGAS

Belo Horizonte, Minas Gerais - Brasil

Abril - 2019

ARTUR SANTOS MIRANDA

ALTERAÇÕES ELÉTRICAS E TECIDUAIS DURANTE A INFECÇÃO PELO *T. CRUZI* E AVANÇOS COMBINADOS PARA A CARACTERIZAÇÃO FUNCIONAL DAS JUNÇÕES GAP CARDIOVASCULARES E DOS EFEITOS DIRETOS DA HIPERCOLESTEROLEMIA NO CORAÇÃO: ALVOS DE NOVAS FERRAMENTAS PARA O ESTUDO DA DOENÇA DE CHAGAS

Orientador: Prof. Dr. Jader Cruz

Tese submetida ao Departamento de Bioquímica e Imunologia do Instituto de Ciências Biológicas da Universidade Federal de Minas Gerais, como requisito parcial para a obtenção do grau de Doutor em Bioquímica e Imunologia.

Universidade Federal de Minas Gerais

Belo Horizonte

Abril - 2019

043

Miranda, Artur Santos.

Alterações elétricas e teciduais durante a infecção pelo *T. Cruzi* e avanços combinados para a caracterização funcional das junções GAP cardiovasculares e dos efeitos diretos da hipercolesterolemia no coração: alvos de novas ferramentas para o estudo da doença de Chagas [manuscrito] / Artur Santos Miranda. - 2019.

108 f. : il. ; 29,5 cm.

Orientador: Prof. Dr. Jader Cruz.

Tese (doutorado) - Universidade Federal de Minas Gerais, Instituto de Ciências Biológicas. Departamento de Bioquímica e Imunologia.

1. Bioquímica. 2. Doença de Chagas. 3. Cardiopatias. 4. Miócitos Cardíacos. 5. Junções Comunicantes. 6. Hipercolesterolemia. I. Cruz, Jader dos santos. II. Universidade Federal de Minas Gerais. Instituto de Ciências Biológicas. III. Título.

CDU: 577.1



Universidade Federal de Minas Gerais
 Curso de Pós-Graduação em Biotecnologia e Imunologia ICB/UFMG
 Av. Antônio Carlos, 6627 – Pampulha
 31270-901 – Belo Horizonte – MG
 e-mail: pg-biq@icb.ufmg.br (31)3409-2615



ATA DA DEFESA DA TESE DE DOUTORADO DE ARTUR SANTOS MIRANDA. Aos doze dias do mês de abril de 2019 às 14:00 horas, reuniu-se no Instituto de Ciências Biológicas da Universidade Federal de Minas Gerais, a Comissão Examinadora da tese de Doutorado, indicada *ad referendum* do Colegiado do Curso, para julgar, em exame final, o trabalho intitulado ""Estudo das junções GAP e da Hipercolesterolemia em cardiomiócitos como novas estratégias para a elucidação dos determinantes da disfunção elétrico-metabólica durante a infecção pelo *Trypanosoma cruzi*""", requisito final para a obtenção do grau de Doutor em Ciências: Bioquímica. Abrindo a sessão, o Presidente da Comissão, Prof. Jader dos Santos Cruz, da Universidade Federal de Minas Gerais, após dar a conhecer aos presentes o teor das Normas Regulamentares do Trabalho Final, passou a palavra ao candidato para apresentação de seu trabalho. Seguiu-se a arguição pelos examinadores, com a respectiva defesa do candidato. Logo após a Comissão se reuniu, sem a presença do candidato e do público, para julgamento e expedição do resultado final. Foram atribuídas as seguintes indicações: Dr. Juliane Vasconcellos Joviano dos Santos (Universidade Federal de Minas Gerais), aprovado; Dr. Silvia Carolina Guatimosim Fonseca (Universidade Federal de Minas Gerais), aprovado; Dr. Antonio Nei Santana Gondim (Universidade do Estado da Bahia), aprovado; Dr. Danilo Roman Campos (Universidade Federal de São Paulo), aprovado; Dr. Jader dos Santos Cruz - Orientador (Universidade Federal de Minas Gerais), aprovado. Pelas indicações o candidato foi considerado:


APROVADO
 REPROVADO

O resultado final foi comunicado publicamente ao candidato pelo Presidente da Comissão. Nada mais havendo a tratar, o Presidente da Comissão encerrou a reunião e lavrou a presente Ata que será assinada por todos os membros participantes da Comissão Examinadora. Belo Horizonte, 12 de abril de 2019.


 Dr. Juliane Vasconcellos Joviano dos Santos (UFMG)


 Dr. Silvia Carolina Guatimosim Fonseca (UFMG)


 Dr. Antonio Nei Santana Gondim (Universidade do Estado da Bahia)


 Dr. Danilo Roman Campos (Universidade Federal de São Paulo)


 Dr. Jader dos Santos Cruz - Orientador (UFMG)

APOIO INSTITUCIONAL

Essa tese foi realizada com apoio dos seguintes laboratórios no Instituto de Ciências Biológicas da Universidade Federal de Minas Gerais: Laboratório de Membranas Excitáveis (LAMEX- Prof. Dr. Jader Cruz), Laboratório de Aterosclerose e Bioquímica Nutricional (LABIN- Profa. Dra. Jacqueline Leite); Laboratório de Gnotobiologia (Profa. Dra Leda Quercia Vieira). Também tivemos apoio do Laboratório de Cromatografia Gasosa e Cromatografia Líquida de Alta Eficiência do Departamento de Química da UFMG (Dra. Vany Ferraz). Contamos também com o apoio do Laboratório de CardioBiologia (Prof. Dr. Danilo Roman-Campos), Departamento de Biofísica da Escola Paulista de Medicina, Universidade Federal de São Paulo.

O período de doutorado sanduíche foi realizado na *Univerity of Western Ontario, London - Canada* sob orientação do Prof. Dr. Bai, financiado pela Fundação de Amparo à Pesquisa do Estado de Minas Gerais (FAPEMIG).

Os experimentos envolvendo microscopia foram realizados no Centro de Aquisição e Processamento de Imagens (CAPI), do ICB, UFMG.

Essa tese foi contou com o apoio financeiro das seguintes instituições:

- Fundação de Amparo à Pesquisa do Estado de Minas Gerais (FAPEMIG)
- Conselho Nacional de Desenvolvimento Científico e Tecnológico (CNPq)
- Coordenação de Aperfeiçoamento de Pessoal de Nível Superior (CAPES)

AGRADECIMENTOS

Ao meu orientador Prof. Jader Cruz, por ter me recebido no laboratório, por ter realizado todo o meu treinamento científico, que não apenas me qualificou para defender essa tese de doutorado, mas também garantiu a minha independência para seguir meu caminho como um jovem pesquisador! Agradeço pela confiança depositada em mim, mesmo quando eu não merecia.

Aos amigos ex-colegas de laboratório que acompanharam e influenciaram todo o desenvolvimento da minha carreira científica até o momento, Prof. Antônio Nei, Eduardo Gervasio e Prof. Danilo Roman-Campos. Saibam aprendo e aprendi muito com vocês, e espero que nossos caminhos continuem se tangenciando em colaborações científicas e não científicas também!

A todos os amigos de laboratório pelo apoio científico e também por todos os momentos de alegrias;

A minha família: Minha mãe, Taninha, Meu pai Rafael, minha irmã Mariana pelo investimento moral e financeiro que permitiu a minha formação intelectual e de caráter como cidadão. Obrigado também pela compreensão e carinho, mesmo quando estou chato!

A minha segunda família: Júnia, Jorge, Isabella, Matheus, e Pedro, por terem me acolhido e dado muito apoio e bons exemplos de confiança, carinho e determinação.

A todos os amigos da graduação pela constante amizade, em especial àqueles que sempre estiveram perto, Douglas, Ariane, Camila, André, Thabata, Raffaello. Cada um de vocês marcou minha vida de forma fundamental e complementar, e formaram muitos dos pilares da minha personalidade e valores! Tenho certeza que independentemente de onde estivermos, sempre poderei contar com vocês para tudo, e tenham certeza de que a recíproca é verdadeira! Um agradecimento especial também para Fernanda e Pablo, que foram apoio psicológico fundamental durante a estadia no Canadá! Contem comigo para tudo!

Nick, spending that year in the lab was awesome indeed! I learnt a lot from you: thanks for sharing with me your knowledge on double patch-clamp, cell culture and other lab stuff. Thanks for all the tips about your culture, good deals, good sushi, Barakat, kendo! Thanks for English lessons as well! We became close friends in a short time, and I have no doubts it will last our entire life. I am waiting for you here!

Hong and Dr. Bai, I have no word to describe my gratitude for having me in the lab over the year. Thanks for the patience and support. I certainly learned a lot from both of you! I hope we can meet each other soon

Ao meu amor para toda vida, Julliane. Não tem como descrever em poucas palavras um agradecimento por toda a importância que você teve na minha carreira científica e na minha vida pessoal. Dessa forma

não vou agradecer a nada específico, mas apenas expressar minha gratidão de modo geral, dizer que eu enxergo tudo o que você fez e faz por mim, e lembra-la de que eu sempre estarei aqui para você!

Às Agências de fomento CAPES, FAPEMIG e CNPq, pelo apoio financeiro.

SUMÁRIO

RESUMO	6
ABSTRACT	7
INTRODUÇÃO.....	8
JUSTIFICATIVA.....	24
OBJETIVOS.....	27
CAPÍTULO 1.....	29
CAPÍTULO 2.....	30
CAPÍTULO 3.....	31
DISCUSSÃO.....	32
CONCLUSÕES.....	38
REFERÊNCIAS.....	39

RESUMO

Desde sua identificação em 1909, muitos esforços foram dedicados à caracterização dos mecanismos de infecção, controle do vetor e tratamento dos sintomas da doença de Chagas (DC). Entretanto, após mais de 100 anos, ainda não existe um tratamento antiparasitário eficaz, especialmente na fase crônica da doença. Além disso, a amenização dos sintomas é feita de maneira não específica de acordo com as diretrizes de outras cardiopatias, o que torna ambas as abordagens ineficientes. Considerando a complexidade da DC, estudos envolvendo aspectos isolados da infecção proporcionam pistas importantes para o entendimento da etiologia da DC e seus mecanismos. Entretanto, abordagens integrativas são necessárias para a determinação de estratégias terapêuticas novas e mais acuradas ao tratamento da DC. Nesse trabalho, nós abordamos esses assuntos de acordo com os seguintes objetivos: caracterização da correlação entre remodelamento tecidual e elétrico na DC e a persistência parasitária no tecido. Além disso, estudamos as propriedades funcionais de junções GAP cardíacas, apontando-as como possíveis determinantes na progressão da DC. Finalmente, descrevemos os efeitos diretos da hipercolesterolemia no coração e em cardiomiócitos isolados, com o intuito de se estabelecer uma nova estratégia se investigar os efeitos de dislipidemias na progressão da DC. De maneira conjunta, os resultados apresentados nesse trabalho irão contribuir para a elucidação das propriedades funcionais das junções GAP e dos efeitos diretos da hipercolesterolemia no coração e em cardiomiócitos isolados. Além disso, apontamos novas estratégias que irão contribuir para o entendimento dos mecanismos envolvidos no desenvolvimento da sintomatologia típica da DC, bem como a influência de aspectos nutricionais na progressão dessa doença.

ABSTRACT

Since identification of Chagas Disease (CD) in 1909, a lot of effort was invested into the characterization of DC infection mechanisms, control of parasite vector and treatment of symptoms. However, after more than 100 years, there is still no effective antiparasitic treatment, especially in the chronic phase, and management of symptoms is done unespecifically for cardiomyopathies, which makes both approaches unneffective. Given the complexity of CD, investigating isolated aspects of the infection provides important cues in terms of disease etiology and mechanisms, however, integrated approaches are also necessary in order to evaluate new and more specific therapeutic strategies. In this study, we have attempted to address these issues, according to the following goals: characterization of whether changes in electrical properties of the isolated ventricular myocytes are correlated with tissue remodeling and *T. cruzi* persistence in CD. Besides, we studied functional properties of cardiac and vascular GAP junctions, pointing them as potential target impacting CD output. Finally, we described direct effect of hypercholesterolemia in a murine model, as a new strategy to evaluate effects of dyslipidemias in the development of CD. All together, we the data reported here will contribute to the elucidation of GAP junction functional properties and the direct role of hypercholesterolemia in heart and isolated cardiomyocytes properties. Furthermore, we have pointed new approaches that will contribute to the elucidation of CD symptoms development as well as to the influence of nutritional aspects to this disease in a more comprehensive manner.

INTRODUÇÃO

Propriedades macroscópicas do coração de mamíferos: bomba cardíaca e mecanismos regulatórios do fluxo

O coração de mamíferos é um músculo tetracavitário o qual representa o principal mecanismo gerador do trabalho mecânico envolvido no fluxo da massa de sangue através dos vasos do sistema circulatório^{1, 2}. O processo cíclico associado ao status mecânico de cada câmara do coração desde a contração atrial até o relaxamento ventricular durante cada batimento é denominado ciclo cardíaco. Além disso, a frequência de ciclos cardíacos no intervalo de 1 minuto é denominada frequência cardíaca³.

Por ser um ciclo, o a dinâmica cardíaca pode ser separada em fases de cunho puramente didáticos para melhor apreciação de suas etapas. Como representado na Figura 1, o ciclo cardíaco inicia-se pelo relaxamento dos átrios e ventrículos, causando sua expansão (diástole), que ocorre de maneira concomitante à abertura das valvas atrioventriculares e fechamento das valvas semilunares (A para B). A expansão das câmaras cardíacas leva ao preenchimento com sangue venoso proveniente da circulação sistêmica para o átrio direito e com sangue arterial proveniente da microcirculação pulmonar para o átrio esquerdo. O preenchimento das câmaras ventriculares ocorre predominantemente de maneira passiva pelo fluxo atrioventricular. Entretanto, a contração atrial a seguir (C) provoca aumento na pressão nessa câmara, forçando a ejeção parcial do sangue remanescente, o que permite uma complementação do volume ventricular^{3, 4, 5}.

A contração atrial é sucedida por um período de contração isovolumétrica (de C pra D), na qual ambas as valvas atrioventriculares e semilunares são resistentes ao fluxo sanguíneo, o que impede o refluxo para os átrios. A abertura das valvas semilunares ocorre ao se atingir uma pressão isovolumétrica crítica (D), momento em que se inicia a ejeção da massa de sangue ventricular para a microcirculação (pelo ventrículo direito, através do tronco pulmonar) e para a circulação sistêmica (ventrículo esquerdo, através da aorta). A ejeção do sangue para a circulação é caracterizada por duas fases: uma fase rápida inicial (E), na qual ainda ocorre aumento da pressão intraventricular em função do prosseguimento de sua contração e

redução do volume da câmara. Ocorre em seguida a fase lenta final (F), que se observa relativa redução da pressão intracavitária, em função da redução da massa de sangue que não é compensada pela redução da área interna da câmara. Observem que a definição de pressão é uma força que atua em uma área.

O relaxamento isovolumétrico caracteriza a início da diástole ventricular, no qual o fechamento das valvas atrioventriculares e semilunares (F para A) concomitante à expansão das câmaras cardíacas promove abrupta queda da pressão intracavitária. Com a progressão da diástole, ocorre novamente a abertura das valvas atrioventriculares e preenchimento das câmaras ventriculares^{3, 5} completando um ciclo cardíaco. É importante, nesse ponto, ressaltar o papel primordial das 4 válvulas cardíacas, denominadas semilunares (valva pulmonar e aórtica) e válvulas atrioventriculares (tricúspide e mitral). Essas válvulas regulam a passagem unidirecional do sangue, evitando refluxo para os átrios durante a contração ventricular e dos vasos para os ventrículos durante o período diastólico^{3, 4}.

Diante da explicação acerca do ciclo cardíaco, segue-se a descrição do controle hemodinâmico do fluxo sanguíneo e sua relação com as propriedades contráteis da bomba cardíaca. A esse, ponto, vale ressaltar que a circulação em mamíferos ocorre em sistema fechado, ou seja, com volume circulatório constante, e em regime estacionário com fluxo constante. Esse fluxo é determinado pelo débito cardíaco, definido como o volume de sangue sendo bombeado pelo coração em 1 minuto, e medido como o produto da frequência cardíaca pelo volume sistólico, $DC = VS \times FC$, no qual DC é o débito cardíaco, VS é o volume sistólico e FC, a frequência cardíaca⁶. Tipicamente, o DC se encontra próximo a 5 l/min de sangue, mas em uma situação de aumento de demanda para trocas gasosas e metabólicas, como no caso de exercício físico, processos inflamatórios e infecciosos, trauma, dentre outros, ocorre significativo aumento do DC. Esse aumento inicialmente se deve através da regulação da frequência cardíaca, que pode ocorrer por influência de diversos fatores, sendo os principais moduladores a alteração do tônus adrenérgico/colinérgico pelo sistema nervoso autônomo, bem como do controle da frequência intrínseca sinusal^{3, 5}.

Além do controle do débito cardíaco pela FC, a alteração do volume sistólico é também determinante para o controle do fluxo sanguíneo. O controle do VS, por sua vez, baseia-se em 3 variáveis principais:

- 1- Pré-carga: Caracterizada pelo volume sanguíneo que preenche o ventrículo ao final da contração isovolumétrica. A expansão da câmara cardíaca

ventricular guarda uma relação diretamente proporcional com a força exercida durante a contração, fenômeno que é conhecido como mecanismo (ou lei) de Frank-Starling. A explicação para essa relação baseia-se na melhor orientação dos filamentos contrateis de actina e miosina em função da distensão dos sarcômeros, o que possibilita uma otimização do recrutamento das fibras e conseqüentemente, maior força de contração ⁷. A pré-carga é controlada, por sua vez por mecanismos que interfiram com o retorno venoso para o coração, incluindo alteração da frequência respiratória e volume respiratório, bem como da atividade acessória da musculatura esquelética, com destaque para a musculatura do tríceps sural ^{3, 5, 8, 9}.

2- Pós-carga: A pós-carga é caracterizada como o volume diastólico final, o volume ventricular sanguíneo remanescente após a sístole. É controlada principalmente pela resistência ao fluxo sanguíneo, com participação fisiológica importante da resistência periférica, mas também pode se encontrar alterada em quadros patológicos em que se observa oclusão parcial de vasos principais, como estenose ou aterosclerose ^{3, 5, 8, 9}.

3- Contratilidade celular: A regulação da capacidade contrátil dos cardiomiócitos é complexa e depende da interação entre a excitabilidade e a contração celular, mediada pela sinalização do Ca^{2+} através do acoplamento excitação-contração ^{9, 10, 11}. Diversos fatores contribuem para a regulação desse sistema, dentre os quais podemos citar as condutâncias iônicas que determinam o formato de onda do potencial de ação cardíaco; o conteúdo de Ca^{2+} presente nos estoques celulares do retículo sarcoplasmático e mitocôndria; a regulação da liberação do cálcio desses estoques e a capacidade de interação do Ca^{2+} com os miofilamentos. Todos esses fatores citados são, por sua vez, estritamente regulados por vias de sinalização celular através de modificações pós traducionais que incluem: fosforilação, sumoilação, palmitoilação, ubiquitinação, além de regulação de caráter oxidativo como nitração e oxidação de resíduos ^{8, 9, 10, 11, 12}.

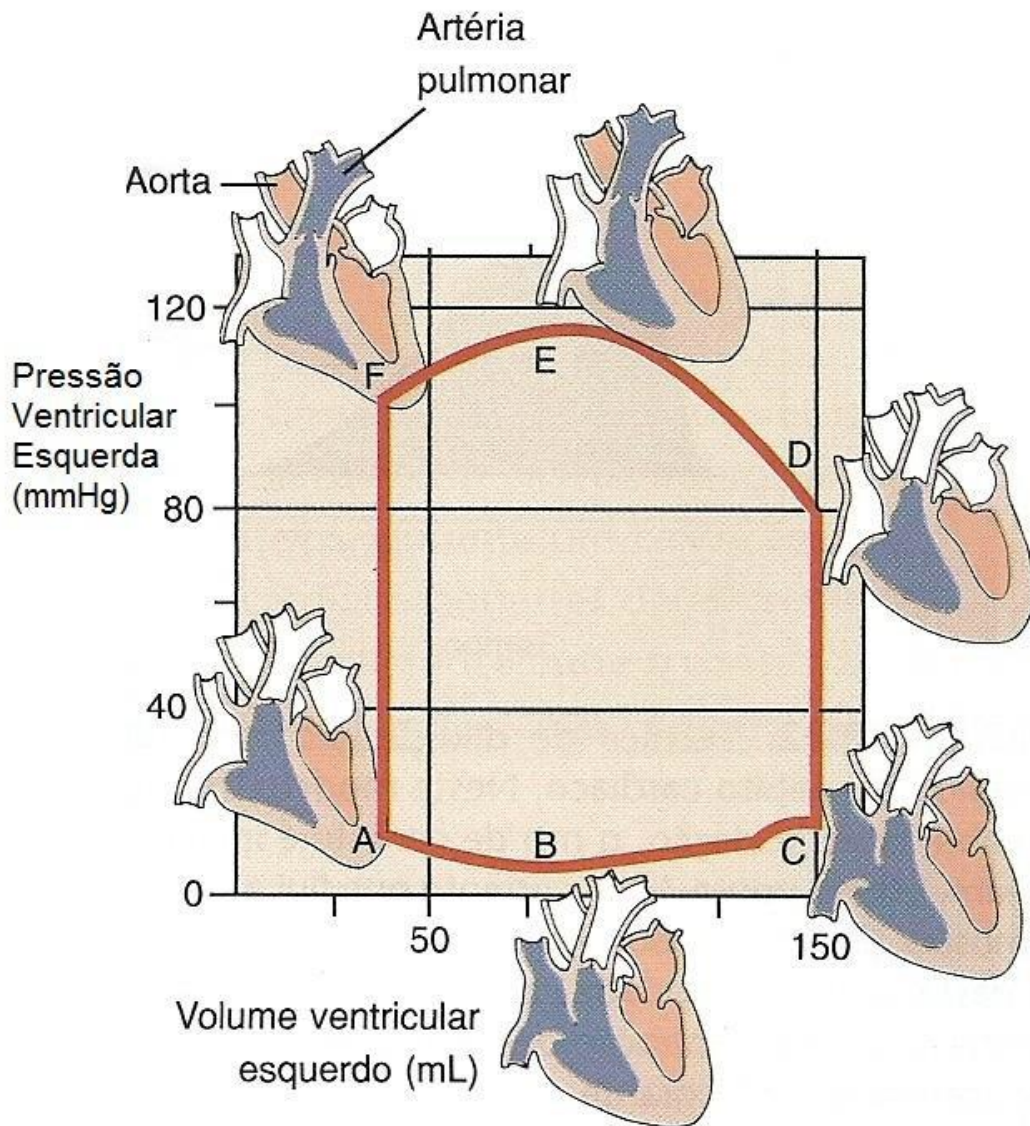


Figura 1: Representação esquemática do ciclo cardíaco, mostrando as alterações de pressão e volume do ventrículo esquerdo durante um único ciclo. Adaptado de Berne et al (2009).

Condução do impulso elétrico no coração

Até o momento foi realizado uma breve introdução sobre a regulação dos aspectos contráteis do coração. O próximo tópico a ser abordado envolve uma descrição da regulação elétrica do coração.

O início do processo de condução do impulso elétrico no coração tem origem através da atividade marca passo de um grupamento de células presentes no nó sino-atrial (NSA). As denominadas células nodais possuem propriedade auto-estimulatórias e são capazes de desencadear potenciais de ação de forma rítmica sem a necessidade de estimulação externa, de modo que a frequência de auto-estimulação dessa região é denominada frequência intrínseca do coração ¹³. O estímulo gerado no NSA é propagado de maneira interatrial até o átrio esquerdo, por meio de um feixe de fibras de condução atrial denominado feixe de Bachman.

Simultaneamente, o estímulo despolarizante é propagado até o nó átrio ventricular (NAV) por meio das vias intermodais, lenta e rápida. O NAV também possui células capacidade auto-estimulatória, com frequência reduzida quando comparada à frequência intrínseca proveniente do NSA, mas que pode servir como marca-passo acessório em caso de falha da capacidade auto-estimulatória sinusal. Em situações fisiológicas, entretanto, a atividade auto-estimulatória atrioventricular é rendida à estimulação atrial ¹³. De maneira importante, ao passar pelo NAV o impulso elétrico sofre um atraso de condução, um importante componente para a sincronização do ciclo cardíaco, pois impede que as contrações atrial e ventricular ocorram simultaneamente, e sim de forma sincronizada ^{4, 13, 14}. O atraso AV é atribuído a diversos fatores: 1- arquitetura geométrica do NAV, com tecidos não condutores que atuam como isolantes da propagação ^{15, 16}, 2- com células de menor tamanho e com estruturação complexa, que aumenta o caminho de condução e o número de junções comunicantes entre as células ¹⁷, 3- redução da expressão de canais para sódio ^{18, 19}, 4- menor acoplamento por meio da natureza e magnitude das junções GAP expressas nessa região ²⁰.

Após atravessar a região AV, o estímulo elétrico é conduzido através do feixe de His, em sua bifurcação esquerda e direita. O feixe de His, por sua vez, também se ramifica formando as fibras de Purkinje, penetrando as paredes do miocárdio, transversalmente do endocárdio ao epicárdio. Nos tecidos adjacentes ao sistema de condução, a propagação do estímulo elétrico é feita célula a célula, a uma velocidade relativamente acelerada (60-80 cm/s), por meio das junções GAP, que serão

discutidas detalhadamente nos próximos tópicos. A magnitude do acoplamento elétrico-metabólico via junções GAP é tal, que se pode afirmar com segurança que, pelo menos sobre o ponto de vista elétrico, o tecido cardíaco funciona com um sincício ²¹.

Aspectos celulares: Excitabilidade, contração e acoplamento elétrico-metabólico intercelular dos cardiomiócitos

A contração do miócito cardíaco e do coração como um todo depende de uma sinalização específica mobilizada pelo íon Ca^{2+} , a qual, a priori, é engatilhada pela excitação elétrica do cardiomiócito, uma variação transitória de seu potencial de membrana. Esse transiente de voltagem que precede a contração celular é denominado potencial de ação (PA).

O PA cardíaco possui um caráter transitório em função do aparecimento de condutâncias iônicas que ocorrem de maneira também transitória. Nesse contexto, os canais iônicos sensíveis à voltagem assumem um papel principal, e mudança de estados para cada isoforma de canais, entre condutor e não condutor da corrente iônica determinam as diferentes fases do PA cardíaco (exceto para células nodais que apresentam particularidades). A Figura 2 mostra as diferentes fases do PA de um cardiomiócito ventricular, e a contribuição dos principais canais iônicos envolvidos nessa etapa.

O PA pode ser didaticamente separado em 4 fases ²². Durante a despolarização da membrana (fase 0) ocorre a ativação dos canais para sódio, Nav1.5, que possuem um sensor de voltagem composto por resíduos de aminoácidos com carga formal positiva (tipicamente argininas) em seus segmentos transmembrana S4. Diante dessa assertiva, fica evidente que para que ocorra a ativação desses canais, deve ocorrer uma alteração da voltagem de repouso da célula, a qual, na ausência de estímulo externo, se mantém estacionária. Esse estímulo pode ser externo, como no caso de miócitos ventriculares, por meio da comunicação através das junções GAP, ou intrínseco da própria célula, como no caso das células marca-passo, pela função de um grupo de canais iônicos específicos, denominados HCN ²³. O PA só é gerado caso a estimulação da célula excitável modifique a voltagem da membrana até um valor crítico, denominado limiar de excitação, que é a voltagem no qual a condutância despolarizante pela ativação dos canais Nav1.5 (para células não nodais) supera a resistência da membrana em retornar ao estado estacionário. Nesse ponto, diz-se que

há um ciclo de retroalimentação positiva para a ativação de Nav1.5, e o PA irá prosseguir sem a necessidade de mais nenhuma perturbação externa da membrana.

A despolarização da célula cardíaca estimula concomitantemente a ativação dos canais para Ca^{2+} e K^+ , porém com cinética mais lenta de ativação. A ativação das correntes de K^+ transientes rápidas (I_{to}) promove o início da repolarização da membrana (fase 1). Entretanto, a abertura dos canais para cálcio tipo-L ($I_{\text{Ca-L}}$) oferece uma resistência à repolarização pelo aparecimento de uma condutância despolarizante, que é observado como uma fase de platô do potencial de membrana (fase 2). A inativação de I_{Ca} em conjunto com a ativação de outros tipos de canais para K^+ , com destaque para a corrente de K^+ retificadora de entrada (I_{K1}), determina finalmente o prosseguimento da repolarização celular (fase 3). A restituição do potencial de repouso do cardiomiócito caracteriza a fase 4, que também tem predominantemente a participação de I_{K1} ^{5, 22}. Ao contrário das condutâncias transitórias em função dos mecanismos de abertura e fechamento (denominados propriedades de *gating*) dos canais iônicos, o potencial de repouso da célula é estacionário e sustentado pela presença dos canais de vazamento, que conduzem Na^+ e K^+ de modo a estabelecer um potencial elétrico da membrana em função do gradiente eletroquímico de ambos os íons. A perpetuação da capacidade excitatória dos cardiomiócitos é garantida ainda pela ação da Na^+/K^+ ATPase, uma proteína transportadora que acopla energia gerada pela quebra de uma molécula de ATP ao transporte de íons Na^+ e K^+ para fora e dentro da célula, respectivamente, contra seu gradiente de concentração, e dessa forma, garantindo a manutenção do gradiente eletroquímico.

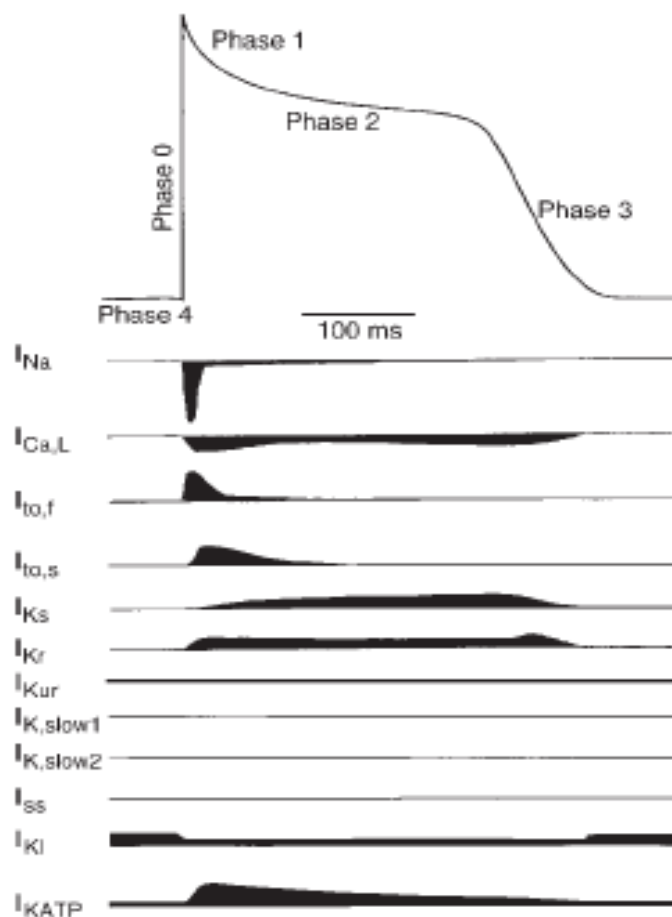


Figura 2: Participação dos diferentes tipos de correntes iônicas na gênese do potencial de ação cardíaco ventricular de humanos. Extraído de Nerbonne & Kass, 2005.

O Ca^{2+} proveniente dos canais tipo-L ativados durante o PA leva por sua vez à ativação de canais presentes na membrana do retículo sarcoplasmático (RS), denominados receptores de rianodina (do inglês *ryanodine receptor*, RyR). Esses canais são seletivos ao Ca^{2+} e também ativados por esse íon, agrupam-se em microrregiões próximas ao fundo das cisternas dos túbulos T, em uma estrutura conhecida como díade^{8, 9, 10}. A ativação dos RyR leva a liberação dos estoques de Ca^{2+} do RS para o citosol de maneira rápida e relativamente sincronizada, garantindo uma rápida difusão para a maquinaria contrátil dessas células. Essa liberação de cálcio induzida pelo cálcio medeia o acoplamento entre a excitabilidade celular e a sua contração, processo denominado acoplamento excitação contração (ECC, do inglês, *excitation contractin coupling*), como representado esquematicamente na

Figura 3.

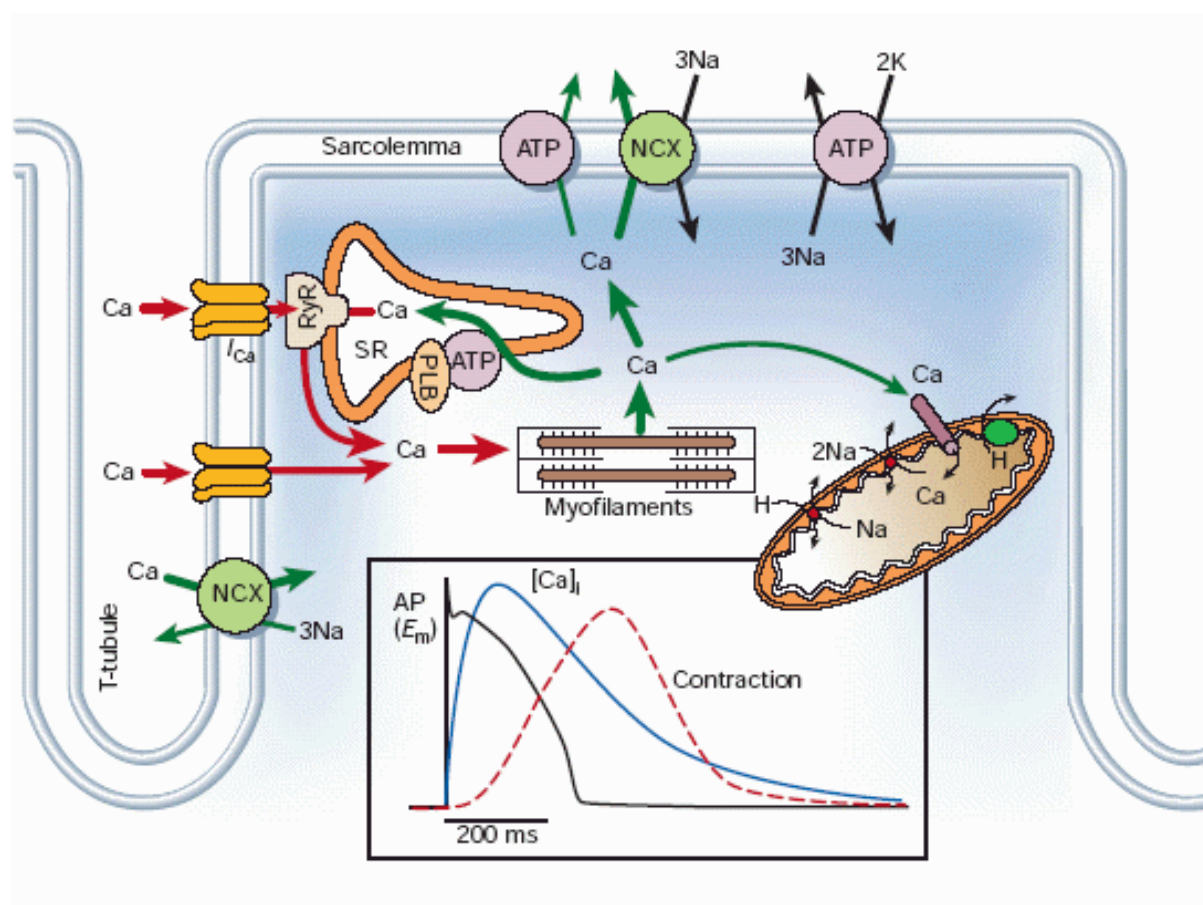


Figura 3: Esquema demonstrando a participação dos principais componentes envolvidos no acoplamento excitação contração, bem como a participação e dinâmica do cálcio nesse processo. Na figura, o componente “ATP” transportando cálcio para fora da célula representa a bomba de cálcio do sarcolema; NCX: trocador $\text{Na}^+/\text{Ca}^{2+}$; ATP/PLB: SERCA associada ao eu peptídeo regulatório, fosfolambam (PLB). Extraído de Bers, 2002.

Após um evento de contração celular ativado pelo Ca^{2+} , os níveis basais desse sinalizador devem ser restaurados, processo que depende dos seguintes sistemas: 1) bomba de Ca^{2+} ATPase do SR (SERCA, do inglês *Sarco-Endoplasmic reticulum calcium*), responsável pela recaptação de Ca^{2+} para o RS; 2) trocador sódio-cálcio presente no sarcolema (NCX, do inglês *sodium calcium exchanger*), 3) bomba de Ca^{2+} ATPase do sarcolema e 4) uniporte de cálcio mitocondrial, como representado na Figura 3. Como descrito anteriormente, a propagação do estímulo elétrico no

coração ocorre através das junções GAP^{24, 25}, canais intercelulares que permitem a passagem de íons e moléculas menores que 1 KDa, normalmente de maneira não seletiva^{26, 27, 28}. Junções GAP são formadas pela associação de dois hemicanais (conexons) presentes, cada um na membrana de uma das células comunicantes. Com representado na Figura 4A, cada um desses canais é formado por um hexâmero de conexinas, proteínas formadas por 4 segmentos transmembrana (M1-M4), dois loops extracelulares (E1-E2), um loop citoplasmático (CL) além das porções N-terminal e C-terminal. Em termos de nomenclatura, conexinas não denominadas pela espécie de origem, bem como pelo peso molecular. Dessa forma, hCx43 determina a conexina (Cx) com 43 KDa humana (h), ou mCx50 representa a conexina com 50 KDa de camundongos (do inglês *mouse*). No genoma humano existem 21 genes para conexinas^{29, 30}, e todas elas apresentam elevado grau de homologia estrutural (70-99% de homologia), tanto entre diferentes conexinas de uma mesma espécie (por exemplo, hCx40 e hCx43) quanto de conexinas análogas de espécies diferentes (como hCx43 e mCx43)³¹.

Cada tipo de conexina é designado pela espécie E1-E2 que forma ligações de hidrogênio com conexinas presentes no conexon adjacente, fornecendo a plataforma de ancoragem das junções GAP^{26, 31, 32}. A estrutura primária desses loops estabelece a compatibilidade entre configurações de conexons capazes ou não de formar junções GAP funcionais⁷. Em termos estruturais (Figura 4B), os conexons podem ser formados por um único tipo de conexina ou por mais de um tipo, formando homômeros ou heterômeros. Quando as junções GAP são formadas por dois conexons homoméricos idênticos, são denominadas homoméricas homotípicas. Como exemplo as junções GAP formadas por miócitos ventriculares, que expressam majoritariamente Cx43^{33, 34}, ou do NAV que expressam tipicamente Cx45^{25, 33}.

Junções GAP formadas por conexons homoméricos, mas com diferentes conexinas entre si são denominados homoméricos heterotípicos. Essa configuração é muito provável entre a comunicação do endotélio que expressam tipicamente Cx40 e Cx37, com células do músculo liso, as quais tipicamente expressam Cx43 e Cx45³⁵. Finalmente as junções formadas por pelo menos um conexon contendo mais de um tipo de conexina são denominadas heteroméricas heterotípicas^{28, 30}. Em termos de organização, junções GAP se organizam em grupamentos contendo vários canais funcionais concentrados em micro domínios da membrana, normalmente associados a

cavéolas ou à domínios ricos em colesterol, ainda que canais isolados, já tenham sido descritos^{36, 37, 38}.

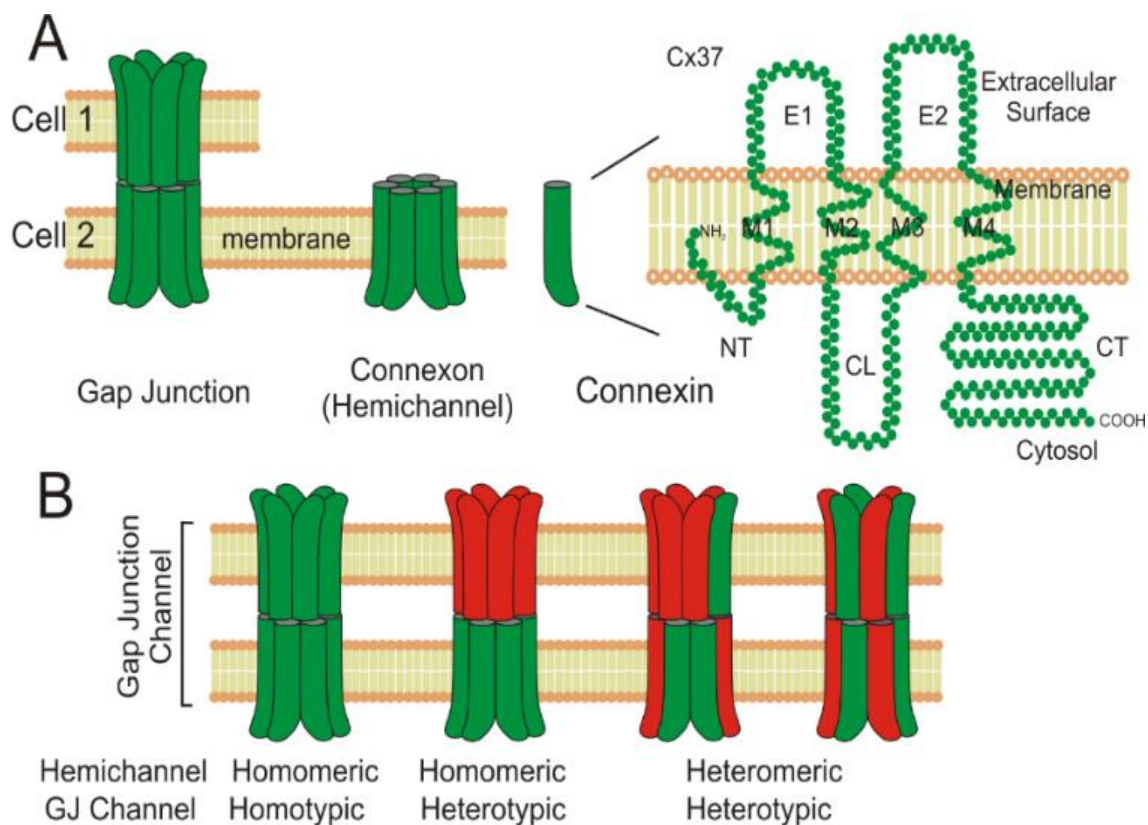


Figura 4: Composição e topologia generalizada das junções GAP (JG), exemplificada por Cx37. (A) Estrutura hierárquica da formação das JG por conexinas (B) Configurações possíveis de JG na membrana. M1-M4- domínios transmembrana; E1/E2- alças extracelulares; CL- alça citoplasmática; NT- domínio N-terminal; CT- domínio C-terminal.

Devido ao seu papel fundamental para a comunicação elétrica e metabólica intercelular, e por serem expressas ubiquamente, alterações na estrutura primária das conexinas são associados a diversas patologias, em sistemas variados. Dentre as principais doenças estudadas, encontra-se catarata, perda de audição congênita, displasia oculodentodigital e fibrilação atrial^{39, 40, 41, 42}. Além disso, conexinas apresentam regulação de sua função em diversos níveis: 1- regulação por voltagem, que provoca a transição do canal de um estado condutor para não condutor, de maneira reversível⁴³,

⁴⁴, 2- regulação por íon divalentes, principalmente Ca^{2+} e Mg^{2+} , normalmente associado à redução transitória da condutância unitária, de maneira dependente de concentração ⁴⁵,
⁴⁶ 3- modificações pós traducionais, principalmente fosforilação ⁴⁷.

Estruturação de microdomínios de membrana: participação do colesterol

Desde a criação do modelo do mosaico fluido por Singer e Nicolson, em 1972 ⁴⁸, já se considerava a assimetria da membrana em termos da composição lipídica e proteica entre as faces interna e externa, propriedades elásticas, capacidade auto-selante e principalmente, a importância da interação com proteínas integrais e acessórias. Entretanto, o modelo original não foi capaz de prever interações lipídeo-lipídeo específicas como geradores de subdomínios dentro da membrana, tampouco a capacidade dessas regiões de interagir e concentrar proteínas, glicoconjugadas de maneira preferencial ⁴⁹. A apreciação da capacidade da membrana em estruturar micro domínios de membrana veio posteriormente ⁵⁰, com a criação das balsas lipídicas ⁵¹, na qual a associação preferencial entre esfingolipídios e colesterol conferia microrregiões com maior resistência à difusão lateral de seus componentes, de modo que proteínas, lipídeos, e glicoconjugados fossem preferencialmente direcionadas a essas regiões.

Balsas lipídicas são pequenos *clusters* (de 10 a 200 nm) constituídos de esfingolipídios (incluindo esfingomielina e glicoesfingolipídeos), colesterol e proteínas especificamente endereçadas a essas regiões ⁵², ⁵³, seja por modificações pós traducionais como acilação ou prenilação, ou por sequências consenso de ligação ao colesterol ⁵³. A presença de esfingolipídios e colesterol confere um elevado caráter apolar a esses microdomínios, de modo que fosfolipídios saturados são preferencialmente associados a essas regiões. Existem diversos tipos de balsas baseado em diferenças de composição lipídica e proteica ⁵⁴, e na capacidade dessas estruturas em agregar-se seletivamente a moléculas sinalizadoras e conseqüentemente determinar uma organização e orientação espacial dos componentes celulares, o que alavancou o estudo das balsas lipídicas nos últimos anos ⁵⁵, ⁵⁶. Particularmente destacam-se as cavéolas como representado na Figura 5.

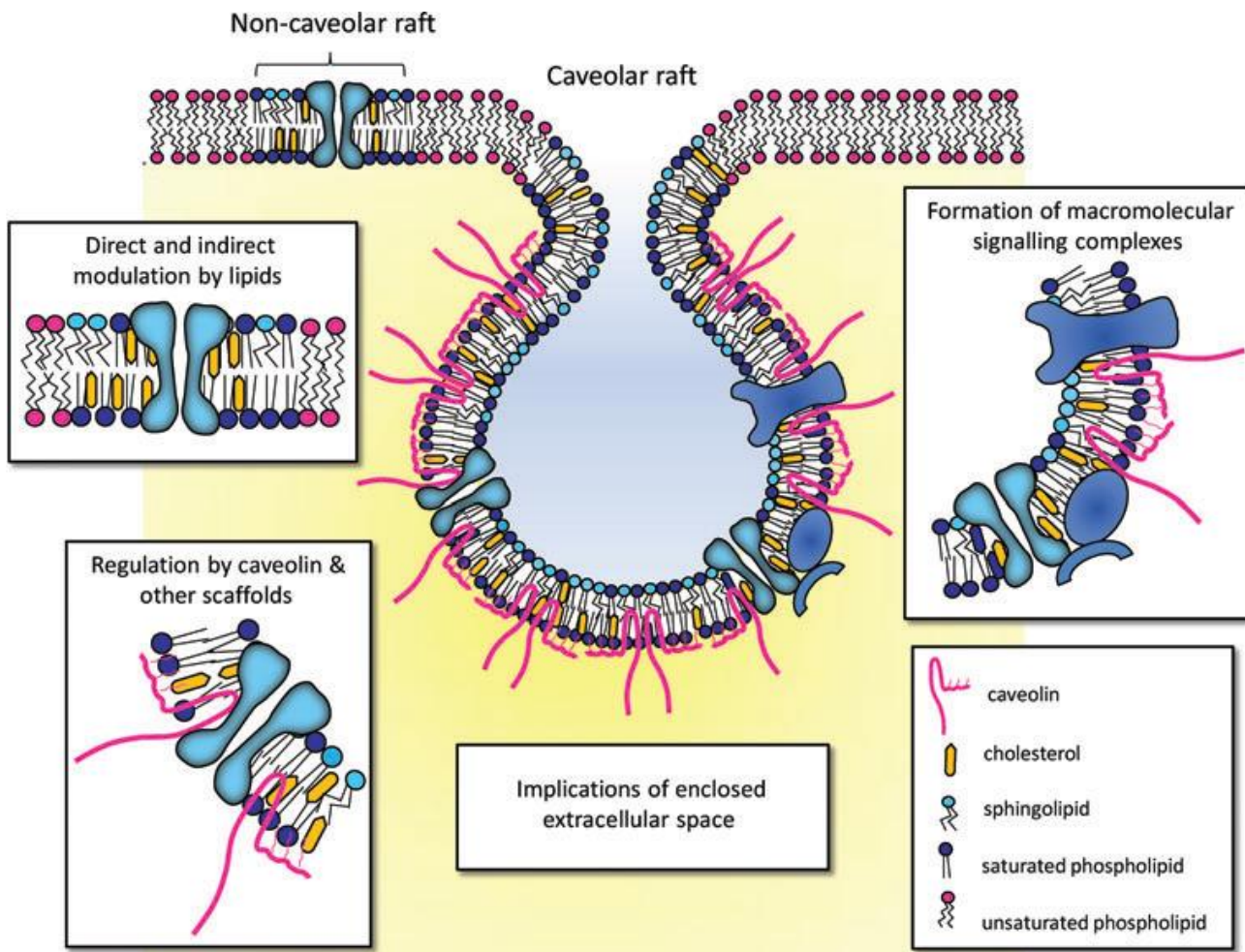


Figura 5: Representação de micro domínios na membrana. Na Figura pode ser observado dois tipos de balsas lipídicas, com a presença ou ausência de interação com caveolinas. É possível observar que balsas lipídicas concentram componentes proteicos e lipídios de maneira seletiva. Extraído de Dart C, 2010.

Diversos canais iônicos, transportadores e outras proteínas envolvidas em vias de sinalização celular foram encontrados concentrados em balsas lipídicas, particularmente em cavéolas, as quais são mais facilmente estudadas. Evidências de diversos componentes envolvidos na morfologia do PA, incluindo o canal para sódio Nav1.5, canal para cálcio Cav1.2, canais para potássio retificadores de entrada Kir2.1,

bem como componentes envolvidos na condução célula a célula cardíaca como conexina-43 já foram encontrados concentrados em cavéolas ^{56, 57, 58}. Não obstante, receptores beta-adrenérgicos responsáveis pela modulação da resposta autonômica simpática no coração também são concentrados nessas estruturas. Finalmente, além da modulação direta dos componentes citados, diversas vias de sinalização celular importantes na regulação dos aspectos eletromecânicos dos cardiomiócitos e do status oxidativo dessas células possuem seus receptores/enzimas incorporados em cavéolas, incluindo a via da proteína cinase A (PKA), proteína cinase C (PKC), fosfatidil-inositol-3- cinase (PI3K)/proteína cinase B (Akt), assim como óxido nítrico sintases (NOS) ⁵⁹.

Doença de Chagas: Disfunções eletro-contráteis em paciente e modelos experimentais

A Doença de Chagas (DC) é uma zoonose transmitida por vetores triatomíneos hematófagos, popularmente conhecidos como barbeiros. Dentre os barbeiros transmissores da doença encontram-se as espécies pertencentes aos gêneros *Triatoma*, *Panstrongylus* e *Rhodinus* (classe Insecta, ordem Hemiptera, família Reduviidae) ⁶⁰. A transmissão do protozoário flagelado *T. cruzi*, agente etiológico da DC, ocorre através da inoculação do parasita pelo contato com fezes infectadas do vetor, principalmente durante seu período de forrageio no hospedeiro. No hospedeiro vertebrado, os parasitas diferenciam-se na forma tripomastigota, capaz de parasitar diferentes células, inclusive cardiomiócitos. No interior das células, eles se diferenciam em amastigotas, iniciando o processo de replicação. Uma nova etapa de diferenciação das formas amastigotas em tripomastigotas conclui o ciclo de parasitismo celular, e as formas tripomastigotas alcançam novamente a corrente sanguínea e/ou interstício através da lise da célula infectada ⁶¹.

A relevância epidemiológica da DC é elevada, principalmente em países nos quais são encontrados os vetores triatomíneos. A DC acomete aproximadamente 8 milhões de pessoas no mundo (OMS *factsheets*, 2018) ⁶², e é um dos maiores contribuintes pelos casos de insuficiência cardíaca na América Latina ^{62, 63, 64}. Além disso, representa uma das patologias mais onerosas dentre as chamadas doenças tropicais negligenciadas ⁶³. Clinicamente, a DC é classificada em duas fases, aguda e crônica, e pode possuir, em ambas as etapas, manifestações de caráter cardíaca,

indeterminada ou do trato digestivo, sendo a forma cardíaca da doença, sua manifestação mais prevalente e severa ⁶⁵. Na fase aguda em geral, a rápida proliferação dos parasitas é acompanhada por uma inflamação sistêmica ^{66, 67}, com infiltrado inflamatório mononuclear, congestão aguda e edema. ⁶⁸. No coração, manifesta-se como uma miocardite aguda, a qual é acompanhada por alterações da função elétrica e contrátil de cardiomiócitos, como reportado em infecções experimentais utilizando modelos murinos da doença ^{69, 70}. O remodelamento celular de cardiomiócitos é tipicamente caracterizado pelo prolongamento do PA, redução na densidade e propriedades de *gating* de canais iônicos, principalmente seletivos para as correntes de potássio e de cálcio ⁷¹. Além disso, a redução das correntes de Ca²⁺ também está relacionada às alterações do manejo intracelular desse íon, bem como disfunções da capacidade contrátil dos cardiomiócitos isolados ^{70, 71, 72}.

Considerando o sistema cardiovascular e seus reguladores, na fase aguda ainda é possível observar uma deservação do sistema autonômico do coração ⁷³. As disfunções elétricas celulares e alteração do tônus autonômico podem determinar o aparecimento de taquicardia e arritmias diversas como alternância de onda P (dissociação atrioventricular), distúrbios de repolarização ⁷⁴, além de marcadores para hipertrofia cardíaca terem sido identificados ⁷². Apesar da diversidade de sintomas explicitados, de forma geral a fase aguda resolve-se após algumas semanas, em função do controle da proliferação do parasita e da resposta imunológica em si pelo hospedeiro. Sabe-se que 30% desses pacientes irão, após um período de 10-30 anos, apresentar novamente os sintomas, agora associados à fase crônica ⁶³. O período entre a fase sintomática aguda e crônica é denominado fase indeterminada, e apesar de sinais clínicos não serem identificados, a presença do parasita pode ser confirmada por métodos sorológicos ou parasitológicos ⁷⁵.

Na fase crônica uma baixa carga parasitária é observada nos pacientes. Entretanto, a sintomatologia é mais severa e limitante para a qualidade de vida dos pacientes. Observa-se a presença de áreas de fibrose no miocárdio e no sistema condutor ^{71, 72, 76, 77}. Nessa fase também ocorrem diversos tipos de arritmias severas e bloqueios de condução ^{78, 79}. Ainda, a cardiopatia dilatada é acompanhada por disfunções sistólicas e diastólicas que finalmente progridem insuficiência cardíaca ^{63, 66}. Em termos celulares, os cardiomiócitos também experimentam distúrbios em sua

função elétrica e contrátil, nas quais alterações na forma de onda do PA, redução da densidade das correntes de Ca^{2+} e K^+ , e redução na capacidade contrátil do cardiomiócito ⁷⁰ são observadas. Não obstante, usando um sistema de infecção *in vitro* em células isoladas, já foi demonstrado uma redução na expressão de Conexina-43, provocando mau funcionamento das junções GAP entre pares de cardiomiócitos, e com isso, gerando os problemas de condução ⁸⁰.

Um aspecto importante da infecção pelo *T. cruzi* é o estresse oxidativo associado ao processo inflamatório durante a infecção. Esse processo determina aumento na taxa de produção de espécies reativas de oxigênio (ROS, do inglês *reactive oxygen species*) e óxido nítrico (NO, do inglês *Nitric Oxide*), como estratégia para se combater a propagação de parasitas ^{81, 82, 83, 84, 85}. Entretanto, tanto ROS quanto NO possuem um caráter sinalizatório importante em cardiomiócitos, regulando a atividade de diversos sistemas da maquinaria celular envolvidas com o controle de suas propriedades elétricas e contráteis ^{12, 86, 87, 88}. Não obstante, o papel de ROS e NO na DC ainda não é bem estabelecido, de modo que sua produção pode ser inclusive importante para a propagação do parasita como reportado anteriormente ⁸⁹.

Finalmente, é importante ressaltar que a forma da DC (cardíaca ou do trato gastrointestinal), bem como a severidade e progressão dos sintomas está intimamente associada à cepa de parasitas infectantes. Diferentes cepas de *T. cruzi* possuem afinidades específicas para determinados órgãos, bem como virulência e taxa de multiplicação características. Além disso, a resposta inflamatória do hospedeiro ainda participa de maneira crucial, tanto para a resolução da doença quanto como potencial amplificador dos danos celulares e estruturais observáveis ⁶⁰.

JUSTIFICATIVA

Desde sua descrição, a Doença de Chagas se tornou foco de esforços coletivos com objetivo de prevenir a infecção, no entendimento da biologia e controle dos vetores invertebrados e no desenvolvimento de estratégias para o tratamento dos sintomas dos pacientes. Essa empreitada coletiva é justificada pelo conjunto de diversos fatores: 1- Alta incidência e prevalência da doença em regiões que hospedam os vetores, como na América Latina, onde constitui uma das principais causas responsáveis pelos casos de insuficiência cardíaca ^{62, 64}. 2- Elevado custo com saúde para o tratamento de pacientes acometidos pela fase crônica e sintomática da doença. De fato, estima-se que a DC tenha custo mundial estimado em 7.19 bilhões de dólares, ~90% desse custo concentrado em regiões endêmicas da doença ⁹⁰. A DC é, portanto, considerada uma das patologias mais onerosas dentre as chamadas doenças tropicais negligenciadas ⁶³. Além disso, pode-se citar: 3- Baixa eficácia dos tratamentos antiparasitários disponíveis, principalmente na fase crônica, pela presença de efeitos colaterais severos ⁹¹. 4- Complexidade do prognóstico e diversidade dos sintomas, principalmente da forma cardíaca da doença. O aparecimento simultâneo de arritmias, disfunções contráteis em um ambiente de alterações metabólicas e inflamatórias dificultam a escolha de um tratamento acurado para a amenização do quadro geral do paciente. Nesse sentido, a caracterização da doença em modelos murinos é uma estratégia importante uma vez que possibilita a avaliação de novas abordagens terapêuticas (considerando o perfil mais acelerado das fases aguda e crônica), bem como amplia o entendimento dos mecanismos associados com a progressão da sintomatologia cardíaca da DC.

Nosso grupo de pesquisa ao longo das décadas de 2000 e 2010 se dedicou à caracterização de modelos murinos para a DC quanto às alterações elétricas, contráteis e do status oxidativo de cardiomiócitos infectados com *T. cruzi*, tanto nas fases aguda quanto crônica da DC ^{70, 71, 72, 92}. Parte dos esforços desse trabalho de doutorado, em alinhamento com o descrito anteriormente, concentraram-se na investigação das disfunções elétricas que acometem o ventrículo direito na progressão entre fase aguda e crônica da DC em modelo murino. Esses trabalhos irão contribuir para o entendimento da correlação entre alterações nas propriedades elétricas de cardiomiócitos com a progressão de alterações estruturais, inflamatórias e da persistência parasitária na DC.

Ainda que os esforços combinados tenham alavancado a caracterização de modelos murinos de infecção experimental com *T. cruzi* e ampliado de maneira geral o entendimento da sintomatologia associada à DC, um aspecto importante da infecção foi negligenciado até o momento, em função da limitação técnica disponível: O estudo do papel das junções GAP na infecção pelo *T. cruzi*. De fato, outros trabalhos reportaram alteração na expressão e distribuição de conexinas no coração durante a DC^{80, 93}. Entretanto, estudos de imageamento e avaliação da expressão por *Western Blot* subestimam as alterações da função das conexinas por desconsiderar a regulação das junções GAP por voltagem e Ca^{2+} , e a influência da atividade desses canais em resposta à modificações pós-traducionais. Nesse sentido, o segundo capítulo desse trabalho de doutorado foi concentrado no aprimoramento técnico para o estudo de junções GAP expressas no coração e no sistema cardiovascular utilizando a técnica de *double patch clamp*. O conjunto de dados dessa seção irão contribuir para a descrição do funcionamento das junções GAP cardiovasculares, em termos de compatibilidade de formação e da regulação desses canais por voltagem. Espera-se que os resultados e experiência obtidos contribuam para a implementação dessa abordagem técnica para o estudo da regulação funcional das junções GAP em modelos de infecção experimental para a DC.

Outra limitação dos modelos experimentais para DC investigados até o momento em nosso grupo de pesquisa negligencia a influência de aspectos ambientais no prognóstico da DC. Particularmente nessa área, desenvolvemos um interesse específico na influência do perfil alimentar como fator crucial para a progressão / resolução dessa patologia. De fato, *T. cruzi* é capaz de invadir diversos tecidos^{94, 95, 96, 97} e sua infecção parecem ser mediadas pelo receptor de LDL⁹⁸. Além disso, já foi reportado que o *T. cruzi* possui elevada afinidade por lipoproteínas^{98, 99}, e que sua infecção está associada ao aumento do conteúdo de colesterol celular¹⁰⁰. Diante do exposto acima, no terceiro capítulo dessa tese, nos dedicamos a estudar a influência da hipercolesterolemia induzida por diet rica em colesterol no conteúdo de colesterol celular e nas propriedades elétricas e contráteis do coração de camundongos e de seus cardiomiócitos isolados. Esses resultados irão contribuir para o entendimento dos efeitos diretos da hipercolesterolemia na função do coração e de cardiomiócitos. Esperamos que esse modelo possa posteriormente ser utilizado em nosso laboratório para o estudo do papel da hipercolesterolemia na infecção experimental pelo *T. cruzi*.

Em conjunto, esperamos que as informações construídas com o estudo de modelos murinos em infecção experimental com *T. cruzi* forneçam pistas importantes para o desenvolvimento de abordagens terapêuticas acuradas para o tratamento da sintomatologia da DC. Essas estratégias poderão, ainda, ser avaliadas nos próprios modelos caracterizados, contribuindo de maneira significativa para o avanço do entendimento da DC.

OBJETIVOS

1-GERAL

O objetivo geral desse trabalho de doutorado foi o desenvolvimento de novas estratégias para o estudo da Doença de Chagas em modelo murino, com ênfase em metodologias para o estudo funcional das junções GAP expressas no sistema cardiovascular e caracterização de um modelo de hipercolesterolemia e seus efeitos diretos na função cardíaca e de cardiomiócitos isolados. Além disso, avaliamos em um modelo de infecção experimental crônica do *T. cruzi*, alterações elétricas de cardiomiócitos isolados e sua relação com alterações adaptativas do ventrículo direito e com a persistência do parasita no coração.

2- ESPECÍFICOS:

Os objetivos específicos serão divididos em 3 capítulos, cada qual, contendo o manuscrito ou artigo publicado referente ao objetivo proposto:

- (Capítulo 1): DISFUNÇÕES ELÉTRICAS, ADAPTAÇÕES MORFOLÓGICAS E PERSISTÊNCIA PARASITÁRIA NO VENTRÍCULO DIREITO DURANTE INFECÇÃO EXPERIMENTAL COM *T. CRUZI*

Objetivo: O objetivo desse trabalho foi avaliar se alterações estruturais progressivas do ventrículo direito entre as fases aguda e crônica se relaciona com a modulação das propriedades elétricas dos cardiomiócitos isolados entre essas duas fases da doença. Além disso, estudar como essas alterações estão relacionadas à persistência do parasita no tecido cardíaco.

- (Capítulo 2): JUNÇÕES GAP E METODOLOGIAS PARA SEU ESTUDO

Objetivo 1: Caracterizar a compatibilidade de formação de junções GAP heterotípicas utilizando conexinas expressas no endotélio e célula muscular lisa. Além disso, caracterizar as propriedades biofísicas de regulação por voltagem dos canais funcionais formados.

Objetivo 2: Investigar a influência da temperatura nas propriedades biofísicas de Junções GAP homotípicas cardíacas, formadas por Cx40 e Cx45: modulação das propriedades cinéticas de desativação e recobro da desativação dos canais e desacoplamento dinâmico.

- (Capítulo 3): EFEITOS DIRETOS DA HIPERCOLESTEROLEMIA NA FUNÇÃO CARDÍACA E DE CARDIOMIÓCITOS

Objetivo: Investigar os efeitos diretos da hipercolesterolemia na modulação no conteúdo de colesterol de cardiomiócitos, bem como da modulação das propriedades contráteis e elétricas do coração e de cardiomiócitos isolados em modelo murino.

Capítulo 1:

DISFUNÇÕES ELÉTRICAS,
ADAPTAÇÕES MORFOLÓGICAS
E PERSISTÊNCIA PARASITÁRIA
NO VENTRÍCULO DIREITO
DURANTE INFECÇÃO
EXPERIMENTAL COM *T. CRUZI*

Altered Cardiomyocyte Function and *Trypanosoma cruzi* Persistence in Chagas Disease

Jader Santos Cruz, Artur Santos-Miranda, Policarpo Ademar Sales-Junior, Renata Monti-Rocha, Paula Peixoto Campos, Fabiana Simão Machado, and Danilo Roman-Campos*

Universidade Federal de Minas Gerais, Minas Gerais, Brazil; Centro de Pesquisas René Rachou, Fundação Oswaldo Cruz (FIOCRUZ), Minas Gerais, Brazil; Escola Paulista de Medicina, Universidade Federal de São Paulo, São Paulo, Brazil

Abstract. Chagas disease, caused by the triatominae *Trypanosoma cruzi*, is one of the leading causes of heart malfunctioning in Latin America. The cardiac phenotype is observed in 20–30% of infected people 10–40 years after their primary infection. The cardiac complications during Chagas disease range from cardiac arrhythmias to heart failure, with important involvement of the right ventricle. Interestingly, no studies have evaluated the electrical properties of right ventricle myocytes during Chagas disease and correlated them to parasite persistence. Taking advantage of a murine model of Chagas disease, we studied the histological and electrical properties of right ventricle in acute (30 days postinfection [dpi]) and chronic phases (90 dpi) of infected mice with the Colombian strain of *T. cruzi* and their correlation to parasite persistence. We observed an increase in collagen deposition and inflammatory infiltrate at both 30 and 90 dpi. Furthermore, using reverse transcriptase polymerase chain reaction, we detected parasites at 90 dpi in right and left ventricles. In addition, we observed action potential prolongation and reduced transient outward K^+ current and L-type Ca^{2+} current at 30 and 90 dpi. Taking together, our results demonstrate that *T. cruzi* infection leads to important modifications in electrical properties associated with inflammatory infiltrate and parasite persistence in mice right ventricle, suggesting a causal role between inflammation, parasite persistence, and altered cardiomyocyte function in Chagas disease. Thus, arrhythmias observed in Chagas disease may be partially related to altered electrical function in right ventricle.

INTRODUCTION

Trypanosoma cruzi, the etiologic agent of Chagas disease, is an important cause of cardiac diseases in Latin America.¹ The onset of Chagas disease is divided in two stages: an acute phase, with high levels of *T. cruzi* in the bloodstream, and a chronic phase, in which the symptoms are observed 10–40 years after the infection, and approximately 20–30% of patients manifest heart conditions including, but not restricted to, heart hypertrophy, heart failure, and cardiac arrhythmias.^{2,3} Changes in heart function is connected to a set of cellular and molecular changes in cardiac tissue such as disrupted myofibrils, increased myocyte apoptosis,⁴ collagen deposition,⁵ oxidative stress,⁶ altered cellular metabolism,⁷ reduced cellular contractility,⁸ and disturbance of electrical properties of the heart.^{9,10} There are distinct hypotheses to explain the molecular mechanisms of altered electrical and contractility properties of the heart during Chagas disease. One of the most accepted explanations claims that chronic cytokine production in the heart is responsible for most of the observed cardiac alterations.^{2,11}

Clinical studies and animal models have shown that right and left ventricles are compromised during the time course of Chagas disease.^{3,8–10,12–15} It is already known that right ventricular function is dysregulated during Chagas disease, however, few studies have pointed out which molecular mechanisms are responsible for right ventricular myocyte dysfunction.^{16,17}

Herein, using a murine model of Chagas disease, we studied whether the changes in electrical properties of the isolated right ventricular myocyte in acute and chronic phases of the disease are correlated with tissue fibrosis, inflammatory infiltrate, and parasite persistence in the heart.

MATERIALS AND METHODS

Mice. Mice were maintained at the Federal University of Minas Gerais (UFMG), Brazil, in accordance with National Institutes of Health guidelines for the care and use of animals. Experiments were performed according to approved protocols from the Institutional Animal Care and Use Committee at UFMG and Federal University of São Paulo.

Mice and parasites. Eight-week-old male C57BL/6 mice were intraperitoneally infected with 50 bloodstream trypomastigote forms of Colombian *T. cruzi* strain,¹⁸ which was maintained by serial passages in mice at the Centro de Pesquisas René Rachou/Fundação Oswaldo Cruz (Belo Horizonte, Brazil).

Histomorphometric analyses. The mice were killed, and hearts were carefully removed and fixed in formalin (10% w/v in isotonic saline). Sections (5 μ m thick) were stained and processed for light microscopic studies and morphometric analysis. Hematoxylin and eosin (HE) was used to count the number of parasite nests/field and quantify inflammatory infiltrates. Picrosirius staining followed by polarized-light microscopy was used to visualize and analyze collagen.¹⁹ Thickness of the right ventricle wall was measured using a magnifier in three different points per ventricular wall from each mouse. All staining was performed in paraffin-embedded heart sections mounted on glass slides. The images were digitized through a JVC TK-1270/JGB microcamera to perform the analysis and transferred to an analyzer (Kontron Elektronik, Munchen, Germany).

Reverse transcriptase polymerase chain reaction. Total RNA was isolated from 50 mg of dissociated left and right ventricular myocytes (see below) from *T. cruzi* infected and control mice, and homogenized in 500 μ L of Trizol reagent (Invitrogen, Carlsbad, CA) according to the manufacturer's instructions. For the reverse transcriptase polymerase chain reaction (RT-PCR), purified RNA (2 μ g) was used to synthesize complementary DNA (cDNA) using a Superscript III (Invitrogen) following the manufacturer's instructions. cDNA was amplified in a PCR using GoTaqGreen Master Mix (Promega, Madison, WI) and 18S ribosomal primers (forward: 5'-TTGTTTGTTGATTCCGTC-3';

*Address correspondence to Danilo Roman-Campos, Departamento de Biofísica, Escola Paulista de Medicina, Universidade Federal de São Paulo, Rua Botucatu 862, Vila Clementino, São Paulo, São Paulo, Brazil, CEP 04023062. E-mail: drcbio@gmail.com

reverse: 5'-CCCAGAACATTGAGGAGCAT-3'). The amplification program was performed in a Eppendorf Mastercycler[®] Nexus (Eppendorf AG, Hamburg, Germany), which included an initial denaturation at 95°C for 2 minutes, followed by 30 cycles of 95°C for 1 minute, 58°C for 1 minute, and 72°C for 30 seconds, with a final extension step at 72°C for 5 minutes. Amplification products were analyzed by electrophoresis in a 2% agarose gel and visualized after staining with GelRed (Biotium Inc., Hayward, CA). A positive result for PCR was the presence of a 200-bp band specific for *T. cruzi*.

Ventricular myocyte isolation. Right and left ventricular cardiomyocytes from age-matched mice were enzymatically isolated as previously described with few modifications.⁸ In brief, the heart was mounted on a homemade Langendorff system, perfused for 5 minutes with calcium-free solution containing (in mM) 130 NaCl, 5.4 KCl, 0.5 MgCl₂, 0.33 NaH₂PO₄, 3 pyruvate, 22 glucose, and 25 4-(2-hydroxyethyl)-1-piperazineethane sulfonic acid (HEPES) (pH set at 7.4). Afterward, the heart was perfused for 10–15 minutes with a solution containing 1 mg/mL collagenase type II (Worthington Biochemical Corp., Lakewood, NJ). The digested heart was then removed from the cannula, and the right and left ventricles was separated and cut into small pieces. Single cells were isolated by mechanical titration and stored in Dulbecco's modified Eagle's medium (Sigma Chemicals Co., St. Louis, MO). Only calcium-tolerant, quiescent, rod-shaped myocytes showing clear cross striations were studied. The isolated cardiac myocytes were used within 4–6 h after enzymatic dispersion.

Electrophysiology. Whole-cell voltage- and current-clamp recordings were obtained using an EPC-9.2 patch-clamp amplifier (HEKA Electronics, Lambrecht [Pfalz], Germany).²⁰ After attaining the whole-cell configuration, 2–5 minutes were allowed to the pipette solution to equilibrate with cellular interior. The experiments were carried out at room temperature (24–27°C). The recording electrodes had resistances of 1–2 MΩ. Current recordings were low-pass filtered (2.9 kHz) and digitized at 5–10 kHz before being stored in a computer. Myocytes showing series resistance (R_s) larger than 10 MΩ were not used in the analysis. R_s compensation was used at 40–70%.

To record action potentials (APs), inwardly rectifying K⁺ current (I_{K1}) and transient outward K⁺ current (I_{to}), the pipette solution was filled with (in mM) 130 K-aspartate, 20 KCl, 10 HEPES, 2 MgCl₂, 5 NaCl, and 5 EGTA, pH set to 7.2 with KOH. We used Tyrode's as bath solution containing (in mM) 140 NaCl, 5.4 KCl, 1 MgCl₂, 1.8 CaCl₂, 10 HEPES, and 10 glucose (pH set at 7.4). After measuring AP and I_{K1} , cardiac myocytes were bathed with recording solution containing 100 μM of Cd²⁺ to block L-type Ca²⁺ current ($I_{Ca,L}$).

We recorded AP until steady-state conditions were achieved. After that 30–50 APs were measured (paced at 1 Hz), and we used the last recorded AP to perform the analysis. We measured the overshoot amplitude, maximal rate of depolarization, and duration at 10%, 50%, and 90% of AP repolarization. I_{K1} was recorded from a holding potential of –40 mV, and then stepped to a set of membrane test potentials (1.5 seconds duration) every 15 seconds between –130 and –40 mV with increments of 10 mV. I_{to} was elicited by depolarization steps from –40 to 70 mV (3 seconds duration) from a holding potential of –80 mV every 15 seconds. We used a 50 ms pre-pulse from –80 to –40 mV to inactivate Na⁺ channels but still were able to record I_{to} .²¹ For measurements of $I_{Ca,L}$, recording pipettes were filled with internal solution containing (in mM) 120 CsCl, 20 tetraethylammonium chloride (TEA-Cl), 5 NaCl, 10 HEPES, 5 Ethylene glycol-bis(2-aminoethylether)-N,N,N',N'-tetraacetic acid (EGTA), pH set to 7.2 with CsOH. $I_{Ca,L}$ was recorded in the presence of 1.8 mM extracellular Ca²⁺. Membrane potential was first stepped from a holding potential of –80 mV to –40 mV for 50 milliseconds (to inactivate Na⁺ channels), and then stepped to different membrane voltages between –40 and 50 mV (300 milliseconds duration). We corrected for junction potential errors (~10 mV) when measuring I_{K1} and I_{to} .

Current–density relationships were fitted using the following equation:

$$I_V = G_{\max} \times \frac{(V_m - E_x)}{1 + \frac{\exp(V_m - V_{0.5})}{S}} \quad (1)$$

where G_{\max} is the maximal conductance; V_m the membrane potential; E_x the electrochemical potential equilibrium for ion x; $V_{0.5}$ the potential in which channels are half activated; S the slope factor.

Statistical analysis. In all experiments, we used 3–5 different hearts. All results are expressed as mean ± standard error of the means, and the number of cells is given as n . Differences between groups were determined using one-way analysis of variance, followed by Bonferroni post hoc test. Differences were considered significant when $P < 0.05$.

RESULTS

Chagas disease causes an increased progression in collagen deposition in both right and left ventricles.^{9,22,23} In a previous study, we have shown that Colombian strain of *T. cruzi* causes marked collagen accumulation in the mice left ventricle.⁹

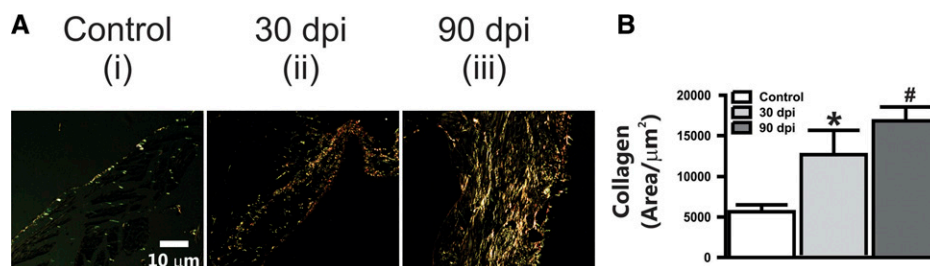


FIGURE 1. Typical histological sections (10 μm, Picosirius staining) of right ventricular tissue. (A) Representative images in (i) control, (ii) 30, and (iii) 90 days postinfection (dpi). (B) Progressive collagen deposition during the time course of Chagas disease. *Control × 30 dpi and #control × 90 dpi, $P < 0.05$.

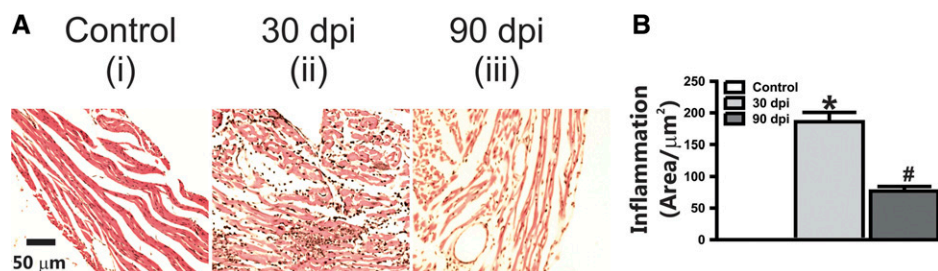


FIGURE 2. Typical histological sections (50 μm , stained with hematoxylin and eosin) of right ventricular tissue. (A) Representative images in (i) control, (ii) 30, and (iii) 90 days postinfection (dpi). (B) Sustained inflammatory infiltrate during *Trypanosoma cruzi* infection during the time course of Chagas disease. *Control \times 30 dpi and #control \times 90 dpi, $P < 0.05$.

As shown in Figure 1A, using Picrosirius staining technique, we detected progressive collagen deposition in right ventricle of infected mice. As depicted in Figure 1B at 30 and 90 days postinfection (dpi), we observed increased collagen deposition $\sim 120\%$ and $\sim 198\%$, respectively. Next, we examined the presence of inflammatory cells in the right ventricle using HE staining. Figure 2A shows typical images of inflammatory cell infiltration in right ventricle. At 30 dpi, an intense inflammatory infiltrate in the right ventricle is noticed when compared with control (Figure 2A and B), which was still observed at 90 dpi indicating a set of chronic inflammation. In addition, we investigated the *T. cruzi* persistence at 90 dpi in the chagasic heart. Using microscopic techniques it was not possible to detect *T. cruzi* nests or isolated parasites in right ventricle (Figure 3A). However, using RT-PCR, we detected ribosomal *T. cruzi* mRNA in both right and left isolated cardiomyocytes at 90 dpi (Figure 4). Interestingly, in this later condition, we verified 23% reduction in the ventricular wall thickness (Figure 3B) in agreement with other study.²⁴

There is compelling evidence in the literature that during the chronic phase of Chagas disease the cardiac tissue presents significant changes in electromechanical properties.^{2,3} However, there is no study correlating inflammation, parasite persistence, and electrical properties of isolated right ventricular myocytes during chagasic cardiomyopathy.⁹ Thus, we used isolated right ventricular myocytes and patch-clamp technique to study the impact of Chagas disease on plasmatic membrane electrical properties.

First, we studied the AP waveform. Figure 5A shows typical AP recordings from isolated cardiac myocytes in control, at 30 dpi, and at 90 dpi. Figure 5B summarizes the results. *Trypanosoma cruzi* infection increased time to action potential repolarization (APR) at both, 30 and 90 dpi. AP duration was increased at 10%, 50%, and 90% of repolarization. Interestingly, as seen in Table 1, no significant

changes in the maximal rate of AP depolarization and overshoot were observed, suggesting no important changes in transient Na^+ current.

The APR is a complex interplay between distinct ionic currents, notably the diversity of voltage-dependent K^+ currents.^{9,25} To investigate the ionic basis to account for AP lengthening, we measured macroscopic outward and inward K^+ currents. Figure 6 shows the results for peak outward K^+ currents, which represent transient outward K^+ current component in cardiomyocytes (I_{to}).²⁶ Figure 6A depicts typical tracings for the outward K^+ current recorded in control, at 30 dpi, and at 90 dpi, respectively. Figure 6B summarizes the results. *Trypanosoma cruzi* infection provoked I_{to} reduction (about 50%) in membrane potentials from 0 to +70 mV. For example, current density (in pA/pF) at +50 mV was 31.9 ± 2.6 (control, $n = 17$), 15.1 ± 1.5 (at 30 dpi, $n = 15$, $P < 0.05$), and 16.9 ± 1.4 (at 90 dpi, $n = 12$, $P < 0.05$). To further investigate the participation of inwardly rectifying K^+ current (I_{K1}), we performed a series of experiments in isolated right ventricle cardiac myocytes during Chagas disease. The results are summarized in Figure 7. Figure 7A shows examples of I_{K1} recordings from control, at 30 dpi, and at 90 dpi. Figure 7B shows the result for sustained component of I_{K1} . Chagasic cardiomyopathy did not change I_{K1} in right ventricular myocytes.

It is well known that during the chronic phase of Chagas disease, electrical and mechanical remodeling of cardiac myocytes occurs.^{3,8-10} In ventricular cardiomyocytes, $I_{\text{Ca,L}}$ is a key player, integrating electrical with mechanical properties.²⁷ Thus, we evaluated whether $I_{\text{Ca,L}}$ was modified in right

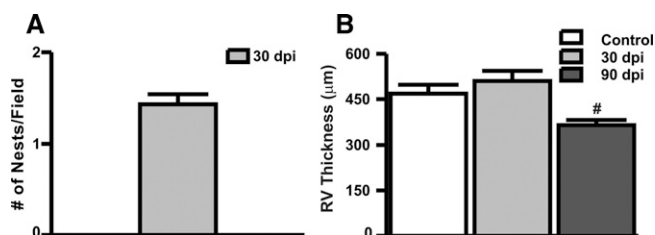


FIGURE 3. Right ventricular parameters during *Trypanosoma cruzi* infection. (A) Number of *T. cruzi* nest/field in right ventricle in the acute phase. (B) Right ventricular thickness.

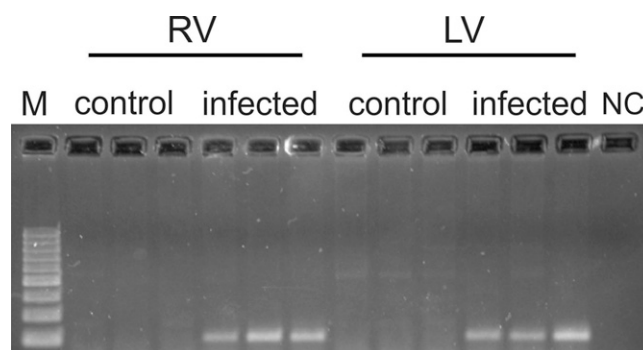


FIGURE 4. Reverse transcriptase polymerase chain reaction (RT-PCR) detection of *Trypanosoma cruzi* in mice cardiac tissue. PCR amplification of a 200-bp fragment represents a positive assay. LV = left ventricle; M = molecular weight marker (100 bp DNA ladder); NC = negative control (without sample); RV = right ventricle.

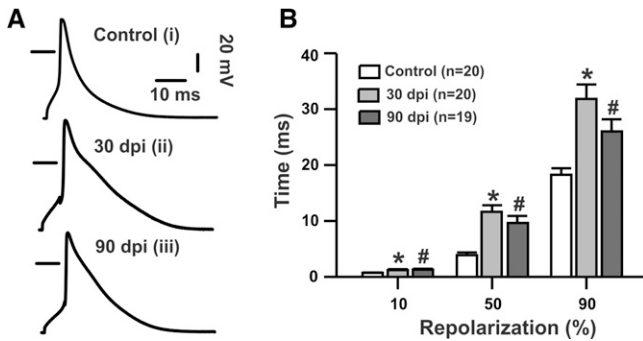


FIGURE 5. Prolonged action potential (AP) from right ventricular myocytes in Chagas disease. (A) Typical AP traces for (i) control, (ii) 30, and (iii) 90 days postinfection (dpi). Marks represent 0 mV. (B) Bar graphs comparing AP repolarization time at different repolarization levels. Control is marked with white bars, 30 dpi with light gray bars, and 90 dpi with dark gray bars. *n* = number of cells. *Control × 30 dpi and #control × 90 dpi, *P* < 0.05.

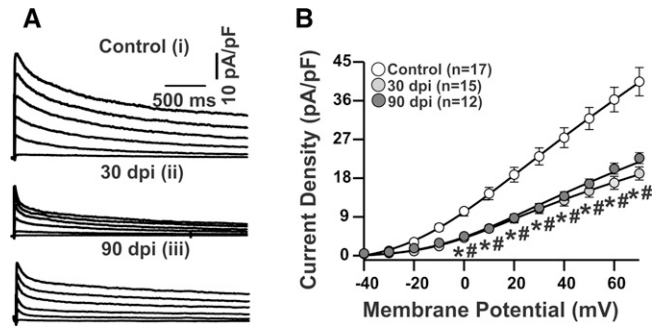


FIGURE 6. Reduced outward K⁺ current (*I*_{to}) in right ventricular myocytes. (A) Representative outward K⁺ current recordings from (i) control, (ii) 30, and (iii) 90 days postinfection (dpi). (B) Voltage dependence of *I*_{to} is plotted as current density (pA/pF) from -40 to +70 mV. Control is marked with white circle, 30 dpi with light gray circles, and 90 with dpi dark gray circles. Lines were fitted according to equation 1. *n* = number of cells. *Control × 30 dpi and #control × 90 dpi, *P* < 0.05.

ventricular myocytes during Chagas disease. Figure 8A represents recordings for *I*_{Ca,L} measured in isolated right ventricular myocytes in control, at 30 dpi, and at 90 dpi. As shown in Figure 8B, *T. cruzi* infection significantly reduced *I*_{Ca,L}.

DISCUSSION

Chagas disease is a serious health problem, especially in Latin American countries. Despite of great efforts in the last century, many aspects of Chagas disease are still unknown.² Clinical studies have described impaired electromechanical properties in chagasic hearts.^{3,28,29} A number of hypotheses were proposed to better explain the clinical phenotype observed in chagasic patients. Two of them are generally accepted based on the relationship between parasite and host. The first puts forward a pivotal role of parasite's persistence to drive chronic inflammation in heart tissue as the major cause of cardiovascular pathology. The second accepted hypothesis postulates that an autoimmune response against self-antigens is responsible for the tissue damage observed in affected organs of chagasic individuals.

In our model, we observed the presence of *T. cruzi* nests in the right ventricular wall of the heart at 30 dpi. More important, at 90 dpi, using RT-PCR, we were able to detect the presence of *T. cruzi* in isolated cardiomyocyte in both right and left ventricles. These results firmly suggest that, in our model, parasite persistence is responsible for chronic inflammation. It is interesting to note, however, that most of the previous studies detected *T. cruzi* in cardiac tissue and not in isolated cardiomyocytes.^{30,31} Here, we detected the presence of *T. cruzi* in isolated cardiomyocytes, which

strongly indicates that parasites are present in cardiomyocyte cells. However, we cannot completely rule out the presence of infected cells isolated along with cardiomyocytes during the enzymatic dissociation of the heart.

In the context of cellular and molecular mechanisms involved in the cardiovascular physiopathology of Chagas disease, most studies have been focused on the left side of the heart. However, many reports in the literature, in both humans and animal models, observed changes in the physiology of the right side of the heart, implying right ventricle as an important player in the development of chagasic cardiomyopathy.^{13,14,24} Various studies demonstrated right branch block, dilated right ventricular chamber, compromised right ventricular myocyte contractility, and thinning of the right ventricular wall even in the absence of left ventricle remodeling, indicating a primary involvement of right ventricle in chagasic cardiomyopathy. However, there is no clear consensus in the literature.¹⁵ Thus, apparently the initial and/or later involvement of right ventricular chamber in chagasic cardiomyopathy progression may depend on the genetic background of the host and/or strain of *T. cruzi* causing the infection.³² Clearly, more studies are necessary to draw a more conclusive opinion about this issue.

TABLE 1
AP parameters

	dV/dt (mV/ms)	Overshoot (mV)	Capacitance (pF)
Control	238.1 ± 14.6 (n = 20)	49.17 ± 1.52 (n = 20)	127.1 ± 7.5 (n = 29)
30 dpi	225.9 ± 17.2 (n = 20)	55.21 ± 2.24 (n = 20)	120.8 ± 6.4 (n = 30)
90 dpi	202.3 ± 11.8 (n = 19)	43.63 ± 1.72 (n = 19)	142.0 ± 7.8 (n = 24)

AP = action potential; dpi = days postinfection.

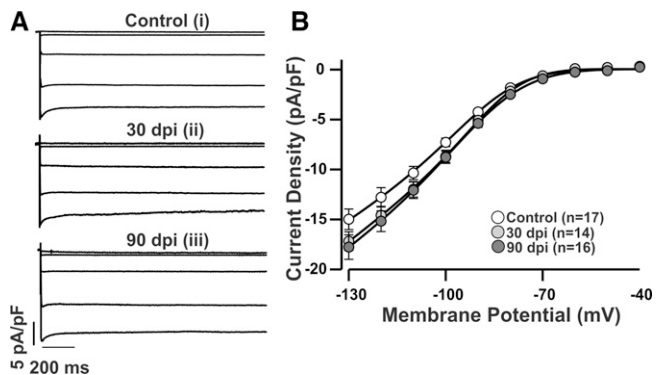


FIGURE 7. Inward K⁺ current (*I*_{K1}) is not altered in right ventricular myocytes. (A) Representative *I*_{K1} recordings from (i) control, (ii) 30, and (iii) 90 days postinfection (dpi). (B) Voltage dependence of *I*_{K1} is plotted as current density (pA/pF) from -130 to +40 mV. *n* = number of cells. Control is marked with white circle, 30 dpi with light gray circles, and 90 dpi with dark gray circles.

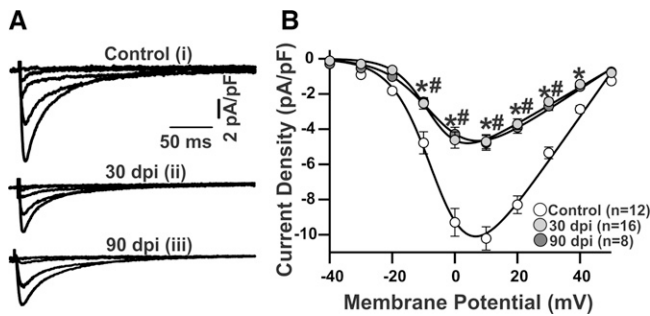


FIGURE 8. Altered L-type Ca^{2+} current ($I_{Ca,L}$) in Chagas disease. (A) Representative $I_{Ca,L}$ recordings from (i) control, (ii) 30, and (iii) 90 days postinfection (dpi). (B) Voltage dependence of $I_{Ca,L}$ is plotted as current density (pA/pF) from -40 to $+50$ mV. Control is marked with white circle, 30 dpi with light gray circles, and 90 dpi with dark gray circles. Lines were fitted according to equation 1. n = number of cells *Control \times 30 dpi and #control \times 90 dpi, $P < 0.05$.

Our results show that *T. cruzi* leads to significant alterations in AP waveform of right ventricular myocytes in acute and chronic phases. Put in perspective, we may suggest that analogous mechanisms cause AP changes in both right and left ventricle myocytes.^{9,10} We previously found increased levels of transforming growth factor beta (TGF- β) and tumor necrosis factor alpha (TNF- α) in the myocardium and bloodstream of infected mice during acute and chronic phases.^{8,9} TNF- α and TGF- β were previously demonstrated as modulators of ionic currents in cardiomyocytes. It is known that TNF- α downregulates I_{to} in cardiomyocytes, through a mechanism dependent on nitric oxide and/or superoxide production.³³ Thus, TNF- α could be responsible for I_{to} current density attenuation in right ventricular myocytes, which might explain the delay in the APR. Hence, reducing TNF- α in the myocardial tissue would restore AP profile in the right ventricular myocytes. However, this hypothesis still needs to be evaluated.

In this model, robust attenuation of $I_{Ca,L}$ was observed. In the context of right ventricular myocytes physiology, $I_{Ca,L}$ is critical to link electrical and mechanical functions. Thus, reduction of $I_{Ca,L}$ could be responsible for the uncoupling of electromechanical function in right ventricular myocytes, contributing to arrhythmogenesis, a common cause of death in chagasic patients. Indeed, an attractive mechanism, one would argue, is that by recovering $I_{Ca,L}$ current density would reduce cardiac arrhythmias propensity contributing, therefore, to a better prognosis in the chronic phase of chagasic cardiomyopathy.⁸ It is important to point out that there are other possible factors involved in altered electrical properties of right ventricular myocytes. Accordingly, *T. cruzi* infection increases expression of β -adrenergic¹⁶ and muscarinic receptors,³⁴ which are known to modulate ionic currents in ventricular myocytes.

Taking together, to our knowledge this study is the first to directly associate parasite persistence, inflammation, and electrical disturbances in the right ventricle of *T. cruzi*-infected mice. Thus, targeting key cytokines (e.g., TNF- α , TGF- β) may have clinical and therapeutic implications during the development of heart malfunction in Chagas disease.

Received March 31, 2015. Accepted for publication January 28, 2016.

Published online March 14, 2016.

Financial support: This study was financially supported by CNPq (grant no. 404353/2012-6) and FAPESP (grant no. 2014/09861-1).

Authors' addresses: Jader Santos Cruz, Artur Santos-Miranda, Renata Monti-Rocha, and Fabiana Simão Machado, Departamento de Bioquímica e Imunologia, Instituto de Ciências Biológicas, Universidade Federal de Minas Gerais, Minas Gerais, Brazil, E-mails: jrcruz@icb.ufmg.br, santosmirandaa.edu@gmail.com, mrrenata@gmail.com, and machadofs@gmail.com. Policarpo Ademar Sales-Junior, Laboratório de Parasitologia Celular e Molecular, Centro de Pesquisas René Rachou, Fundação Oswaldo Cruz (FIOCRUZ), Minas Gerais, Brazil, E-mail: policarpoasjunior@yahoo.com.br. Paula Peixoto Campos, Departamento de Patologia Geral, Instituto de Ciências Biológicas, Universidade Federal de Minas Gerais, Minas Gerais, Brazil, E-mail: paulapet2003@yahoo.com.br. Danilo Roman-Campos, Departamento de Biofísica, Escola Paulista de Medicina, Universidade Federal de São Paulo, São Paulo, Brazil, E-mail: drcbio@gmail.com.

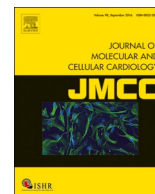
REFERENCES

1. WHO, 2010. *Factsheet on Chagas Disease*. Geneva, Switzerland: World Health Organization.
2. Marin-Neto JA, Cunha-Neto E, Maciel BC, Simoes MV, 2007. Pathogenesis of chronic Chagas heart disease. *Circulation* 115: 1109–1123.
3. Dias E, Laranja FS, Miranda A, Nobrega G, 1956. Chagas' disease: a clinical, epidemiologic, and pathologic study. *Circulation* 14: 1035–1060.
4. Tostes S Jr, Bertulucci Rocha-Rodrigues D, de Araujo Pereira G, Rodrigues V Jr, 2005. Myocardiocyte apoptosis in heart failure in chronic Chagas' disease. *Int J Cardiol* 99: 233–237.
5. Kumar R, Kline IK, Abelmann WH, 1969. Experimental *Trypanosoma cruzi* myocarditis: relative effects upon the right and left ventricles. *Am J Pathol* 57: 31–48.
6. Wen JJ, Vyatkina G, Garg N, 2004. Oxidative damage during chagasic cardiomyopathy development: role of mitochondrial oxidant release and inefficient antioxidant defense. *Free Radic Biol Med* 37: 1821–1833.
7. Vyatkina G, Bhatia V, Gerstner A, Papaconstantinou J, Garg N, 2004. Impaired mitochondrial respiratory chain and bioenergetics during chagasic cardiomyopathy development. *Biochim Biophys Acta* 1689: 162–173.
8. Roman-Campos D, Duarte HL, Sales PA Jr, Natali AJ, Ropert C, Gazzinelli RT, Cruz JS, 2009. Changes in cellular contractility and cytokines profile during *Trypanosoma cruzi* infection in mice. *Basic Res Cardiol* 104: 238–246.
9. Roman-Campos D, Sales-Junior P, Duarte HL, Gomes ER, Lara A, Campos P, Rocha NN, Resende RR, Ferreira A, Guatimosim S, Gazzinelli RT, Ropert C, Cruz JS, 2013. Novel insights into the development of chagasic cardiomyopathy: role of PI3Kinase/NO axis. *Int J Cardiol* 167: 3011–3020.
10. Roman-Campos D, Sales-Junior P, Duarte HL, Gomes ER, Guatimosim S, Ropert C, Gazzinelli RT, Cruz JS, 2013. Cardiomyocyte dysfunction during the chronic phase of Chagas disease. *Mem Inst Oswaldo Cruz* 108: 243–245.
11. Cunha-Neto E, Bilate AM, Hyland KV, Fonseca SG, Kalil J, Engman DM, 2006. Induction of cardiac autoimmunity in Chagas heart disease: a case for molecular mimicry. *Autoimmunity* 39: 41–54.
12. Pereira Barretto AC, Mady C, Arteaga-Fernandez E, Stolf N, Lopes EA, Higuchi ML, Bellotti G, Pileggi F, 1986. Right ventricular endomyocardial biopsy in chronic Chagas' disease. *Am Heart J* 111: 307–312.
13. Carrasco HA, Medina M, Inglessis G, Fuenmayor A, Molina C, Davila D, 1983. Right ventricular function in Chagas disease. *Int J Cardiol* 2: 325–338.
14. Marin-Neto JA, Marzullo P, Sousa AC, Marcassa C, Maciel BC, Iazigi N, L'Abbate A, 1988. Radionuclide angiographic evidence for early predominant right ventricular involvement in patients with Chagas' disease. *Can J Cardiol* 4: 231–236.
15. Nunes Mdo C, Barbosa Mde M, Brum VA, Rocha MO, 2004. Morphofunctional characteristics of the right ventricle in Chagas' dilated cardiomyopathy. *Int J Cardiol* 94: 79–85.
16. Chen G, Barr S, Walsh D, Rohde S, Brewer A, Bilezikian JP, Wittner M, Tanowitz HB, Morris SA, 1996. Cardioprotective

- actions of verapamil on the beta-adrenergic receptor complex in acute canine Chagas' disease. *J Mol Cell Cardiol* 28: 931–941.
17. Souza AP, Jelicks LA, Tanowitz HB, Olivieri BP, Medeiros MM, Oliveira GM, Pires AR, Santos AM, Araujo-Jorge TC, 2010. The benefits of using selenium in the treatment of Chagas disease: prevention of right ventricle chamber dilatation and reversion of *Trypanosoma cruzi*-induced acute and chronic cardiomyopathy in mice. *Mem Inst Oswaldo Cruz* 105: 746–751.
 18. Federici EE, Abelmann WH, Neva FA, 1964. Chronic and progressive myocarditis and myositis in C3h mice infected with *Trypanosoma cruzi*. *Am J Trop Med Hyg* 13: 272–280.
 19. Junqueira LC, Junqueira LC, Brentani RR, 1979. A simple and sensitive method for the quantitative estimation of collagen. *Anal Biochem* 94: 96–99.
 20. Hamill OP, Marty A, Neher E, Sakmann B, Sigworth FJ, 1981. Improved patch-clamp techniques for high-resolution current recording from cells and cell-free membrane patches. *Pflugers Arch* 391: 85–100.
 21. Roman-Campos D, Duarte HL, Gomes ER, Castro CH, Guatimosim S, Natali AJ, Almeida AP, Pesquero JB, Pesquero JL, Cruz JS, 2010. Investigation of the cardiomyocyte dysfunction in bradykinin type 2 receptor knockout mice. *Life Sci* 87: 715–723.
 22. Prado CM, Celes MR, Malvestio LM, Campos EC, Silva JS, Jelicks LA, Tanowitz HB, Rossi MA, 2012. Early dystrophin disruption in the pathogenesis of experimental chronic Chagas cardiomyopathy. *Microbes Infect* 14: 59–68.
 23. Jelicks LA, Shirani J, Wittner M, Chandra M, Weiss LM, Factor SM, Bekirov I, Braunstein VL, Chan J, Huang H, Tanowitz HB, 1999. Application of cardiac gated magnetic resonance imaging in murine Chagas' disease. *Am J Trop Med Hyg* 61: 207–214.
 24. Chandra M, Tanowitz HB, Petkova SB, Huang H, Weiss LM, Wittner M, Factor SM, Shtutin V, Jelicks LA, Chan J, Shirani J, 2002. Significance of inducible nitric oxide synthase in acute myocarditis caused by *Trypanosoma cruzi* (Tulahuen strain). *Int J Parasitol* 32: 897–905.
 25. Nerbonne JM, Kass RS, 2005. Molecular physiology of cardiac repolarization. *Physiol Rev* 85: 1205–1253.
 26. Xu H, Guo W, Nerbonne JM, 1999. Four kinetically distinct depolarization-activated K⁺ currents in adult mouse ventricular myocytes. *J Gen Physiol* 113: 661–678.
 27. Bers DM, 2008. Calcium cycling and signaling in cardiac myocytes. *Annu Rev Physiol* 70: 23–49.
 28. Ribeiro AL, Marcolino MS, Prineas RJ, Lima-Costa MF, 2014. Electrocardiographic abnormalities in elderly Chagas disease patients: 10-year follow-up of the Bambui Cohort Study of Aging. *J Am Heart Assoc* 3: e000632.
 29. Nunes Mdo C, Rocha MO, Ribeiro AL, Colosimo EA, Rezende RA, Carmo GA, Barbosa MM, 2008. Right ventricular dysfunction is an independent predictor of survival in patients with dilated chronic Chagas' cardiomyopathy. *Int J Cardiol* 127: 372–379.
 30. Caldas S, Caldas IS, Diniz Lde F, Lima WG, Oliveira Rde P, Cecilio AB, Ribeiro I, Talvani A, Bahia MT, 2012. Real-time PCR strategy for parasite quantification in blood and tissue samples of experimental *Trypanosoma cruzi* infection. *Acta Trop* 123: 170–177.
 31. Marcon GE, de Albuquerque DM, Batista AM, Andrade PD, Almeida EA, Guariento ME, Teixeira MA, Costa SC, 2011. *Trypanosoma cruzi*: parasite persistence in tissues in chronic chagasic Brazilian patients. *Mem Inst Oswaldo Cruz* 106: 85–91.
 32. Andrade SG, 1990. Influence of *Trypanosoma cruzi* strain on the pathogenesis of chronic cardiomyopathy in mice. *Mem Inst Oswaldo Cruz* 85: 17–27.
 33. Fernandez-Velasco M, Ruiz-Hurtado G, Hurtado O, Moro MA, Delgado C, 2007. TNF-alpha downregulates transient outward potassium current in rat ventricular myocytes through iNOS overexpression and oxidant species generation. *Am J Physiol Heart Circ Physiol* 293: H238–H245.
 34. Peraza-Cruces K, Gutierrez-Guedez L, Castaneda Perozo D, Lankford CR, Rodriguez-Bonfante C, Bonfante-Cabarcas R, 2008. *Trypanosoma cruzi* infection induces up-regulation of cardiac muscarinic acetylcholine receptors in vivo and in vitro. *Braz J Med Biol Res* 41: 796–803.

Capítulo 2:

JUNÇÕES GAP E
METODOLOGIAS PARA SEU
ESTUDO



Heterotypic docking compatibility of human connexin37 with other vascular connexins

Nicholas K. Kim^a, Artur Santos-Miranda^a, Honghong Chen^a, Hiroshi Aoyama^b, Donglin Bai^{a,*}

^a Department of Physiology and Pharmacology, University of Western Ontario, London, Ontario, Canada

^b Graduate School of Pharmaceutical Sciences, Osaka University, Osaka, Japan

ARTICLE INFO

Keywords:

Gap junction channel
Heterotypic docking compatibility
Vasculature
Myoendothelial junction

ABSTRACT

Human vascular connexins (Cx37, Cx40, Cx43, and Cx45) can form various types of gap junction channels to synchronize vasodilation/constriction to control local circulation. Most of our knowledge on heterotypic gap junctions of these vascular connexins was from studies on rodent connexins. In human vasculature, the same four homolog connexins exist, but whether these human connexins can form heterotypic GJs as those of rodents have not been fully studied. Here we used in vitro expression system to study the coupling status and GJ channel properties of human heterotypic Cx37/Cx40, Cx37/Cx43, and Cx37/Cx45 GJs. Our results showed that Cx37/Cx43 and Cx37/Cx45 GJs, but not Cx37/Cx40 GJs, were functional and each with unique rectifying channel properties. The failure of docking between Cx37 and Cx40 could be rescued by designed Cx40 variants. Characterization of the heterotypic Cx37/Cx43 and Cx37/Cx45 GJs may help us in understanding the intercellular communication at the myoendothelial junction.

1. Introduction

Gap junction (GJ) channels provide direct passages for ions, metabolites, and small signaling molecules < 1 kDa in size between two adjacent cells [1–3]. GJ channels are formed from two properly docked hemichannels (or connexons), each of which is a hexamer of connexins [4,5]. There are 21 connexin genes in the human genome (20 connexin genes in the mouse genome) encoding different connexins which are commonly expressed in tissue-specific manner [4,6]. All connexins are predicted to have a similar topological structure with four transmembrane domains (M1–4), two extracellular loops (E1 and E2), a cytoplasmic loop (CL), and with both amino and carboxyl terminus (NT and CT, respectively) in the cytosol [1,3,7]. Most connexins have been shown to be able to form functional GJs to mediate intercellular communications between cells from the same tissue (most commonly in the form of homotypic GJs) as well as between cells from different tissues (commonly via heterotypic GJs if these cells express different set of connexins) [5]. The functional consequence of GJs is to synchronize physiological activities in a variety of tissues and organs [1,3,8,9].

Within the vasculature, GJ channels are found at the cell junctions between endothelial cells, the junctions between vascular smooth

muscle cells, and also at the myoendothelial junctions between these two cells [10–13]. In large arteries, an internal elastic lamina is found to fully separate endothelial cells from vascular smooth muscle cells, but in small arteries and arterioles, the internal elastic lamina shows fenestrations, where endothelial cells often project out to make direct contact with the smooth muscle cells forming myoendothelial gap junctions [10,14,15]. Four connexins, Cx37, Cx40, Cx43, and Cx45, have been identified in the vasculature with Cx37 and Cx40 preferentially expressed in the endothelial cells [16,17] and Cx43 and Cx45 were found in the smooth muscle cells [9,18–20]. Lower level of expression of Cx43 in the endothelial cells and Cx37 in the smooth muscle cells were also reported [16–18,20,21]. Cell type specific expression of different connexins in the small arteries predicted formation of homomeric homotypic, homomeric heterotypic, and heteromeric heterotypic GJs in endothelial cells, smooth muscle cells, and at the myoendothelial junctions. Previous studies on heterotypic docking compatibility of these vascular connexins were almost exclusively on rodent connexins [9,22–26]. Limited information is available on the functional status of heterotypic GJs and their channel properties of human vascular connexins, especially on the heterotypic docking compatibility of human Cx37 with other vascular connexins (Cx40,

Abbreviations: Cx37, connexin37; Cx40, connexin40; Cx43, connexin43; Cx45, connexin45; E1, the first extracellular domain; E2, the second extracellular domain; GJ, gap junction; G_j , gap junctional coupling conductance; I_j , macroscopic junctional current; i_j , unitary junctional current; γ_j , unitary gap junction channel conductance; V_j , transjunctional voltage

* Corresponding author at: Department of Physiology and Pharmacology, University of Western Ontario, London, Ontario N6A 5C1, Canada.

E-mail address: donglin.bai@schulich.uwo.ca (D. Bai).

<https://doi.org/10.1016/j.yjmcc.2018.12.013>

Received 12 October 2018; Received in revised form 3 December 2018; Accepted 26 December 2018

Available online 27 December 2018

0022-2828/ © 2018 Elsevier Ltd. All rights reserved.

Cx43, and Cx45), leaving an important knowledge gap.

Studies on rodent connexins revealed that Cx37, Cx40, Cx43, and Cx45 belong to the same group of docking-compatible connexins and each of them was able to form functional heterotypic GJs with the others in the group [22–24,27–29]. For example, mouse Cx37 was reported to be able to form homomeric heterotypic GJs channels with mouse Cx40, Cx43, or Cx45, to allow successful intercellular transfer of Lucifer yellow in transfected HeLa cells [22]. Correspondingly electrical coupling in transfected N2A cells or oocyte expression system indicated that Cx37 can form heterotypic GJ channels with Cx40 or Cx43 respectively [9,23,24,29,30]. However, studies on human vascular connexins revealed that Cx40 showed virtually no coupling when docked with Cx43 or Cx45, distinct from those observed in rodent connexins [31,32], indicating the requirement for a more systematic study on heterotypic docking of human connexins.

It is hypothesized that human Cx37 is able to form homomeric heterotypic GJs with Cx40, Cx43, or Cx45 to mediate GJ coupling between endothelial cells and at myoendothelial junctions. Our in vitro study showed that cells expressing human Cx37 was able to form functional heterotypic GJs with cells expressing Cx43 or Cx45, but not Cx40. Designed docking variants in Cx40 E1 or E2 domains successfully established heterotypic docking with Cx37. Both Cx37/Cx43 and Cx37/Cx45 GJs showed prominent inward rectifications in the junctional current (I_j) - transjunctional voltage (V_j) relationship for the initial $I_{j,s}$, but an outward rectification at the steady state $I_{j,s}$. The coupling conductance of Cx37/Cx45 could be up/down regulated by small changes in transjunctional voltage (V_j , 5–10 mV). Characterizing the properties of these heterotypic GJs will help to understand how vascular GJ function could be dynamically regulated by V_j .

2. Methods

2.1. Plasmid construction

Human Cx37 was purchased from R&D Systems Inc. (Cat.# RDC0562, Minneapolis, MN, USA) and PCR was used to subclone Cx37 into pIRES2-EGFP vector to have Cx37-IRES-GFP with following primers: forward: 5' G GCA CTC GAG ATG GGT GAC TGG GGC 3' and reverse: 5' G ACC GGA TCC TTA TAC ATA CTG CTT CTT AGA AGC 3'.

Human Cx40-IRES-DsRed and Cx45-IRES-DsRed were generated as previously described [31,32]. Cx40-IRES-DsRed were used as templates to generate untagged individual point mutants (D55N and P193Q) similar to those described earlier [31]. Cx43-IRES-DsRed was generated from cutting of Cx43 from Cx43-IRES-GFP and ligation into a pIRES2-DsRed2 vector between the restriction sites, *EcoRI* and *BglII*.

Tagged human Cx37-GFP was generated by PCR cloning of Cx37 into pEGFP vector at the restriction sites of *XhoI* and *BamHI* with the following primers: Forward: 5' G GCA CTC GAG ATG GGT GAC TGG GGC 3' Reverse: 5' G ACC GGA TCC TAC ATA CTG CTT CTT AGA AGC 3'. To ensure in-frame insertion we did another mutagenesis and the resultant Cx37-GFP contained a short peptide linker, GSPVAT, between Cx37 V333 and the start codon of GFP. All of the RFP-tagged expression vectors, Cx40-RFP, Cx40 D55N-RFP, Cx40 P193Q-RFP, Cx43-RFP, or Cx45-RFP were in pTag-RFP vector as described previously [31,32].

2.2. Cell culture and transient transfections

Gap junction (GJ) deficient mouse neuroblastoma (N2A) cells or human cervical carcinoma (HeLa) cells (American Type Culture Collection, Manassas, VA, USA) were grown in Dulbecco's Modified Eagle's Medium (DMEM) (Life Technologies Corporation, Grand Island, NY, USA) containing 4.5 g/L D-(+)-glucose, 584 mg/L L-glutamine, 110 mg/L sodium pyruvate, 10% fetal bovine serum (FBS), 1% penicillin, and 1% streptomycin, in an incubator with 5% CO₂ at 37 °C [31]. Prior to transfection, N2A or HeLa cells were replated into a 35 mm dish at ~70% confluency. Cells were transfected with 1.0 µg of a cDNA

construct and 2 µL of X-tremeGENE HP DNA transfection reagent (Roche Diagnostics GmbH, Indianapolis, IN, USA) in Opti-MEM + GlutaMAX-I medium for 5 h. At the end of transfection, the medium was changed back to FBS-containing DMEM and incubated overnight.

On next day transfected N2A cells were replated on glass coverslips for an hour prior to transfer to patch clamp recording chamber. N2A cell pairs expressing Cx37-IRES-GFP (or Cx40, Cx43, Cx45, each of them in IRES-DsRed vector) were selected for homotypic GJ functional studies. For heterotypic GJ studies, Cx37-IRES-GFP transfected cells were mixed with cells transfected with Cx40-IRES-DsRed (or its mutant-IRES-DsRed), Cx43-IRES-DsRed, or Cx45-IRES-DsRed and replated on glass coverslips for one hour to allow formation of heterotypic cell pairs with one expressing GFP and the other expressing DsRed.

Localizations of fluorescent protein tagged connexins, Cx37-GFP, Cx40-RFP, Cx40 D55N-RFP, Cx40 P193Q-RFP, Cx43-RFP, or Cx45-RFP, were studied by expressing these constructs individually in gap junction deficient HeLa cells. Cx37-GFP expressing cells were mixed with cells expressing RFP-tagged Cx40 (or one of its mutants), Cx43, or Cx45 and then replated onto glass bottomed dishes for 3–6 h to allow formation of heterotypic GJs. To show co-localization of GFP and RFP at cell-cell interfaces, these fluorescent images were taken individually on Zeiss LSM800 with Airyscan confocal microscope and then superimposed together. Punctate yellow color signals indicated colocalization of two different connexins, i.e. Cx37-GFP and one of the RFP-tagged Cx40 (or its variant), Cx43, or Cx45. DIC images were also taken to show cell morphology.

2.3. Electrophysiological recording

Glass coverslips containing transfected cells were transferred to a recording chamber on an inverted microscope (Leica DM IRB, Ontario, Canada) containing extracellular solution (ECS) at room temperature (22–24 °C). The ECS contained (in mM): 135 NaCl, 2 CsCl, 2 CaCl₂, 1 MgCl₂, 1 BaCl₂, 10 HEPES, 5 KCl, 5 D-(+)-glucose, 2 Sodium pyruvate, pH 7.4 with 1 M NaOH, and osmolarity of 310–320 mOsm. Whole cell voltage clamp was performed on each of the cell pair with Axopatch 200B amplifier (Molecular Devices, Sunnyvale, CA, USA). Patch pipettes were pulled with a PC-10 puller (Narishige International USA Inc., Amityville, NY, USA) and were filled with intracellular solution (ICS) containing (in mM): 130 CsCl, 10 EGTA, 0.5 CaCl₂, 5 Na₂ATP, 10 HEPES, pH 7.2 with 1 M CsOH, and osmolarity of 290–300 mOsm. Each of the cell pair was voltage clamped at 0 mV. In one cell, a series of voltage pulses was applied for 7 s. The other cell of the pair was constantly held at 0 mV to record gap junctional current (I_j). Currents were low-pass filtered (Bessel filter at 1 kHz) and recorded using pClamp9.2 in a computer at a sampling rate of 10 kHz via an AD/DA converter (Digidata 1322A, Molecular Devices, Sunnyvale, CA, USA).

2.4. Transjunctional voltage dependent gating

Transjunctional voltage (V_j) dependent gating (V_j -gating) was studied in homotypic and heterotypic cell pairs. Voltage pulses of ± 5 , ± 20 to ± 100 mV with 20 mV increments were delivered in one of the cell pair to establish $V_{j,s}$ and transjunctional currents ($I_{j,s}$) were recorded in the other cell. In most cases, $I_{j,s}$ peaked at the beginning and then deactivated (especially with high $V_{j,s}$, ± 40 to ± 100 mV) to a steady-state near the end of a 7 s V_j pulse. Gap junctional conductance (G_j) was calculated ($G_j = I_j/V_j$). The steady state G_j was normalized to the peak G_j to obtain a normalized steady-state junctional conductance ($G_{j,ss}$) for each tested V_j . The $G_{j,ss}$ was then plotted with V_j to obtain a $G_{j,ss}$ - V_j plot, which could normally fit well with a two-state Boltzmann equation for each V_j polarity [31]. Boltzmann parameters, V_0 , G_{min} , G_{max} , A , were determined for each GJ where possible. V_0 is the voltage when the conductance is reduced by half [$(G_{max} - G_{min})/2$], G_{min} is the normalized voltage-insensitive residual conductance, while G_{max} represents

the maximum normalized conductance, and A is the slope of the curve which reflects V_j -gating sensitivity [33].

$$G_{j,ss} = \left(\frac{G_{\max} - G_{\min}}{1 + e^{A(V_j - V_0)}} \right) + G_{\min}$$

2.5. Statistical analysis

Data are expressed as mean \pm SEM (standard error of mean). Kruskal Wallis followed by a Dunn's post-hoc test were used to compare multiple groups of non-parametric data as specified. One-way ANOVA was used to compare multiple groups of data with Gaussian distribution. One sample t -test was used to test if the normalized $G_{j,ss}$ was different from a theoretical value of 1 for the long V_j pulse (25 s) experiment. Statistical significance is indicated with the asterisks on the graphs only for biologically meaningful group comparisons (* $P < 0.05$; ** $P < 0.01$; or *** $P < 0.001$).

3. Results

3.1. Human Cx37, Cx40, Cx43, and Cx45 formed functional homotypic gap junction channels

N2A cells were transfected with expression vectors containing one of the human vascular connexins and each with an untagged fluorescent protein (e.g. Cx37-IRES-GFP, Cx40-IRES-DsRed, Cx43-IRES-DsRed, or Cx45-IRES-DsRed). Cell pairs with positive expression of GFP (or DsRed) were voltage clamped using dual whole cell patch clamp technique. The majority of cell pairs expressing Cx37 showed transjunctional currents (I_j s) in response to a V_j pulse (+20 mV, Fig. 1A), indicating successful formation of Cx37 GJs. Coupling percentage for cell pairs expressing Cx37 was calculated for each transfection and the

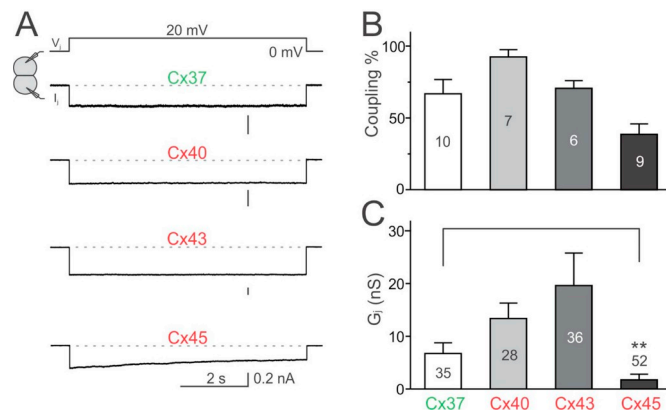


Fig. 1. Coupling percentage and conductance of human homotypic vascular gap junction (GJ) channels.

(A) Dual whole cell patch clamp technique was used to measure transjunctional current (I_j) from N2A cell pairs expressing Cx37, Cx40, Cx43, or Cx45 in response to a +20 mV V_j pulse. Expression of each of these connexins in cell pairs were typically formed functional GJ channels as shown. The green Cx37 and red Cx40, Cx43, or Cx45 text indicate untagged reporters (GFP or DsRed) were expressed with these connexins. (B) Bar graph summarizes the average coupling percentage (coupling%) of cell pairs expressing homotypic Cx37, Cx40, Cx43, or Cx45 from several independent transfections (as shown on each bar). Cx37 cell pairs showed similar coupling% as that of each tested connexin. (C) Bar graph illustrates the average transjunctional conductance (G_j) of all cell pairs expressing the connexins. The G_j was calculated from the initial peak I_j s of cell pairs showing time-dependent changes. A Kruskal-Wallis test followed by Dunn's multiple comparison test showed the G_j of Cx37 was similar to those of Cx40 and Cx43, but significantly greater than Cx45 G_j ($P < 0.05$). The total number of recorded cell pairs is indicated on each bar. (For interpretation of the references to color in this figure legend, the reader is referred to the web version of this article.)

average coupling% of ten transfections was plotted as a bar graph (Fig. 1B). The average coupling conductance (G_j) of Cx37 expressing cell pairs was obtained and plotted (Fig. 1C). Cell pairs expressing Cx40, Cx43, or Cx45 showed similar coupling% and G_j as those of Cx37, except the average of Cx45 G_j was significantly lower than that of Cx37 (Fig. 1C, $P < 0.01$). I_j s of Cx37, Cx40, or Cx43 were typically stable during a 20 mV V_j pulse, except I_j of Cx45, where a time-dependent deactivation was routinely observed (Fig. 1A). The averaged Cx45 G_j is the lowest and that of Cx43 is the highest in the tested GJs.

3.2. Cx37 formed functional heterotypic GJs with Cx43 or Cx45 but not with Cx40

To test if human Cx37 can form functional heterotypic GJs with other vascular connexins, cells expressing Cx37 (with untagged GFP) were mixed with cells expressing Cx40, Cx43, or Cx45 (all with untagged DsRed). Heterotypic cell pairs (one GFP+ and the other DsRed+) were selected to test their coupling status (for calculating coupling%) and coupling conductance (G_j). Most of heterotypic Cx37/Cx43 or Cx37/Cx45 cell pairs formed functional GJs similar to the levels of their respective homotypic GJs (Fig. 2B). Only $19 \pm 10\%$ of heterotypic Cx37/Cx40 cell pairs was able to form functional GJs, which was significantly lower than that of Cx40 GJ (Fig. 2B, $P < 0.01$), but not statistically different from that of Cx37. The G_j of the heterotypic GJs was measured and plotted with their respective homotypic GJs (Fig. 2C). Heterotypic Cx37/Cx43 and Cx37/Cx45 GJs showed a similar level of G_j as those of their respective homotypic GJs. However, Cx37/Cx40 GJs displayed a significantly lower G_j than those of homotypic Cx37 or Cx40 GJs (Fig. 2C, $P < 0.01$ or $P < 0.001$, respectively). Combined lower coupling% and G_j of Cx37/Cx40 GJs indicate that Cx37 is unlikely to form heterotypic GJs with Cx40.

GFP-tagged Cx37 (Cx37-GFP) was used to study if Cx37 could colocalize with Cx40, Cx43, or Cx45 (each was tagged with RFP) at cell-cell interfaces forming GJ plaque-like structures. HeLa cell pairs expressing Cx37-GFP in one and Cx43-RFP or Cx45-RFP in the other showed punctate colocalization at the cell-cell interface (Fig. 2D). However, Cx37-GFP was not colocalized with Cx40-RFP at the cell pairs expressing these constructs (Fig. 2D), indicating that Cx37 unlikely forms GJs with Cx40.

3.3. V_j -gating properties of homotypic vascular GJs

To investigate the transjunctional voltage dependent I_j deactivation (V_j -gating) of cell pairs forming homotypic Cx37, Cx40, or Cx45 GJs, the I_j s were measured in response to a series of V_j pulses (as shown in Fig. 3A). The I_j s of cell pairs expressing each of these connexins showed symmetrical V_j -dependent deactivation with different V_j -gating properties. For Cx37 GJs, when V_j absolute value was ≤ 20 mV, I_j s showed no deactivation. I_j s, in response to V_j s in the range of ± 40 to ± 100 mV, showed strong deactivation. The normalized steady state conductance ($G_{j,ss}$) was plotted as a function of V_j (open grey circles in Fig. 3B), which could be well fitted by a Boltzmann equation for each V_j polarity (smooth dashed grey lines in Fig. 3B). V_j -gating of Cx40 (black filled circles in the middle panel of Fig. 3B) or Cx45 (black filled circles in the bottom panel of Fig. 3B) were also studied using identical V_j protocol. As shown in Fig. 3B, $G_{j,ss}$ - V_j plots could be well fitted with Boltzmann equations for both Cx40 and Cx45 GJs. Comparing with the Boltzmann fitting parameters of Cx37 GJs, the Cx40 GJ showed a larger V_0 , with similar G_{\min} and A , while Cx45 GJs showed lower G_{\min} , and V_0 but similar A (Table 1). The Cx37 GJ Boltzmann fitting curves (smooth dashed grey lines) were plotted onto the $G_{j,ss}$ - V_j plots of Cx40 and Cx45 GJs for easy comparison (Fig. 3B). Under the same experimental conditions, the V_j -gating analysis of Cx43 expressing cell pairs was not possible due to G_j level was too high to maintain proper voltage clamp.

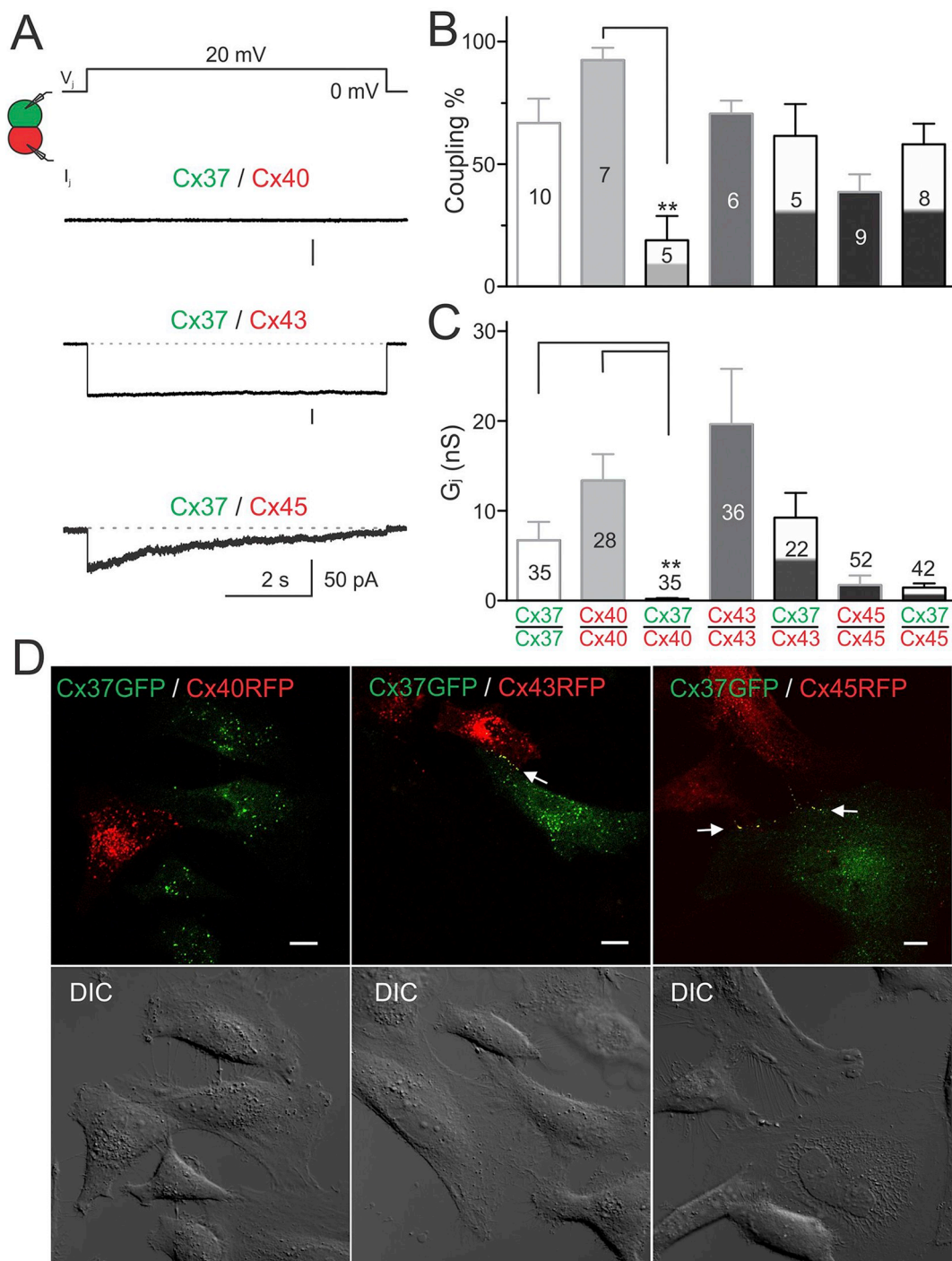


Fig. 2. Coupling percentage and conductance of human heterotypic Cx37/Cx40, Cx37/Cx43, and Cx37/Cx45 gap junctions. (A) A 20 mV V_j -induced I_j s are illustrated from N2A cell pairs expressing Cx37 in one and Cx43, Cx45, or Cx40, in the other. Functional heterotypic Cx37/Cx43, or Cx37/Cx45 GJs could be formed, but most of the Cx37/Cx40 cell pairs failed to show I_j . (B) Bar graph summarizes the coupling% of heterotypic Cx37/Cx40, Cx37/Cx43, or Cx37/Cx45 GJs. A significantly lower coupling% was observed for Cx37/Cx40 cell pairs than that of homotypic Cx40 ($P < 0.01$). The total number of independent transfections is indicated. (C) Bar graph illustrates the coupling conductance (G_j) of heterotypic cell pairs as indicated. Cx37/Cx40 showed a significantly decreased G_j compared to each of the homotypic GJs ($P < 0.01$ vs Cx37 and $P < 0.001$ vs Cx40). The total number of recorded cell pairs is indicated on each bar. Data for homotypic Cx37, Cx40, and Cx43 GJs were identical as those presented in Fig. 1 (with grey outlines) for easy comparison. (D) Confocal fluorescent images (top row) and corresponding DIC images (bottom row) to show localizations of fluorescent protein tagged Cx37, Cx40, Cx43, or Cx45 expressed in HeLa cells. Co-localization of Cx37-GFP and Cx43-RFP (or Cx45-RFP, top middle and right panels) could be observed at the cell-cell interfaces forming GJ plaque-like structures (arrows), but no colocalizations could be observed between Cx37-GFP and Cx40-RFP (top left panel). Scale bar = 10 μ m.

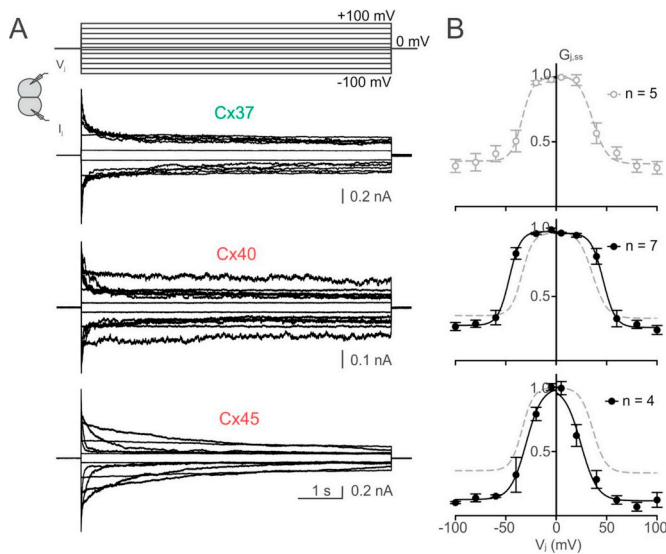


Fig. 3. V_j -gating of homotypic Cx37, Cx40, and Cx45 GJs. (A) Superimposed junctional currents (I_{js}) were recorded from cell pairs expressing homotypic Cx37, Cx40, or Cx45 GJs in response to a series of V_j pulses (± 5 , ± 20 to ± 100 mV with 20 mV increment, as indicated). (B) Normalized steady state junctional conductance, $G_{j,ss}$, (a ratio of steady state G_j to the initial G_j) of Cx37 (open grey circles), Cx40, and Cx45 (middle and bottom panels respectively, black filled circles) were plotted as a function of V_j s. Boltzmann equations were used to fit $G_{j,ss} - V_j$ plots for each of these homotypic GJs. The Boltzmann fitting of Cx37 GJ (dashed grey lines) were superimposed on every plot for comparison. Number of cell pairs for each plot is indicated.

Table 1
Boltzmann Fitting parameters for homotypic and heterotypic gap junctions (GJs).

GJs	V_j polarity ^a	G_{min}	V_0	A
Cx37 (n = 5)	+	0.33 ± 0.03	36.1 ± 2.6	0.14 ± 0.05
	-	0.35 ± 0.03	33.9 ± 3.2	0.18 ± 0.08
Cx40 (n = 7)	+	0.26 ± 0.03	$46.7 \pm 1.9^*$	0.17 ± 0.04
	-	0.28 ± 0.02	$46.6 \pm 1.7^{**}$	0.18 ± 0.04
Cx45 (n = 4)	+	$0.12 \pm 0.03^{***}$	$24.6 \pm 2.2^*$	0.12 ± 0.03
	-	$0.13 \pm 0.03^{***}$	29.9 ± 2.2	0.13 ± 0.02
Cx37/Cx43 (n = 4)	+	0.18 ± 0.13	$55.8 \pm 7.3^*$	0.06 ± 0.03
Cx37/Cx45 (n = 5)	+	$0.06 \pm 0.02^{***}$ (w/Cx37)	$24.5 \pm 1.3^{**}$ (w/Cx37)	0.12 ± 0.01
Cx37/D55N (n = 7)	+	0.31 ± 0.03	36.3 ± 4.3	0.24 ± 0.26
	-	0.27 ± 0.02	$35.4 \pm 2.7^*$ (w/Cx40)	0.21 ± 0.11
Cx37/P193Q (n = 5)	+	$0.19 \pm 0.02^*$ (w/Cx37)	43.6 ± 1.5	0.11 ± 0.02
	-	0.28 ± 0.03	$36.7 \pm 2.0^{**}$ (w/Cx40)	0.16 ± 0.06

Data are presented as mean \pm SEM and V_0 are absolute values. One-way ANOVA followed by Tukey post-hoc test was used to compare Boltzmann fitting parameters of the homotypic and heterotypic GJs against the respective controls (or as indicated) with the same V_j polarity. Student *t*-test was used to compare Boltzmann fitting parameters of Cx37/Cx43 GJ with those of Cx37. The number of asterisks indicate the statistical difference level (* $P < 0.05$, ** $P < 0.01$, *** $P < 0.001$).

^a V_j polarity of heterotypic GJs is defined by the relative voltage level of Cx37-expressing cell.

3.4. V_j -gating properties of heterotypic Cx37/Cx43 and Cx37/Cx45 GJs

The same twelve voltage pulses were delivered to heterotypic Cx37/Cx43 or Cx37/Cx45 cell pairs, typical induced junctional currents (I_{js}) showed strong V_j -gating when Cx37 cell with $+V_j$ s (or when Cx43 or Cx45 with $-V_j$ s), but at the opposite V_j s (i.e. Cx37 with $-V_j$ s or Cx43, or

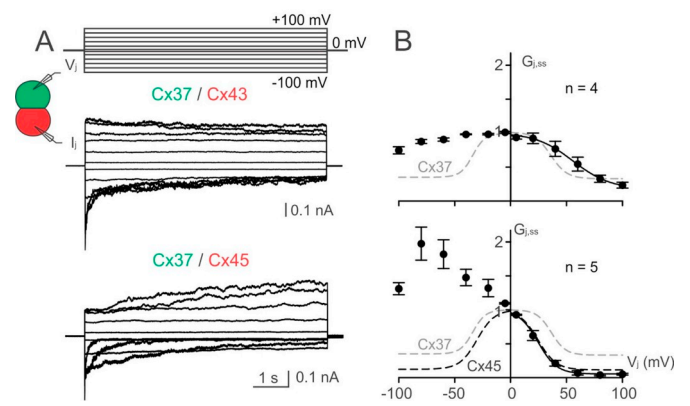


Fig. 4. V_j -gating of heterotypic Cx37/Cx43 and Cx37/Cx45 GJs. (A) Superimposed I_{js} from heterotypic Cx37/Cx43 or Cx37/Cx45 cell pairs in response to a series of V_j pulses as indicated. (B) Normalized steady state junctional conductance, $G_{j,ss}$, of Cx37/Cx43 or Cx37/Cx45 were plotted with tested V_j s. The data of $G_{j,ss} - V_j$ plot when Cx37 cell with $+V_j$ (or when Cx43 or Cx45 with $-V_j$) could be well fitted with a Boltzmann equation for each of Cx37/Cx43 or Cx37/Cx45 GJs. Boltzmann fitting curves of V_j -gating of homotypic Cx37 (smooth grey dashed lines) or Cx45 (smooth black dashed lines) GJ were superimposed on the plots for easy comparison.

Cx45 with $+V_j$ s), little V_j -gating was observed for Cx37/Cx43 GJ or even reverse V_j -gating for Cx37/Cx45 GJ (Fig. 4A). The V_j levels sufficient to induce V_j -gating appeared to be different for these two heterotypic GJs with Cx37/Cx43 GJ in the range of $+40$ to $+100$ mV (on Cx37 or -40 to -100 mV on Cx43) and Cx37/Cx45 GJ in the range of $+20$ to $+100$ mV (on Cx37 or -20 to -100 mV on Cx45). $G_{j,ss} - V_j$ plots were generated for Cx37/Cx43 and Cx37/Cx45 GJs and in both cases the data were fitted well with Boltzmann equations when Cx37 with $+V_j$ (or when Cx43 or Cx45 with $-V_j$) (Fig. 4B), but not the opposite V_j . The Boltzmann fitting parameters are listed in Table 1. The V_0 of Cx37/Cx43 GJ was significantly higher than that of Cx37 GJ and the G_{min} and V_0 of Cx37/Cx45 GJ were significantly lower than those of Cx37 GJ. The Boltzmann fitting parameters of Cx37/Cx45 were similar to those of homotypic Cx45 GJ (Fig. 4B, Table 1).

The I_{js} of these two heterotypic GJs displayed some interesting features. For example, the amplitude of the initial apparent inward (defined by the Cx43 or Cx45 cell) junctional currents, $I_{j,ini}$, induced by a V_j appeared to be larger than the corresponding outward $I_{j,ini}$ for both heterotypic GJs (Fig. 5A, B, open triangles). However, the amplitude of the end of inward junctional currents, $I_{j,end}$, were much lower than the corresponding outward $I_{j,end}$ (Fig. 5A, B, filled triangles). To quantitatively describe this, we calculated the ratio of junctional conductance $G_j(-)/G_j(+)$ for both the $I_{j,ini}$ and $I_{j,end}$ and plotted with the absolute V_j s (Fig. 5C). It is very interesting to observe that the ratio $G_j(-)/G_j(+)$ for Cx37/Cx43 GJs were V_j dependent ($P < 0.01$ for both the initial and the end currents). But the ratio $G_j(-)/G_j(+)$ for Cx37/Cx45 GJs failed to show any V_j dependence for both the initial and the end of the I_{js} ($P > 0.05$ for both cases).

Cx37/Cx43 cell pairs sometimes showed one functional GJ channel to allow us to study single channel currents (i_{js}) at different V_j s (Fig. 6A). All point histograms and Gaussian fits were used to measure the amplitudes of i_{js} for the main conducting state (the main open state) (Fig. 6B). Various levels of subconductance states were also observed (Fig. 6A open arrows) for this cell pair. The plot of i_j (main conducting state) $- V_j$ from 4 cell pairs showed inward rectification (Fig. 6C) similar to that of macroscopic $I_j - V_j$ plot for Cx37/Cx43 GJs (Fig. 5B). The γ_j of the main open state showed some interesting features. First, when Cx43 with $-V_j$ (or Cx37 with $+V_j$) the $\gamma_j(-)$ is larger than the γ_j of opposite V_j polarity, $\gamma_j(+)$. Second, both $\gamma_j(-)$ and $\gamma_j(+)$ were not constant at different V_j levels. The $\gamma_j(-)$ increased with the increase of V_j values, while the $\gamma_j(+)$ decreased with the increase of V_j values. Third, the

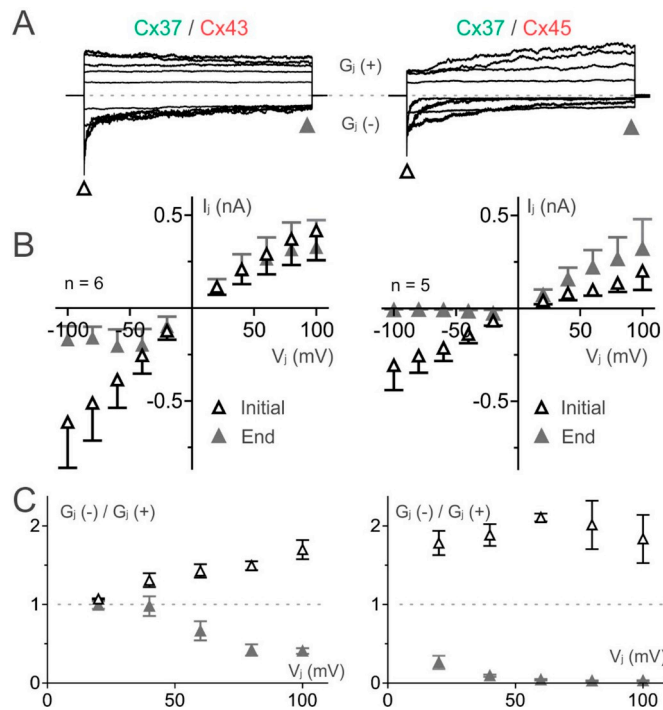


Fig. 5. Heterotypic Cx37/Cx43 and Cx37/Cx45 GJs showed similar and different rectifying properties.

(A) Same I_j s as shown in Fig. 4A are shown here to illustrate measurement at the initial (open triangle) and the end (grey filled triangle) of each I_j and the definition of positive conductance $G_j(+)$ when Cx43 or Cx45 with $+V_j$ s and negative conductance $G_j(-)$ when Cx43 or Cx45 with $-V_j$ s. (B) $I_j - V_j$ plots were constructed for Cx37/Cx43 and Cx37/Cx45 GJs for both the initial (black open triangles) and the end (filled grey triangles) of the I_j s. (C) The ratios of $G_j(-)/G_j(+)$ for the initial (black open triangles) and the end (filled grey triangles) were plotted with V_j s. The ratio was nearly constant for Cx37/Cx45 GJs at different V_j s. It was not the case for Cx37/Cx43 GJ, which showed an increase with V_j for the initial conductance ratio, but a decrease for the end conductance ratio.

ratio of $\gamma_j(-)/\gamma_j(+)$ was increased with V_j values in a linear fashion and showed V_j -dependence ($P < 0.05$, Fig. 6C right panel), again similar to what observed for the macroscopic initial $G_j(-)/G_j(+)$ ratio changes with V_j .

3.5. Characterization of V_j -gating of heterotypic Cx37/Cx43 and Cx37/Cx45 GJs with prolonged V_j pulses

Both heterotypic Cx37/Cx43 and Cx37/Cx45 GJs showed a prominent V_j -gating when positive voltages were administered to the Cx37 cell (or Cx43 or Cx45 cell with $-V_j$) and an apparent reverse V_j -gating on the opposite V_j polarity for Cx37/Cx45 GJ. As the V_j -gating kinetics was slow in low level of V_j s, longer V_j pulses (duration = 25 s) are needed to allow better estimation of steady state of I_j s and longer inter pulse intervals (25 s) are also necessary to allow recovery of deactivated GJs (Fig. 7A). We focused on very low V_j levels from ± 2 to ± 20 mV as it is possible for vascular cells to have transient membrane potential differences especially at the myoendothelial cell junctions [34,35]. As shown in Fig. 7, the normalized steady state conductance ($G_{j,ss}$) of Cx37/Cx43 GJs were consistently around one, except -20 mV where a significant drop was observed (open circles, Fig. 7B). Distinct from the Cx37/Cx43 GJs, the $G_{j,ss}$ of Cx37/Cx45 GJs showed a significant reduction when V_j s were equal or lower than -5 mV (filled black circles, Fig. 7) and a significant increase (reverse V_j -gating) when V_j s were equal or higher than $+10$ mV (filled grey circles, Fig. 7), indicating that G_j of Cx37/Cx45 could be down/up regulated by a V_j of only 5–10 mV.

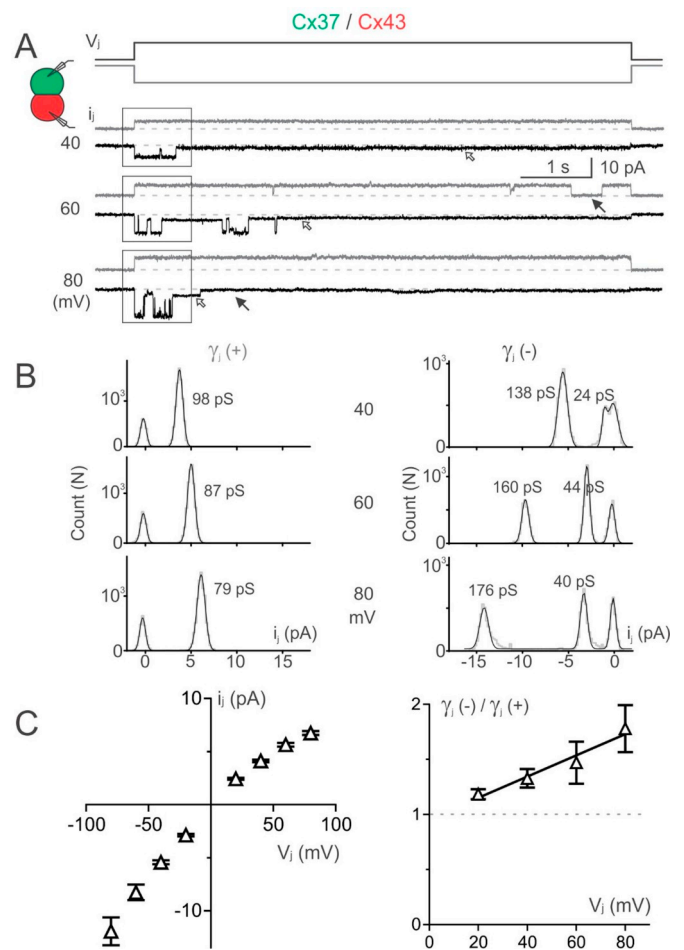


Fig. 6. Unitary channel properties of heterotypic Cx37/Cx43 GJ.

(A) Single channel currents (i_j s) were recorded from a heterotypic Cx37/Cx43 cell pair at the indicated V_j s. Grey and black traces are i_j s in response to $-V_j$ s and $+V_j$ s, respectively. (B) All point histograms were generated at the boxed areas shown in panel A. Gaussian fits were used to determine the i_j amplitudes of main open state and the subconductance state (as indicated on each plot). Note the single channel conductances with inward current, $\gamma_j(-)$, were larger than those of outward current, $\gamma_j(+)$. (C) $i_j - V_j$ relationship of heterotypic Cx37/Cx43 GJ at the main open state was constructed and showed inward rectification. Right panel is the average ratio of $\gamma_j(-)/\gamma_j(+)$ - V_j relationship for Cx37/Cx43 GJ. The ratio was increased with V_j in a linear fashion and was significantly deviated from horizontal (dashed grey line).

3.6. Establish gap junction coupling of Cx37/Cx40 by designed docking variants

To explore the structural mechanisms of why Cx37 hemichannel is unable to dock with Cx40 hemichannels to form functional heterotypic GJs, we aligned key portions of docking domains (part of E1 and E2 domains) of the human vascular connexins with those of Cx26 (Fig. 8A). Similar to previously described [31,32], these connexins aligned very well with Cx26 in these domains, especially on those equivalent docking hydrogen bond (HB) forming residues (Fig. 8A). E1 and E2 of Cx40 showed several unique key residues at the docking interface (for example, D55 on the E1 and P193 on the E2 domain) could restrict its ability to form docking interactions with docked connexin due to an electrostatic repulsion (D55, Supplemental Fig. 1A) or a very different docking interface structure of Cx40 E2 due to existence of P193. Our homology model of Cx40 P193Q showed that this variant can take a similar main chain structure as that of Cx26 and could form hydrogen bonds and hydrophobic interactions at the docking interface in heterotypic Cx37/Cx40 P193Q GJ (Supplemental Fig. 1B).

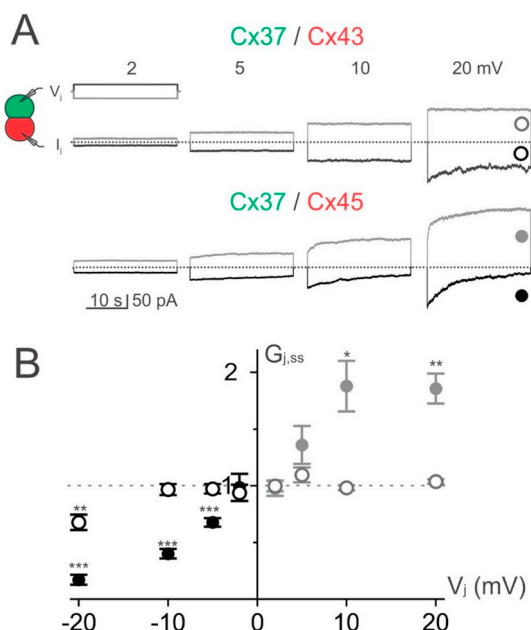


Fig. 7. Long voltage pulse protocol revealed the threshold of heterotypic Cx37/Cx43 and Cx37/Cx45 GJ V_j -gating.

(A) I_j s were recorded in response to a 25 s V_j -protocol at ± 2 , ± 5 , ± 10 , and ± 20 mV (as indicated) for heterotypic Cx37/Cx43 (top row) and Cx37/Cx45 (bottom row) cell pairs. The grey colored I_j s correspond to $+V_j$ on Cx43 or Cx45 cell (or $-V_j$ on Cx37 cell). While black colored I_j s correspond to $-V_j$ on Cx43 or Cx45 cell (or $+V_j$ on Cx37 cell). (B) Normalized steady state conductance, $G_{j,ss}$, of Cx37/Cx43 (open circles) or Cx37/Cx45 (filled circles) GJ were plotted to the respective V_j s (defined by Cx43 or Cx45 cells). The $G_{j,ss}$ of Cx37/Cx43 GJs showed no change at the tested V_j s, except -20 mV where a significant reduction in $G_{j,ss}$ was observed ($P < 0.01$, one-sample t -test). However, the $G_{j,ss}$ of Cx37/Cx45 GJs displayed significant V_j -gating starting at -5 mV ($P < 0.001$) and reverse V_j -gating (an increase in steady-state conductance) starting at $+10$ mV ($*P < 0.05$).

Our homology model predicted that designed Cx40 variants, D55N or P193Q, eliminated the electrostatic repulsion at the E1 or the E2 main chain structure issue near P193, respectively. Our experimental tests on heterotypic Cx37/Cx40 D55N (or Cx37/Cx40 P193Q) cell pairs demonstrated that each of these Cx40 variants successfully formed heterotypic GJs with Cx37. As shown in Fig. 8B,C, majority of heterotypic Cx37/D55N or Cx37/P193Q cell pairs formed functional GJs. The coupling percentages of both Cx37/D55N and Cx37/P193Q were similar to those of homotypic Cx37 or Cx40 but were significantly higher than that of Cx37/Cx40 cell pair (Fig. 8C, $P < 0.05$ for both variants). Similarly, the G_j of heterotypic Cx37/D55N (or Cx37/P193Q) GJs was significantly higher than that of Cx37/Cx40 and was similar to those of homotypic Cx37 or Cx40 GJs (Fig. 8D). Significantly increased coupling % and G_j of Cx37/D55N or Cx37/P193Q than those of Cx37/Cx40 demonstrated that these Cx40 variants were fully capable of docking with Cx37 to form functional heterotypic GJs.

Mixing HeLa cells expressing Cx37-GFP with cells expressing Cx40 D55N-RFP (or P193Q-RFP), we were able to find colocalized GJ plaque-like structures at the cell-cell interface in heterotypic cell pairs for both Cx40 variants (Fig. 8E), different from the heterotypic cell pairs with wildtype Cx40 (Fig. 2D).

The V_j -gating of Cx37/D55N or Cx37/P193Q GJs was largely symmetrical similar to those of homotypic Cx37 and Cx40 GJs (Supplemental Fig. 2A). $G_{j,ss} - V_j$ plots were constructed and the data were fitted well with Boltzmann equations for both V_j polarities (Supplemental Fig. 2B). The Boltzmann fitting parameters (Table 1) were similar to those of Cx37 or Cx40 GJs with only one consistent change for both variants, a lower V_0 values than those of Cx40 GJ when Cx37 cell with $-V_j$ s (or Cx40 variants with $+V_j$ s).

4. Discussion

The present study is the first to investigate functional status and channel properties of human heterotypic Cx37/Cx40, Cx37/Cx43, and Cx37/Cx45 GJs. Our results showed that the coupling status and conductance (G_j) of both heterotypic Cx37/Cx43 and Cx37/Cx45 GJs were comparable to the respective homotypic GJs, indicating that these heterotypic GJs were functional. However, significantly lower coupling % and G_j were observed for heterotypic Cx37/Cx40 cell pairs, indicating that Cx37 was unable to form heterotypic GJs with Cx40. Previously designed Cx40 variants [31], removing electrostatic or structural issues at the extracellular domains rescued the heterotypic docking and both formed functional heterotypic GJs with Cx37. Detailed characterization of Cx37/Cx43 and Cx37/Cx45 GJs revealed that both GJs showed asymmetric V_j -gating and rectifications in current-voltage ($I_j - V_j$) relationship. However, the rectification of Cx37/Cx45 GJs (peak I_j s) appeared to be near 0 mV, while the rectification of Cx37/Cx43 GJs (peak I_j s) was continuous throughout the full range of tested V_j s (-100 to $+100$ mV). Similar continuous rectification was also observed at the Cx37/Cx43 single GJ channel level at the main conductance state. Long duration V_j pulses (25 s and within ± 20 mV) produced a strong V_j -gating (threshold of -5 mV on Cx45 cell) or reverse V_j -gating (threshold of $+10$ mV on Cx45 cell) for Cx37/Cx45 GJs, but only a minor V_j -gating (threshold of -20 mV) and no reverse gating for Cx37/Cx43 GJs. The knowledge of coupling status and detailed channel properties of these vascular heterotypic GJs is very useful for understanding the roles of GJ in modulating vasomotor response.

4.1. Physiological role of vascular connexins

Blood circulation in tissues and organs is highly regulated by well-coordinated dilation or constriction of small arteries and arterioles. These vasomotor responses, especially vasodilation, can propagate back into larger arteries to meet the local demand for blood supply [36,37]. Direct GJ intercellular communications have been shown to play a critical role in the conduction of vasomotor responses from arterioles to larger arteries [35–38]. Both endothelial cells and smooth muscle cells in small arteries or arterioles express two or more connexins and they often found to be colocalized at cell-cell junctions between endothelial cells, smooth muscle cells, and myoendothelial junctions likely forming homomeric or heteromeric as well as homotypic and heterotypic GJs [12,13,17]. Knockout mouse models have been generated for each of the vascular connexins and collectively argue strongly that these connexins play important role in vasculature development and animal survival [39–42]. These in vivo animal models and many pharmacological experiments showed an important role for GJs in vasomotor control [35–37]. Our in vitro characterization of different types of human homotypic and heterotypic GJs will help to delineate the possible interactions among these vascular connexins. Demonstration at in vivo or in situ for the existence of these heterotypic GJs is needed to fully understand their roles in vasomotor control.

4.2. Docking and formation of heterotypic gap junctions among human vascular connexins

Vascular endothelial cells mainly express Cx37 and Cx40, while smooth muscle cells abundantly express Cx43 and Cx45 with some exceptions [12,13]. This expression pattern argues that heterotypic GJs likely play an important role in the myoendothelial junctions. If we only consider simple homomeric heterotypic GJs, they could be Cx37/Cx43 (or Cx45) and Cx40/Cx43 (or Cx45) GJs and it is also theoretically possible to have heterotypic GJs within endothelial (Cx37/Cx40) or smooth muscle cells (Cx43/Cx45). Previous functional studies on rodent connexins indicate that homomeric heterotypic Cx37/Cx43, Cx37/Cx45, and Cx43/Cx45 GJs were functional [22,30,50] and displayed connexin-specific asymmetric V_j -gating [9,23,28,29,51,52]. Our

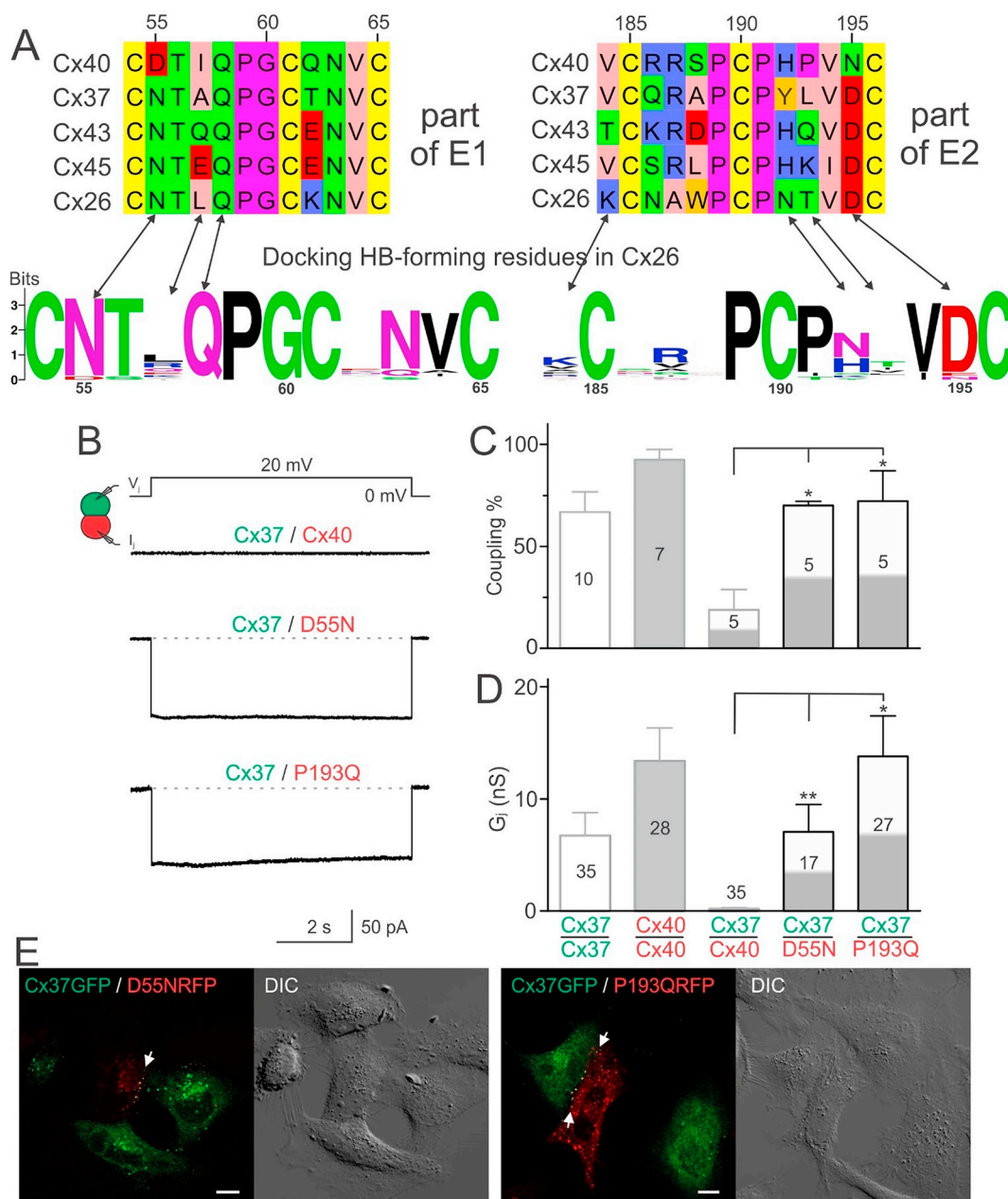


Fig. 8. Sequence alignment, coupling percentage and G_j of heterotypic GJs of Cx37 with Cx40 variants.

(A) Part of the E1 and E2 domains of Cx40, Cx37, Cx43, and Cx45 are aligned with those of Cx26. The docking hydrogen bond (HB)-forming residues in Cx26 structure (2ZW3) and their equivalent residues in Cx26 are indicated with arrows. Sequence logos were generated with WebLogo for all human connexins capable of making functional GJ channels. Out of the seven putative docking residues, Cx40 D55 and P193 are uniquely different from Cx37, Cx43 and Cx45 and many other human connexins and are chosen to generate the variants, D55N and P193Q. The residue numbering follows those of Cx40. (B) Representative I_j were recorded from heterotypic Cx37/Cx40 D55N (Cx37/D55N) or Cx37/P193Q cell pairs in response to +20 mV V_j pulse. I_j of Cx37/Cx40 is shown for comparison, which is the same as that in Fig. 2A. (C) Bar graph summarizes the coupling% of heterotypic Cx37/Cx40, Cx37/D55N, and Cx37/P193Q GJs. Both Cx37/D55N and Cx37/P193Q showed a significant increase in the coupling% compared to that of Cx37/Cx40 ($P < 0.05$). The total number of independent transfections is indicated. (D) Bar graph illustrates the averaged G_j of different cell pairs as indicated. A significant increase in G_j was observed for both Cx37/D55N and Cx37/P193Q cell pairs compared to that of Cx37/Cx40. The total number of recorded cell pairs is indicated. Data for Cx37/Cx37, Cx40/Cx40, and Cx37/Cx40 GJs were identical as those presented in Figs. 1 and 2 (with grey outlines) for easy comparison. (E) Confocal fluorescent images and the corresponding DIC images to show localizations of fluorescent protein tagged Cx37, Cx40 variants D55N or P193Q expressed in HeLa cells. Unlike those observed for Cx37 and Cx40 cell pairs (Fig. 2D), co-localization of Cx37-GFP and Cx40 D55N-RFP or P193Q-RFP could be observed at the cell-cell interfaces forming GJ plaque-like structures (arrows). Scale bar = 10 μ m.

current and previous studies showed that the corresponding human connexins were also able to form functional heterotypic Cx37/Cx43, Cx37/Cx45, and Cx43/Cx45 GJs with similar V_j -gating properties (present study and [32]). However, different from those observed in rodent heterotypic GJs [9,22,24,25,29,51,53,54], we found that human Cx40 was unable to dock and form functional heterotypic GJs with

human Cx37 (present study), Cx43 [31], or Cx45 [32]. Docking incompatible in Cx37/Cx40 GJ was based on significantly lower coupling percentage and coupling conductance of Cx37/Cx40 cell pairs and no co-localization at the cell-cell interfaces with the two different fluorescent protein tagged connexins. Incompatible docking of human Cx40 with any of the other human vascular connexins indicate that GJ

intercellular communications at the myoendothelial junctions likely rely on Cx37/Cx43 or Cx37/Cx45 GJs and the GJs within endothelial cells are probably dependent on homotypic Cx37 or Cx40 GJs.

Sequence alignment of E1 and E2 domains of all human vascular connexins with those of Cx26 (see Fig. 8A) revealed that most of the amino acid residues are highly conserved and most likely take a similar structure as the crystal structure of Cx26 GJ [55]. Based on this hypothesis, we developed homology structure models of heterotypic GJs, including Cx40/Cx43, Cx40/Cx45, and Cx40/Cx37. Our models predict that Cx40 is unique at the docking interface with an aspartate at the 55th position (D55) carrying a negative charge and a proline residue at the 193rd position constraining the local main chain structure. Interestingly, our designed Cx40 variants, D55N or P193Q (exchanging with the corresponding residues in Cx43), eliminated the electrostatic repulsion or the main chain structure issue, respectively. Each variant not only successfully rescued their docking with Cx43 or Cx45 [31,32], but also with Cx37, indicating that the docking interface structure of Cx37 GJ is also very similar to that of Cx26 GJ and likely using similar noncovalent interactions for heterotypic or homotypic docking.

4.3. Similarity and differences between Cx37/Cx43 and Cx37/Cx45 GJs

As discussed above, Cx37/Cx43 and Cx37/Cx45 GJs are the most likely candidates for intercellular communication at the myoendothelial junction in small arteries. Detailed characterization of these GJs found that both GJs showed asymmetric V_j -gating and inward rectifications for their $I_j - V_j$ relationship at the initial peak I_j , but both with outward rectification near the end of the I_j s (see Fig. 5). This means that the coupling conductance (G_j) is high when Cx37 expressing cell is transiently depolarized in the Cx37/Cx43 or Cx37/Cx45 cell pairs (or the Cx43 or Cx45 cell transiently hyperpolarized). However, if the depolarization of Cx37 cell is sustained in these heterotypic cell pairs, then the G_j is quickly diminished to a much lower level for both Cx37/Cx43 and Cx37/Cx45 GJs. On the opposite V_j polarity, i.e. membrane depolarization in Cx43 or Cx45 cells (or hyperpolarization of Cx37 cell), the G_j was either not changed or increased for Cx37/Cx43 or Cx37/Cx45 GJs (Figs. 4, 7). Due to that vascular smooth muscle cells and endothelial cells do not fire any action potentials, it is unlikely to have large V_j s between these two types of cells. Thus, we investigated the G_j changes with small likely physiological relevant changes in the V_j (± 2 to ± 20 mV) for each of Cx37/Cx43 or Cx37/Cx45 cell pair and observed similar V_j -dependent G_j modulation. As a slower V_j -gating kinetics was observed at these low V_j s, we used a much longer V_j pulse (25 s) to have a better estimate for steady state properties for these heterotypic GJs (Fig. 7).

Several V_j -gating properties for Cx37/Cx45 GJs were distinct from those of Cx37/Cx43 GJs. First, much lower threshold of V_j (-5 mV on Cx45 cell) showed V_j -gating in Cx37/Cx45 GJs than that of Cx37/Cx43 (-20 mV on Cx43 cell). While at the opposite V_j polarity, a $+10$ mV or larger V_j (on Cx45 cell) produced reverse V_j -gating (or increased I_j with time during the V_j pulse) in Cx37/Cx45 GJ, but no reverse V_j -gating was observed for Cx37/Cx43 GJs at any tested V_j s. Second, half deactivation voltage (or V_0 of Boltzmann fit) of Cx37/Cx45 GJs was estimated to be 24.5 ± 1.3 mV, which was much lower than that of Cx37/Cx43 GJs ($V_0 = 55.8 \pm 7.3$ mV). Third, the V_j -gating sensitivity (slope in the Boltzmann fitting curves) of Cx37/Cx45 GJs ($A = 0.12 \pm 0.01$) was higher than that of Cx37/Cx43 ($A = 0.06 \pm 0.03$). Fourth, the estimated residue conductance level (or the Boltzmann fitting parameter G_{\min}) of Cx37/Cx45 GJs (0.06 ± 0.02) was much lower than that of Cx37/Cx43 ($G_{\min} = 0.18 \pm 0.13$). Finally, the $G_j(-)/G_j(+)$ plot of Cx37/Cx45 GJs showed little V_j -dependence for both initial and end (steady-state) conductance, while the same plot of Cx37/Cx43 GJs displayed V_j -dependent changes for both initial and end conductance (Fig. 5C). These unique properties of Cx37/Cx45 GJs offered some very interesting ways to dynamically regulate the electrical coupling of the myoendothelial junction.

4.4. Mechanisms of V_j -gating in heterotypic gap junctions

Homotypic GJ channels are normally gated by V_j in a mirror symmetrical way with connexin-specific gating properties (e.g. Fig. 3). The underline mechanism of V_j -gating is believed to be gating one of the two docked connexin hemichannels either at $-V_j$ side (when a connexin with negative gating polarity) or $+V_j$ side (when a connexin with positive gating polarity) [56]. Studying heterotypic GJ channel greatly facilitated the assignment of gating polarity of many connexins as the component hemichannel often retain its V_j -gating characteristics. For example, Cx45 was consistently assigned to have a negative gating polarity, retained its V_j -gating signatures in our studied heterotypic Cx37/Cx45 GJs (Fig. 4). As Cx45 GJ displayed one of the smallest single channel conductance, when its hemichannel is docked with another higher conductance (low resistance) hemichannel like Cx37, large portion of the V_j is predicted to drop on the Cx45 hemichannel and showed a V_j -gating profile (when Cx45 side with $-V_j$ s) very much similar to that of homotypic Cx45 GJs. It is very interesting that when Cx45 side with $+V_j$ s in Cx37/Cx45 GJs, the I_j s were not deactivated, but were significantly increased with time (reverse V_j -gating). One possible explanation of the I_j increase was due to an incomplete recovery of previously deactivated GJs (Fig. 4). However, with a much longer inter pulse interval (25 s) we still observed an increase in I_j s in Cx37/Cx45 GJ (when $+V_j$ on Cx45 cell, see data in Fig. 7). Therefore, we believe that this reverse V_j -gating of Cx37/Cx45 GJ is an intrinsic property of this heterotypic GJ, most likely due to properties of Cx45 hemichannel. Supporting such idea, several previous studies on heterotypic GJs containing Cx45 also observed reverse V_j -gating when Cx45 side with $+V_j$ s [29,32,51,52]. In contrast to that of Cx37/Cx45 GJs, the Cx37/Cx43 GJs showed V_j -gating when Cx37 with $+V_j$ s and no reverse V_j -gating on the opposite V_j s. The V_j -gating profile is also somewhat different from those of Cx37 GJs (with a larger A and V_0 of Boltzmann fitting parameters). It is very interesting for Cx37/Cx43 GJs showing a continuous inward rectification throughout the tested V_j s for both macroscopic I_j s and microscopic i_j s (main conductance state), which was reflected by both the $I_j - V_j$ (or $i_j - V_j$) plot and $G_j(-)/G_j(+)$ $- V_j$ (or $\gamma_j(-)/\gamma_j(+)$ $- V_j$) plot, indicating that the V_j -dependent rectification was at least in part due to the rectification at individual channels. The molecular mechanisms of GJ channel rectification is not clear. But it may be related to pore lining residues changing their orientations under different V_j s to facilitate or hinder ion permeation.

5. Conclusion

We provided experimental evidence that Cx37 hemichannel can dock with Cx43 or Cx45 hemichannels to form functional heterotypic GJs but not with Cx40 hemichannels. Cx40 variants, D55N or P193Q, rescued heterotypic docking with Cx37. Heterotypic Cx37/Cx43 and Cx37/Cx45 GJs exhibited distinct rectifying properties and the G_j of Cx37/Cx45 can be reduced or elevated by small difference in membrane potentials (5–10 mV). V_j -dependent rectifying properties of Cx37/Cx43 GJs were retained at individual channel level.

Funding

This work was supported by the Canadian Institutes of Health Research (153415 to D.B.) and Grants-in-Aid for Scientific Research from the Ministry of Education, Culture, Sports, Science and Technology of Japan (26440029 to H.A.). A.S-M. received a travel grant from FAPEMIG of Brazil.

Acknowledgments

We thank Professor Tomitake Tsukihara for his generous help on developing homology models.

Conflict of interest

None declared.

Author contributions

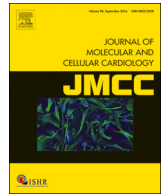
N.K.K. designed and performed majority of the patch clamp experiments, analyzed data, generated most of the final figures, and wrote an early draft of the manuscript. A.S.M. designed and performed some patch clamp experiments. H.C. generated all the expression constructs and designed and performed colocalization study. H.A. developed homology models. D.B. designed the project, supervised data analysis and critically revised the manuscript.

Appendix A. Supplementary data

Supplementary data to this article can be found online at <https://doi.org/10.1016/j.yjmcc.2018.12.013>.

References

- [1] D.A. Goodenough, D.L. Paul, Gap junctions, *Cold Spring Harb. Perspect. Biol.* 1 (1) (2009) a002576.
- [2] G.S. Goldberg, P.D. Lampe, B.J. Nicholson, Selective transfer of endogenous metabolites through gap junctions composed of different connexins, *Nat. Cell Biol.* 1 (7) (1999) 457–459.
- [3] N.M. Kumar, N.B. Gilula, The gap junction communication channel, *Cell* 84 (3) (1996) 381–388.
- [4] J.C. Saez, V.M. Berthoud, M.C. Branes, A.D. Martinez, E.C. Beyer, Plasma membrane channels formed by connexins: their regulation and functions, *Physiol. Rev.* 83 (4) (2003) 1359–1400.
- [5] D. Bai, A.H. Wang, Extracellular domains play different roles in gap junction formation and docking compatibility, *Biochem. J.* 458 (1) (2014) 1–10.
- [6] G. Sohl, Gap junctions and the connexin protein family, *Cardiovasc. Res.* 62 (2) (2004) 228–232.
- [7] L.C. Milks, N.M. Kumar, R. Houghten, N. Unwin, N.B. Gilula, Topology of the 32-kD liver gap junction protein determined by site-directed antibody localizations, *EMBO J.* 7 (10) (1988) 2967–2975.
- [8] M.V. Bennett, V.K. Verselis, Biophysics of gap junctions, *Semin. Cell Biol.* 3 (1) (1992) 29–47.
- [9] R. Bruzzone, J.A. Haefliger, R.L. Gimlich, D.L. Paul, Connexin40, a component of gap junctions in vascular endothelium, is restricted in its ability to interact with other connexins, *Mol. Biol. Cell* 4 (1) (1993) 7–20.
- [10] C. de Wit, M. Boettcher, V.J. Schmidt, Signaling across myoendothelial gap junctions—fact or fiction? *Cell Commun. Adhes.* 15 (3) (2009) 231–245.
- [11] D.G. Welsh, C.H.T. Tran, B.O. Hald, M. Sancho, The conducted vasomotor response: function, biophysical basis, and pharmacological control, *Annu. Rev. Pharmacol. Toxicol.* 58 (2018) 391–410.
- [12] H.I. Yeh, S. Rothery, E. Dupont, S.R. Coppen, N.J. Severs, Individual gap junction plaques contain multiple connexins in arterial endothelium, *Circ. Res.* 83 (12) (1998) 1248–1263.
- [13] C.E. Hill, N. Rummery, H. Hickey, S.L. Sandow, Heterogeneity in the distribution of vascular gap junctions and connexins: implications for function, *Clin. Exp. Pharmacol. Physiol.* 29 (7) (2002) 620–625.
- [14] G.J. Campbell, M.R. Roach, Fenestrations in the internal elastic lamina at bifurcations of human cerebral arteries, *Stroke* 12 (4) (1981) 489–496.
- [15] S.L. Sandow, C.E. Hill, Incidence of myoendothelial gap junctions in the proximal and distal mesenteric arteries of the rat is suggestive of a role in endothelium-derived hyperpolarizing factor-mediated responses, *Circ. Res.* 86 (3) (2000) 341–346.
- [16] J.E. Gabriels, D.L. Paul, Connexin43 is highly localized to sites of disturbed flow in rat aortic endothelium but connexin37 and connexin40 are more uniformly distributed, *Circ. Res.* 83 (6) (1998) 636–643.
- [17] M.J. van Kempen, H.J. Jongma, Distribution of connexin37, connexin40 and connexin43 in the aorta and coronary artery of several mammals, *Histochem. Cell Biol.* 112 (6) (1999) 479–486.
- [18] T.L. Little, E.C. Beyer, B.R. Duling, Connexin 43 and connexin 40 gap junctional proteins are present in arteriolar smooth muscle and endothelium in vivo, *Am. J. Phys.* 268 (2) (1995) H729–H739 Pt 2.
- [19] K. Pogoda, M. Füller, U. Pohl, P. Kameritsch, NO, via its target Cx37, modulates calcium signal propagation selectively at myoendothelial gap junctions, *Cell Commun. Signal.* 12 (1) (2014) 33.
- [20] N.J. Severs, S. Rothery, E. Dupont, S.R. Coppen, H.I. Yeh, Y.S. Ko, T. Matsushita, R. Kaba, D. Halliday, Immunocytochemical analysis of connexin expression in the healthy and diseased cardiovascular system, *Microsc. Res. Tech.* 52 (3) (2001) 301–322.
- [21] N.M. Rummery, H. Hickey, G. McGurk, C.E. Hill, Connexin37 is the major connexin expressed in the media of caudal artery, *Arterioscler. Thromb. Vac. Biol.* 22 (9) (2002) 1427–1432.
- [22] C. Elfgang, R. Eckert, H. Lichtenberg-Frate, A. Butterweck, O. Traub, R.A. Klein, D.F. Hulser, K. Willecke, Specific permeability and selective formation of gap junction channels in connexin-transfected HeLa cells, *J. Cell Biol.* 129 (3) (1995) 805–817.
- [23] P.R. Brink, K. Cronin, K. Banach, E. Peterson, E.M. Westphale, K.H. Seul, S.V. Ramanan, E.C. Beyer, Evidence for heteromeric gap junction channels formed from rat connexin43 and human connexin37, *Am. J. Physiol. Cell Ph.* 273 (4) (1997) C1386–C1396.
- [24] H. Hennemann, T. Suchyna, H. Lichtenberg-Frate, S. Jungbluth, E. Dahl, J. Schwarz, B.J. Nicholson, K. Willecke, Molecular cloning and functional expression of mouse connexin40, a second gap junction gene preferentially expressed in lung, *J. Cell Biol.* 117 (6) (1992) 1299–1310.
- [25] T.W. White, D.L. Paul, D.A. Goodenough, R. Bruzzone, Functional analysis of selective interactions among rodent connexins, *Mol. Biol. Cell* 6 (4) (1995) 459–470.
- [26] V. Valiunas, R. Weingart, Electrical properties of gap junction hemichannels identified in transfected HeLa cells, *Pflügers Arch.* 440 (3) (2000) 366–379.
- [27] D. Bai, Structural analysis of key gap junction domains—lessons from genome data and disease-linked mutants, *Semin. Cell Dev. Biol.* 50 (2016) 74–82.
- [28] S. Elenes, A.D. Martinez, M. Delmar, E.C. Beyer, A.P. Moreno, Heterotypic docking of Cx43 and Cx45 connexons blocks fast voltage gating of Cx43, *Biophys. J.* 81 (3) (2001) 1406–1418.
- [29] M. Rackauskas, M.M. Kreuzberg, M. Pranevicius, K. Willecke, V.K. Verselis, F.F. Bukauskas, Gating properties of heterotypic gap junction channels formed of connexins 40, 43, and 45, *Biophys. J.* 92 (6) (2007) 1952–1965.
- [30] T.W. White, R. Bruzzone, Multiple connexin proteins in single intercellular channels: connexin compatibility and functional consequences, *J. Bioenerg. Biomembr.* 28 (4) (1996) 339–350.
- [31] A. Jassin, H. Aoyama, W.G. Ye, H. Chen, D. Bai, Engineered Cx40 variants increased docking and function of heterotypic Cx40/Cx43 gap junction channels, *J. Mol. Cell. Cardiol.* 90 (2016) 11–20.
- [32] W.G. Ye, B. Yue, H. Aoyama, N.K. Kim, J.A. Cameron, H. Chen, D. Bai, Junctional delay, frequency, and direction-dependent uncoupling of human heterotypic Cx45/Cx43 gap junction channels, *J. Mol. Cell. Cardiol.* 111 (2017) 17–26.
- [33] D.C. Spray, A.L. Harris, M.V. Bennett, Equilibrium properties of a voltage-dependent junctional conductance, *J. Gen. Physiol.* 77 (1) (1981) 77–93.
- [34] D.G. Welsh, S.S. Segal, Endothelial and smooth muscle cell conduction in arterioles controlling blood flow, *Am. J. Phys.* 274 (1) (1998) H178–H186 Pt 2.
- [35] G.G. Emerson, S.S. Segal, Electrical coupling between endothelial cells and smooth muscle cells in hamster feed arteries: role in vasomotor control, *Circ. Res.* 87 (6) (2000) 474–479.
- [36] S.S. Segal, B.R. Duling, Conduction of vasomotor responses in arterioles: a role for cell-to-cell coupling? *Am. J. Phys.* 256 (3 Pt 2) (1989) H838–H845.
- [37] C. de Wit, T.M. Griffith, Connexins and gap junctions in the EDHF phenomenon and conducted vasomotor responses, *Pflügers Arch.* 459 (6) (2010) 897–914.
- [38] R.E. Haddock, C.E. Hill, Rhythmicity in arterial smooth muscle, *J. Physiol.* 566 (2005) 645–656 Pt 3.
- [39] O. Kruger, A. Plum, J.S. Kim, E. Winterhager, S. Maxeiner, G. Hallas, S. Kirchhoff, O. Traub, W.H. Lamers, K. Willecke, Defective vascular development in connexin 45-deficient mice, *Development* 127 (19) (2000) 4179–4193.
- [40] M. Kumai, K. Nishii, K. Nakamura, N. Takeda, M. Suzuki, Y. Shibata, Loss of connexin45 causes a cushion defect in early cardiogenesis, *Development* 127 (16) (2000) 3501–3512.
- [41] A.G. Reaume, P.A. de Sousa, S. Kulkarni, B.L. Langille, D. Zhu, T.C. Davies, S.C. Juneja, G.M. Kidder, J. Rossant, Cardiac malformation in neonatal mice lacking connexin43, *Science* 267 (5205) (1995) 1831–1834.
- [42] A.M. Simon, A.R. McWhorter, Vascular abnormalities in mice lacking the endothelial gap junction proteins connexin37 and connexin40, *Dev. Biol.* 251 (2) (2002) 206–220.
- [43] P.A. Weber, H.C. Chang, K.E. Spaeth, J.M. Nitsche, B.J. Nicholson, The permeability of gap junction channels to probes of different size is dependent on connexin composition and permeant-pore affinities, *Biophys. J.* 87 (2) (2004) 958–973.
- [44] V. Valiunas, R. Weingart, P.R. Brink, Formation of heterotypic gap junction channels by connexins 40 and 43, *Circ. Res.* 86 (2) (2000) E42–E49.
- [45] F.F. Bukauskas, A.B. Angele, V.K. Verselis, M.V. Bennett, Coupling asymmetry of heterotypic connexin 45/connexin 43-EGFP gap junctions: properties of fast and slow gating mechanisms, *Proc. Natl. Acad. Sci. U. S. A.* 99 (10) (2002) 7113–7118.
- [46] G.T. Cottrell, J.M. Burt, Heterotypic gap junction channel formation between heteromeric and homomeric Cx40 and Cx43 connexons, *Am. J. Phys. Cell Physiol.* 281 (5) (2001) C1559–C1567.
- [47] X. Lin, Q. Xu, R.D. Veenstra, Functional formation of heterotypic gap junction channels by connexins-40 and -43, *Channels (Austin)* 8 (5) (2014) 433–443.
- [48] S. Maeda, S. Nakagawa, M. Suga, E. Yamashita, A. Oshima, Y. Fujiyoshi, T. Tsukihara, Structure of the connexin 26 gap junction channel at 3.5 Å resolution, *Nature* 458 (7238) (2009) 597–602.
- [49] V.K. Verselis, C.S. Ginter, T.A. Bargiello, Opposite voltage gating polarities of two closely related connexins, *Nature* 368 (6469) (1994) 348–351.



Effects of temperature on transjunctional voltage-dependent gating kinetics in Cx45 and Cx40 gap junction channels

Artur Santos-Miranda, Mahmoud Noureldin, Donglin Bai*

Department of Physiology and Pharmacology, University of Western Ontario, London, Ontario, Canada

ARTICLE INFO

Keywords:

Gap junction channel
Connexin40
Connexin45
Gating kinetics, patch clamp

ABSTRACT

Gap junctions (GJs) are intercellular channels directly linking neighbouring cells and are dodecamers of connexins. In the human heart, connexin40 (Cx40), Cx43, and Cx45 are expressed in different regions of the heart forming GJs ensuring rapid propagation of action potentials in the myocardium. Two of these connexins, Cx40 and Cx45, formed functional GJs with prominent transjunctional voltage-dependent gating (V_j -gating), which can be a mechanism to down regulate coupling conductance (G_j). It is not clear the effects of temperature on V_j -gating properties. We expressed Cx40 or Cx45 in N2A cells to study the V_j -gating extent, the kinetics of deactivation, and the recovery time course from deactivation at 22 °C, 28 °C, and 32 °C. Dynamic uncoupling between cell pairs were evaluated at different temperatures, junctional delays, and/or repeating frequencies. Cx40 or Cx45 GJs showed little changes in the extent of V_j -gating, but in both cases with a faster deactivation kinetics at high temperatures. The recovery from deactivation was faster at higher temperatures for Cx45 GJs, but not for Cx40 GJs. Cx45 GJs, but not Cx40 GJs, were dynamically uncoupled when sufficient junctional delays and/or repeating frequency in all tested temperatures. Gap junction specific dynamic uncoupling could play an important role in regulating action potential propagation speed in Cx45 enriched nodal cells in the heart.

1. Introduction

Gap junctions (GJs) are intercellular channels composed of two properly docked connexons (also known as hemichannels), allowing direct exchange of ions and small molecules to synchronize cells/tissues electrically and metabolically. Each connexon (hemichannel) is a hexamer of transmembrane proteins named connexins. In the human genome there are 21 genes encoding different connexins [1,2]. All connexins show similar topological structures with four transmembrane domains linked by two extracellular loops and one cytoplasmic loop with cytosolic amino terminus and carboxyl terminus. Different tissue cells commonly express different connexins. In the human heart, three connexins, Cx40, Cx43, and Cx45, are abundantly expressed in different regions of the myocardium [3–5]. Cx45 is the main connexin in the sinoatrial (SA) and atrioventricular (AV) nodal cells and is also expressed at a lower level in the atria and ventricles [3,6]. Both Cx40 and Cx43 are expressed in the atrial myocytes and Cx43 is the main connexin type in the ventricles [4]. In the ventricular conduction system all three connexins are expressed [3,4,7]. This regional specific expression pattern of connexins in the heart predicts a variety of cardiac gap

junctions being formed. These gap junctions are critical for rapid propagation of action potentials in different regions of the heart leading to a highly synchronized rhythmic beating.

It is well known that cardiac action potentials conduct at different velocity in different regions of the heart with the slowest propagation speed observed at the nodal regions [8,9], including AV node to cause an AV delay, which is important for effective sequential contractions of the atria and ventricles [8,10]. Many factors including sodium channels, calcium channels, potassium channels, cell geometry, passage length, and abundance and function of gap junction channels could contribute to the regional differences in conduction velocity [8,10]. Focusing on gap junctions, the GJ function can be quantitatively measured by coupling conductance (G_j). The G_j level could depend on the abundance and GJ type expressed in the cardiomyocytes. In addition, GJs in the heart could be dynamically modulated by a variety of physiological/pathological factors, including changes in intracellular ion concentrations (including protons/pH and divalent cations), chemicals, and transjunctional voltage (V_j). Transjunctional voltage-dependent gating (also known as V_j -gating) is a ubiquitous property for all GJs. Among the three cardiac connexins, Cx45 and Cx40 GJs have been

Abbreviations: Cx40, connexin40; Cx45, connexin45; GJ, gap junction; G_j , gap junctional coupling conductance; I_j , macroscopic transjunctional current; V_j , transjunctional voltage

* Corresponding author at: Department of Physiology and Pharmacology, University of Western Ontario, London, Ontario N6A 5C1, Canada.

E-mail address: donglin.bai@schulich.uwo.ca (D. Bai).

<https://doi.org/10.1016/j.yjmcc.2018.12.014>

Received 21 September 2018; Received in revised form 29 November 2018; Accepted 26 December 2018

Available online 27 December 2018

0022-2828/ © 2018 Elsevier Ltd. All rights reserved.

shown to have prominent V_j -gating with rapid deactivation kinetics [11–17]. V_j -gating of Cx45 (or Cx40) GJs could reduce G_j to a much lower level (over 80% of original G_j) during large sustained V_j s [13,15–18]. Previous functional characterizations of V_j -gating of GJs were carried out at room temperatures (20–25 °C). The effects of higher temperature near human body temperature on the V_j -gating of these connexins have not been studied, leaving an important knowledge gap. Previous studies demonstrated that the G_j could be dynamically regulated when sufficient junctional delay and repeating frequency (heart rate) provided [19] or during a simulated cardiac action potential protocol at the junction [20–22]. Here we investigated the extent of V_j -gating, the deactivation kinetics, and the recovery kinetics from deactivation of Cx45 and Cx40 GJs. Our results showed that temperature-dependent modulations were GJ (or connexin)-specific. The GJs most vulnerable to dynamic uncoupling was Cx45 GJs with retained dynamic uncoupling during the elevated temperatures tested. This unique dynamic uncoupling of Cx45 GJs might play a role in the delay of action potential propagation in the nodal cells of the heart.

2. Methods

2.1. Plasmid construction

Human Cx45-IRES-GFP and Cx40-IRES-GFP constructs were created as described [19,23]. The human Cx40 and Cx45 cDNA sequence were compared with human reference genome to confirm the accuracy of the sequence with no additional variations being introduced.

2.2. Cell culture and transfection

Connexin deficient mouse neuroblastoma cells (N2A, obtained from American Type Culture Collection, Manassas, VA, USA) were grown in Dulbecco's modified Eagle's medium (DMEM, Invitrogen, Burlington, ON, Canada) containing 10% fetal bovine serum and 1% penicillin and streptomycin, in an incubator maintained at 37 °C and 5% CO₂ atmosphere [24,25]. During transfection, N2A cells were kept for 5 h in Opti-MEM1 + GlutaMAX-I medium supplemented with HEPES and 2.4 g/L NaHCO₃ added with 2 µL of X-tremeGENE HP DNA transfection reagent (Roche, Mississauga, ON) and 1.0 µg of Cx45 or Cx40 cDNA construct. After transfection, the medium was switched back to serum containing DMEM and cells were cultured overnight. Transfected N2A cells were then replated on glass coverslips for 40 min for Cx40 or 75–90 min for Cx45 prior to patch clamp recording. Shorter replating time for Cx40 was used to increase the yield of getting more cell pairs with G_j in the range of 3–9 nS with good gating kinetics.

2.3. Dual patch clamp recording

A glass coverslip with transfected cells was transferred into a recording chamber filled with extracellular solution (ECS) on the stage of an upright microscope (BX51, Olympus). A heated chamber (QE-1 coupled with a temperature control unit TC-344B, Warner Instrument, Hamden, CT, USA) was used to control the ECS temperature at 22 °C, 28 °C or 32 °C. The composition of ECS is (in mM): 140 NaCl, 2 CsCl, 2 CaCl₂, 1 MgCl₂, 5 HEPES, 4 KCl, 5 D-(+)-glucose, 2 Pyruvate, pH 7.4. Cell pairs displaying GFP fluorescence were selected for dual patch clamp recording. Each patch pipette was filled with intracellular solution (ICS) containing (in mM): 130 CsCl, 10 EGTA, 0.5 CaCl₂, 3 MgATP, 2 Na₂ATP, 10 HEPES, pH 7.2. Patch pipettes resistance was typically in the range of 2–3 MΩ. After establishing a whole cell configuration in each of the cell pair, both cells were voltage clamped at 0 mV for a few minutes to allow ICS dialysis into cells. A short (10 ms) transjunctional voltage pulse ($V_j = 10$ mV) was applied to one cell of the pair and the transjunctional current (I_j) was measured in the other cell of the pair. The electrical coupling conductance (G_j) between the cell pair was calculated according to: $G_j = I_j/V_j$. Transjunctional voltage-dependent

gating (V_j -gating) was studied by delivering a series of voltage pulses (7 s in duration) from ± 20 mV to ± 100 mV, with 20 mV increments in one cell of the pair and recording I_j s in another cell of the pair. Sometimes, we also included V_j pulses of ± 5 mV (for Cx45 GJs). Dual patch clamp was achieved via Axopatch 700A amplifier (Molecular Devices, Sunnyvale, CA) with a low-pass filter (cut-off frequency 1 kHz) and digitalized at a 10 kHz sampling rate using an AD/DA converter (Digidata 1322A, Molecular Devices, Sunnyvale, CA). The steady-state conductance was normalized to the respective peak conductance to obtain normalized steady-state conductance ($G_{j,ss}$), which was plotted as a function of tested V_j s. The $G_{j,ss} - V_j$ plot was fitted by a Boltzmann equation for each V_j polarity [26]:

$$G_{j,ss} = (G_{\max} - G_{\min}) / (1 + \exp.[A(V_j - V_0)]) + G_{\min}$$

V_0 is the voltage at which the conductance is reduced by half [$(G_{\max} - G_{\min})/2$]. G_{\max} and G_{\min} are the maximum and minimum normalized conductance, respectively. A is the slope of the fitted curve, which reflects the V_j sensitivity of the GJ channels.

2.4. Statistical analysis

GraphPad Prism (Graph Pad Software, USA) was used to generate bar graphs, plots, and statistical analysis. Data are expressed as mean ± standard error of the mean (SEM). For data groups fit Gaussian distribution, we used one way ANOVA followed by Newman-Keuls post hoc test for comparison. For non-parametric data, we used Kruskal-Wallis test followed by Dunn's post-hoc test to compare groups of data. Statistical significance is indicated with asterisks (* $P < 0.05$, ** $P < 0.01$, *** $P < 0.001$).

3. Results

3.1. Coupling percentage and conductance in cell pairs expressing Cx45 or Cx40 were similar at tested temperatures

N2A cell pairs expressing Cx45 or Cx40 with an untagged reporter (GFP) were selected for dual whole-cell patch clamp analysis. Cell pairs expressing Cx45 showed an averaged GJ coupling percentage of 60–70% at the tested temperatures (Fig. 1A). Moreover, cell pairs expressing Cx40 displayed similar level of GJ coupling percentages at the tested temperatures (Fig. 1A). Gap junction coupling conductance was measured using a V_j pulse delivered in one of the cell pair and transjunctional current (I_j) was recorded in the other (Fig. 1B). Summarized GJ coupling conductance (G_j) for coupled cell pairs was plotted and no statistical difference was observed for cells pairs expressing Cx45 or Cx40 at the three tested temperatures (Fig. 1C). Arrhenius plots of Cx45 (or Cx40) GJ showed no statistically significant G_j changes at the tested temperatures (Supplemental Fig. 1).

3.2. V_j -gating extent of Cx45 or Cx40 GJs at different temperatures

A series of transjunctional voltage (V_j) pulses was applied to one of Cx45-expressing cell pair and transjunctional currents (I_j s) were recorded in the other cell. As shown in Fig. 2A, cell pairs expressing Cx45 at room temperature (22 °C) showed prominent I_j deactivation when the absolute values of $V_j = 20$ mV or higher. This V_j -dependent I_j deactivation is known as V_j -gating. Normalized steady-state junctional conductance, $G_{j,ss}$, was calculated for each tested V_j s to generate $G_{j,ss} - V_j$ plot (Fig. 2B open circles). The $G_{j,ss} - V_j$ plot could be well fitted with the Boltzmann equation for each V_j polarity (Fig. 2B, smooth dashed lines). Repeating the same experiments at increased temperatures, 28 °C or 32 °C, showed a similar $G_{j,ss} - V_j$ plots (Fig. 2B grey circles or black circles, respectively) and the respective Boltzmann fitting curves were similar to those obtained at 22 °C (Fig. 2B). The Boltzmann fitting parameters were similar at these tested temperatures with an exception of V_0 at positive V_j s (Table 1).

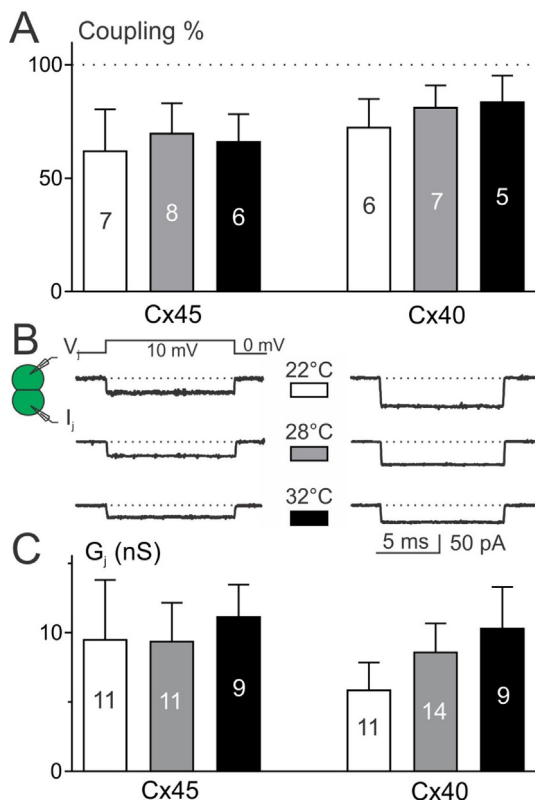


Fig. 1. Coupling percentage and conductance (G_j) were not affected by temperatures. (A) Coupling percentages of cell pairs expressing Cx45 or Cx40 are shown at 22 °C (white bars), 28 °C (grey bars), and 32 °C (black bars). The number of transfections is indicated. (B) Typical junctional currents (I_j) are shown in response to V_j (10 mV) for Cx45 GJs and Cx40 GJs at the indicated temperatures. (C) Averaged coupling conductance (G_j) of coupled cell pairs expressing Cx45 or Cx40. The number of cell pairs is indicated.

Different from Cx45 GJs, cell pairs expressing Cx40 showed no V_j -gating at ± 20 mV. Higher V_j s (± 40 to ± 100 mV) produced I_j deactivation at room temperature (22 °C, Fig. 3A). $G_{j,ss} - V_j$ plot was generated and could be well fitted with the Boltzmann equation for each V_j polarity (Fig. 3B). Similar V_j -gating was observed at elevated temperatures (28 °C and 32 °C) and the Boltzmann fittings were near identical to those obtained at room temperature (Fig. 3) without significant change in any of the fitting parameters (Table 1).

3.3. V_j -gating kinetics of Cx45 or Cx40 GJs at different temperatures

As shown in Fig. 2, the V_j -gating extent (steady-state to peak ratios) for Cx45 GJs were similar at different temperatures, but the I_j s appeared to have an accelerated kinetics. To investigate the detailed kinetics of I_j deactivations at the same V_j under different temperatures, the I_j deactivations were fitted to a single exponential process (with a time constant τ) at the initial part of I_j s. As shown in Fig. 4A, a single exponential process fitted well for each I_j s and higher temperatures showed faster kinetics with a lower τ values. The averaged time constants (τ s) for each tested V_j under different temperatures are plotted (Fig. 4B). A significant decrease in the time constants (τ s) when temperature was elevated from 22 °C to 28 °C ($P < 0.01$ for each tested V_j s), but no further decrease in the τ s was observed from 28 °C to 32 °C (Fig. 4B).

V_j -gating of Cx40 GJs was also investigated at different temperatures. Similar to those observed for Cx45 GJs, single exponential process fitted well for the I_j deactivation (Fig. 5A) and the time constants (τ s) were significantly decreased at each tested V_j s when temperature was increased from 22 °C to 28 °C, but no further decrease of the τ s were

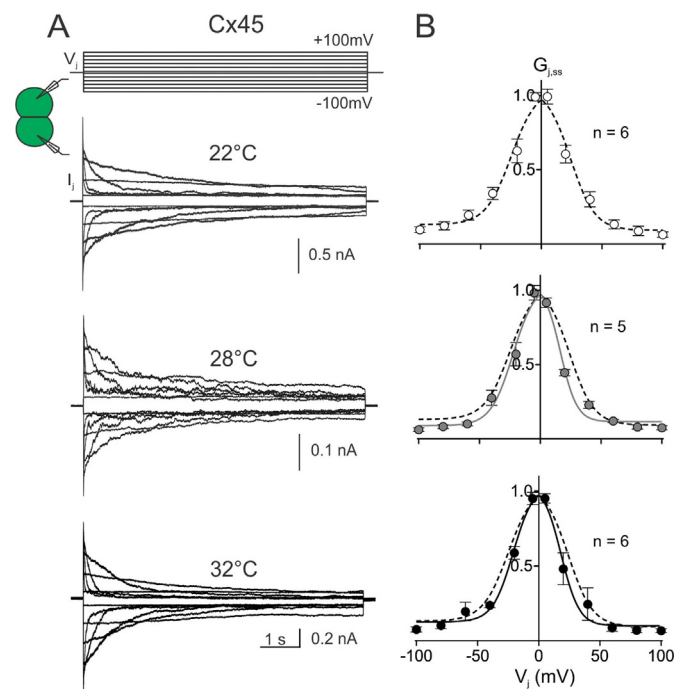


Fig. 2. V_j -gating of Cx45 gap junctions showed little change in the extent at tested temperatures. (A) Superimposed representative Cx45 junctional currents (I_j s) were displayed in response to the indicated V_j pulses (± 5 mV and ± 20 to ± 100 mV at 20 mV increment) at the indicated temperatures. (B) Normalized steady state junctional conductance, $G_{j,ss}$ of Cx45 GJs were plotted at different V_j s. The $G_{j,ss} - V_j$ plot was fitted with a two-state Boltzmann equation at each V_j polarity under different temperatures. The Boltzmann fitting curves at 22 °C (smooth dashed lines) were also plotted on those of 28 °C (smooth grey lines) and 32 °C (smooth black lines) for comparison. Number of cell pairs is indicated.

Table 1

Boltzmann fitting parameters for the V_j -gating of Cx45 and Cx40 gap junctions (GJs) at different temperatures.

GJ	Temp. (°C)	G_{min}	V_0 (mV)	A
Cx45	22	0.10 ± 0.03	24.2 ± 1.7	0.10 ± 0.01
	28	0.11 ± 0.02	$16.6 \pm 0.7^{*1}$	0.10 ± 0.01
	32	0.08 ± 0.02	$18.4 \pm 1.8^*$	0.13 ± 0.03
Cx40	22	0.21 ± 0.03	38.9 ± 1.5	0.18 ± 0.09
	28	0.18 ± 0.02	40.7 ± 1.0	0.16 ± 0.04
	32	0.19 ± 0.02	41.8 ± 1.4	0.15 ± 0.04

Data in this table were the Boltzmann fitting at the positive V_j polarity. The Boltzmann fitting parameters for negative V_j were similar for each GJ and therefore are not shown.

¹ One-way ANOVA was used to compare the corresponding parameters obtained at 22 °C.

* $P < 0.05$.

observed between 28 °C and 32 °C (Fig. 5B).

The rate of deactivation ($1/\tau$) was calculated at different V_j s and the $1/\tau - V_j$ plot could be well fitted by an exponential process for both Cx45 and Cx40 GJs under each of the tested temperatures (Supplemental Fig. 2). There is no statistically significant difference in the fitted exponential processes.

3.4. Faster recovery of Cx45 V_j -gating, but not that of Cx40, was observed with increased temperature

Large V_j (100 mV) induced a rapid I_j deactivation in Cx45 GJs. Removal of V_j was required to allow deactivated Cx45 GJs to recover back to an open state. To examine the recovery time course from Cx45

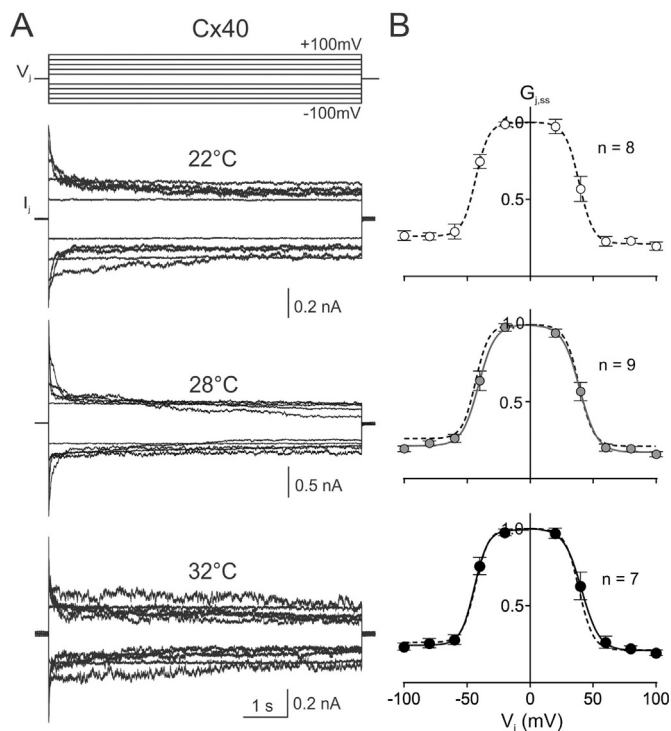


Fig. 3. V_j -gating of Cx40 gap junctions showed little change in the extent at tested temperatures. (A) Superimposed representative Cx40 junctional currents (I_j) were displayed in response to the indicated V_j pulses (± 20 to ± 100 mV) at the indicated temperatures. (B) Normalized steady state junctional conductance, $G_{j,ss}$, of Cx40 GJs were plotted at different V_j s. The $G_{j,ss} - V_j$ plot was fitted with a two-state Boltzmann equation at each V_j polarity under different temperatures. The Boltzmann fitting curves at 22 °C (smooth dashed lines) were also plotted on those of 28 °C (smooth grey lines) and 32 °C (smooth black lines) for comparison. Number of cell pairs is indicated.

GJ deactivation, a series of test V_j pulses were designed at different intervals after a pre-conditional V_j pulse at 22 °C. As shown in 6A, with the increase in the inter-pulse interval, the peak amplitude of I_j s to the test V_j pulses was recovered to a level near the pre-conditional V_j pulse induced I_j . The recovery percentage was plotted as a function of inter-pulse interval (Fig. 6B) and could be fitted well with a single exponential process with a time constant, $\tau = 3.7 \pm 0.9$ s, (Fig. 6B dashed line in the top panel). Increase temperature to 28 °C, the recovery from deactivation was faster with a significantly shorter time constant, $\tau = 2.0 \pm 0.4$ s, for the recovery plot (Fig. 6B middle panel). Further increase temperature to 32 °C, the time course of the recovery was similar to that at 28 °C with a time constant, $\tau = 2.0 \pm 0.1$ s (Fig. 6B bottom panel). The averaged peak recovery percentages were similar at all tested temperatures ($\sim 90\%$).

Different from those observed for Cx45 GJs, the recovery from deactivation of Cx40 GJs was very rapid, which prompt us to design a shorter double V_j pulse protocol to test the recovery time course. As shown in Fig. 7A, the amplitude of test pulse-induced I_j s was recovered quickly with the increase in the inter pulse interval. The recovery percentage – interval time plot was constructed and could be fitted well with a single exponential process ($\tau = 36 \pm 6$ ms, Fig. 7B). Increase temperature to 28 °C or 32 °C failed to change the recovery time constants ($\tau = 27 \pm 11$ ms and $\tau = 23 \pm 8$ ms, respectively, $P > 0.05$, Fig. 7B). The averaged peak recovery percentages were similar at all tested temperatures (~ 80 – 85%) for Cx40 GJs.

3.5. Dynamic modulation of Cx45 or Cx40 GJs at different temperatures

Cardiac action potentials (APs) show a variety of wave forms,

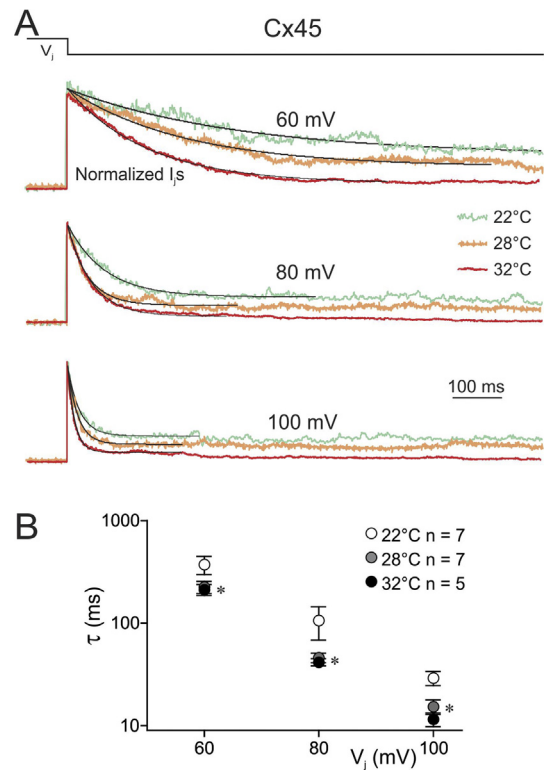


Fig. 4. Junctional current deactivation kinetics of Cx45 GJ changed under different temperatures. (A) Cx45 GJ junctional currents (I_j) at different temperatures are normalized to the same amplitude for easy comparison of deactivation kinetics at each tested V_j (60, 80, or 100 mV). Smooth black line on each I_j was a single exponential fit of the deactivation process. (B) The averaged time constants (τ s) of the exponential fit for each tested V_j at different temperatures are plotted. Number of cell pairs is indicated for each temperature.

typically with a rapid membrane depolarization, a sustained plateau phase with different durations, followed by a much slower repolarization phase. The onset depolarization phase of a cardiac AP is much faster than that of repolarization [27]. These AP properties together with transjunctional delay at the cell-cell junctions impose a large transient transjunctional voltage (V_j , near the full amplitude of an AP, ~ 100 mV) at the onset of AP followed by a moderate amplitude and prolonged V_j during the repolarization phase. If we assume the junctional delay is Δt and the repolarization takes ~ 70 ms, then a predicted V_j profile could be derived as shown in Fig. 8A (black dashed line under the AP). We simulated this temporal junctional voltage change with a V_j protocol (solid grey line) and applied such protocol for 50 times at a repeating frequency of one Hertz (1 Hz) to mimic regular heart rate (60 beats/min) or 3 Hz to mimic tachycardia (180 beats/min).

When such a V_j -protocol ($\Delta t = 10$ ms, 3 Hz for 50 times) applied onto a cell pair expressing Cx45, the G_j was gradually decreased to a much lower level (Fig. 8A,B). However, when the same V_j -protocol was applied onto cell pairs expressing Cx40, the G_j was not significantly changed during the entire time course (Fig. 8A,B). Reduce the repeating frequency of the V_j protocol from 3 Hz to 1 Hz, the Cx45 GJs showed less reduction in the G_j at the end of 50 cycles, while the G_j of Cx40 GJs remained unchanged during the entire 50 cycles. To quantitatively evaluate this V_j -protocol to reduce the G_j s of Cx45 or Cx40 GJs, the averaged conductance ratios ($G_j/G_{j,ini}$) were calculated from the last ten points (grey areas in Fig. 8B) and plotted as bar graph under different V_j -protocols, e.g. 3 Hz (Fig. 8C left panels) or 1 Hz (Fig. 8C right panels), different junctional delays (1, 3, 10 ms as indicated under each group of bars), as well as different temperatures (22 °C white bars, 28 °C grey bars, and 32 °C black bars). A significantly reduced G_j of Cx45 GJs was observed when $\Delta t = 10$ ms at 1 Hz, $\Delta t = 3$ ms at 3 Hz, or $\Delta t = 10$ ms at

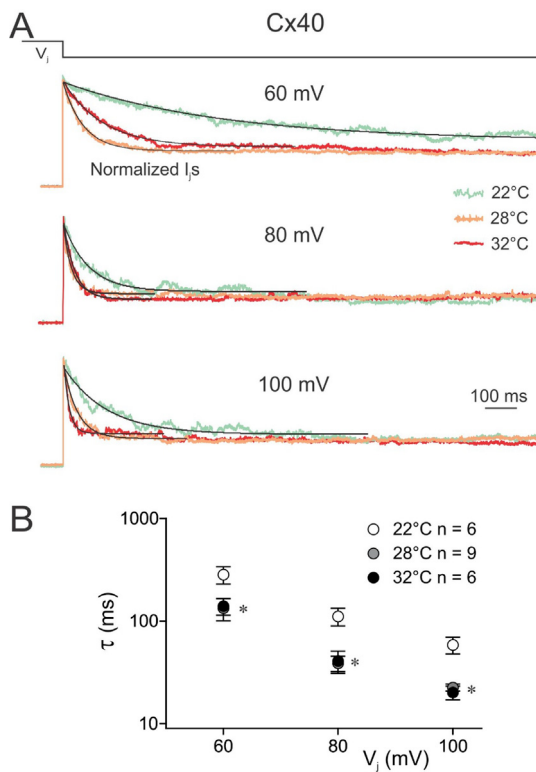


Fig. 5. Junctional current deactivation kinetics of Cx40 GJ changed under different temperatures. (A) Cx40 GJ junctional currents (I_j) at different temperatures are normalized to the same amplitude for easy comparison of deactivation kinetics at each tested V_j (60, 80, or 100 mV). Smooth black line on each I_j was a single exponential fit of the deactivation process. (B) The averaged time constants (τ s) of the exponential fit for each tested V_j at different temperatures are plotted. Number of cell pairs is indicated for each temperature.

3 Hz (Fig. 8C top panels). The Cx45 G_j reduction was consistent at all tested temperatures, indicating this dynamic uncoupling is temperature-independent at our tested temperatures. Other V_j -protocols ($\Delta t = 1$ ms at 1 or 3 Hz, $\Delta t = 3$ ms at 1 Hz) failed to cause a significant reduction of Cx45 G_j (Fig. 8C top panels). Distinct from Cx45 G_js, the G_j of Cx40 G_js showed no change at any of our tested V_j -protocols and any tested temperatures (Fig. 8C bottom panels).

4. Discussion

In this study, we investigated temperature effects on V_j -gating properties of two cardiac G_js. In the case of Cx45 G_js, increased temperature from 22 °C to 28 °C (or 32 °C) led to an accelerated V_j -dependent deactivation with little change in the extent of V_j -gating (a minimum change in Boltzmann parameter, G_{min}) at the tested V_j range. The rate of recovery from deactivation of Cx45 G_js was also accelerated at higher temperatures. The dynamic uncoupling with our designed protocol was evident in Cx45 G_js when sufficient junctional delay and/or repeating frequency provided. However, in the same tested temperatures Cx40 G_js showed no change in the rate of recovery from deactivation, no change in the Boltzmann fitting parameters for the V_j -gating, and no dynamic uncoupling in any of our tested junctional delays and/or repeating frequencies. The only temperature-dependent effect of Cx40 G_js was an accelerated V_j -dependent deactivation kinetics. The time constants of the recovery time course from deactivation of Cx40 G_js were much shorter (~70–100 fold shorter) than those of Cx45 G_js. The unique dynamic uncoupling of Cx45 G_js may play a role in a slower AV node conduction and preventing high rate of ventricular beating from fibrillating atria in atrial fibrillation patients.

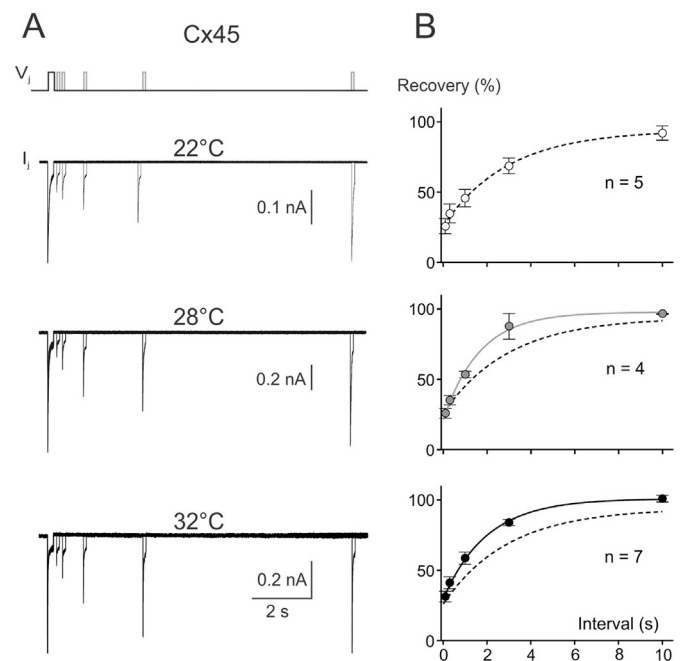


Fig. 6. Recovery from Cx45 I_j deactivation was faster at higher temperatures. (A) A double voltage pulse protocol as shown at the top was used to study the recovery time course of Cx45 I_j deactivation. The initial conditional V_j pulse (100 mV for 200 ms) was used to deactivate Cx45 G_js, which was followed by a test V_j pulse (100 mV for 100 ms) at different inter pulse intervals (0.1, 0.3, 1, 3, 10 s). The test V_j -induced I_j s were gradually recovered with the increase in the inter pulse interval. Increase temperature from 22 °C to 28 °C or 32 °C, the recovery appeared to be faster. (B) The recovery percentage from deactivation was calculated and was plotted as a function of inter pulse interval. The data on each plot can be fitted well with a single exponential time course with a time constant, $\tau = 3.7 \pm 0.9$ s at 22 °C (smooth dashed lines on each plot), $\tau = 2.0 \pm 0.4$ s at 28 °C (smooth grey line), or $\tau = 2.0 \pm 0.1$ s at 32 °C (smooth black line).

4.1. Effects of temperature on the V_j -gating kinetics of Cx40 and Cx45 G_js and dynamic uncoupling

We found that the V_j -gating of both Cx40 and Cx45 G_js could be fitted well by a single exponential process in the range of V_j values between 60 and 100 mV (Figs. 4 and 5). A faster kinetics (or smaller time constants, τ s) was observed when temperature was elevated from 22 °C to 28 °C for both G_js. However, further elevation of temperature from 28 °C to 32 °C, we did not observe any significant further increase in the kinetics of V_j -gating. The following two factors could play a role in this observation. 1) The effects of temperature on the gating kinetics are not linear for both G_js and might have been saturated in the range of temperatures 28–32 °C. This hypothesis is qualitatively consistent with the observations on several other voltage-gated ion channels with a non-linear change in the gating kinetics [28,29]. 2) Some fluctuations in measured V_j -gating kinetics are unavoidable for dual whole cell voltage clamp (e.g. stability of whole cell access, and/or coupling level) [24,30,31]. This system error together with a relatively lower temperature gap (4 degrees from 28 to 32 °C) might have prevented us from observing some small kinetic changes. We did try to perform dual patch clamp at 34 °C or higher and unfortunately dual patch clamp at these high temperatures were too unstable to yield enough meaningful data. With this technical limitation, we chose to rely on extrapolation of kinetic changes in 22–28 °C to estimate Q10. Our estimated Q10 for deactivation and recovery from deactivation of Cx45 GJ at $V_j = 100$ mV were 3.1 and 2.9, respectively. For Cx40 GJ at the same V_j , the Q10 of deactivation and recovery from deactivation were 4.0 and 1.6, respectively. These Q10 values of these G_js fall into the commonly

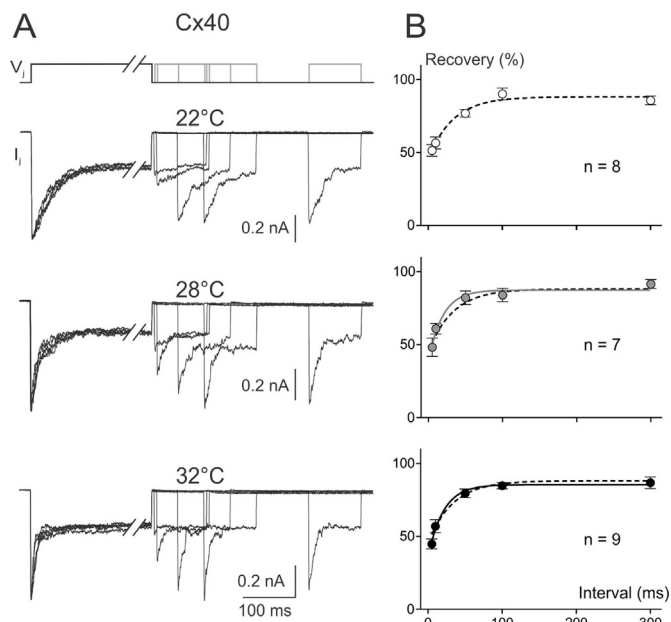


Fig. 7. Recovery from Cx40 I_j deactivation was not different at the tested temperatures. (A) A double voltage pulse protocol as shown at the top was used to study the recovery time course of Cx40 I_j deactivation. The initial conditional V_j pulse (100 mV for 600 ms) was used to deactivate Cx40 GJs, which was followed by a test V_j pulse (100 mV for 100 ms) at different inter pulse intervals (5, 10, 50, 100, 300 ms). The test V_j -induced I_j s were gradually recovered with the increase in the inter pulse interval for all tested temperatures. (B) The recovery percentage from deactivation was plotted as a function of inter pulse interval. The data on each plot can be fitted well with a single exponential time course with a time constant, $\tau = 36 \pm 6$ ms at 22 °C (smooth dashed lines on each plot), $\tau = 27 \pm 11$ ms at 28 °C (smooth grey line), or $\tau = 23 \pm 8$ ms at 32 °C (smooth black line). These τ s are not statistically different.

observed range 2–4 for many other ion channels [32].

We speculate that increasing temperature to human body temperature (37 °C) is likely to accelerate the gating kinetics of Cx45 or Cx40 GJs, which could lead to more dynamic uncoupling (or accumulation of deactivated GJs) with our designed V_j protocols. Currently experimental evidence for the deactivation kinetics of V_j -gating of these GJs at 37 °C remains to be determined. In addition to the deactivation kinetics, we have recognized that the recovery kinetics from deactivation of these GJs also played a key role in the dynamic uncoupling, e.g. a faster recovery kinetic with higher temperatures could play an opposite role, i.e. decreasing dynamic uncoupling. Our experimental results showed that for Cx45 GJs, the recovery time course at 22 °C ($\tau = 3.7$ s) was accelerated when temperature was increased to 28 °C or 32 °C (both cases, the $\tau = 2$ s). Interestingly, the dynamic uncoupling with our designed V_j protocols was sustained and not changed significantly at any of these temperatures, indicating that the temperature dependent increase in deactivation kinetics was balanced by a temperature dependent increase in the recovery kinetics of Cx45 GJs resulting in similar accumulation of deactivated GJs in these V_j protocols. In the case of Cx40 GJs, the recovery kinetics from deactivation was ($\tau = 0.036$ s) about two orders faster than that of Cx45 GJs and we observed a slightly lower, but not statistically different, time constants ($\tau = 0.027$ s for 28 °C and 0.023 s for 32 °C) for the recovery kinetics. We believe that these much faster recovery kinetics of Cx40 GJs are responsible for our failure to observe any dynamic uncoupling with tested junctional delays (1–10 ms) and repeating frequencies (1–3 Hz).

Consistent with our results, an early study using dual patch clamp on chick ventricular myocytes also reported a temperature dependent increase in the GJ V_j -gating kinetics, including a faster deactivation kinetics and a faster recovery kinetics for the recovery from deactivation [33]. The authors did not do any quantitative analysis of Q10 for

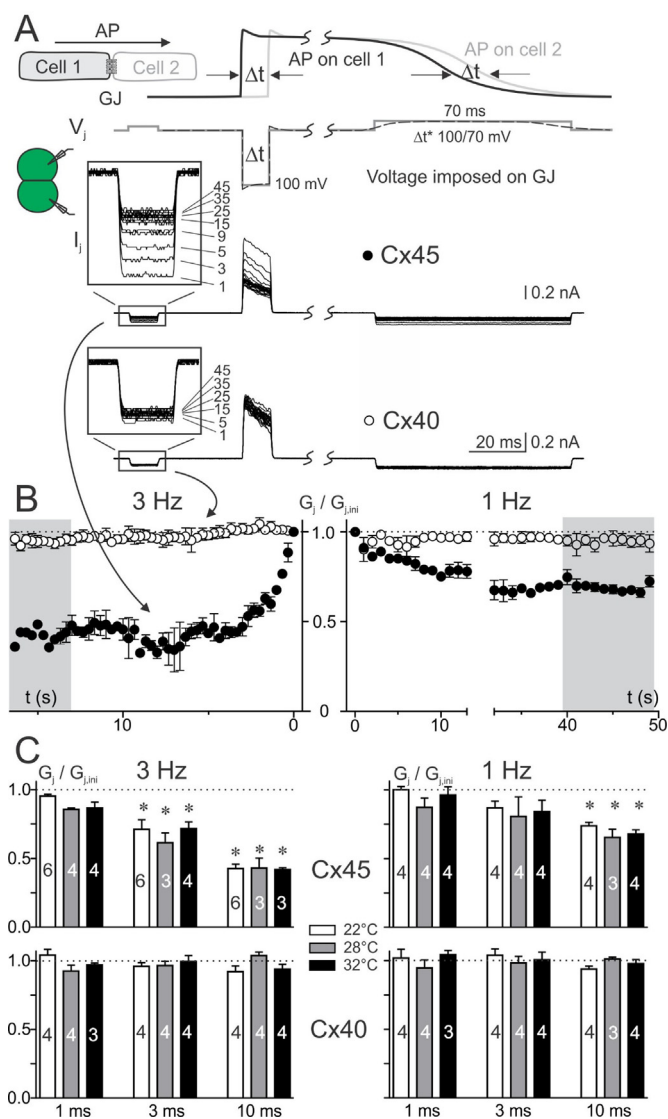


Fig. 8. Dynamic uncoupling was observed in Cx45 GJs, but not in Cx40 GJs, at the tested temperatures. (A) A generic cardiac action potential (AP) propagates from Cell 1 (black) to Cell 2 (grey) with a junctional delay of Δt . Due to that cardiac AP possesses a fast depolarization and a slower repolarization, the voltage imposed on the GJs (dashed lines) was predicted to have a large transient V_j (~ 100 mV with a duration of Δt) followed by a lower V_j during the entire repolarization phase. A V_j -protocol was designed to simulate the voltage changes on the GJs assuming the repolarization phase is ~ 70 ms (grey line). When a V_j -protocol with junctional delay, $\Delta t = 10$ ms, was applied to a cell pair expressing Cx45 at a repeating frequency of 3 Hz for 50 cycles, a reduction in the G_j was observed reaching a steady state level of coupling after ~ 15 V_j protocols (see enlarged inset). In contrast, the same V_j protocol failed to reduce G_j in Cx40 GJs. Note that we only displayed all odd numbered records for both Cx45 and Cx40 GJs. (B) The coupling conductance was normalized to the initial coupling conductance ($G_j/G_{j,ini}$) and plotted with time during the 50 cycles at 3 Hz (left panel) or at 1 Hz (right panel). Note that Cx45 GJs (black circles) showed frequency and junctional delay time dependent uncoupling during the 50 cycles, while Cx40 GJs (white circles) showed no change in G_j under the same conditions. The average of last 10 points in the light grey zone was used to generate the bar graph below. (C) The average of last 10 normalized G_j ratio ($G_j/G_{j,ini}$) from experiments described above was plotted as bar graph to show the coupling level change under different experimental conditions. The Cx45 GJs showed a significant G_j reduction at $\Delta t = 3$, or 10 ms at 3 Hz, or $\Delta t = 10$ ms at 1 Hz in every tested temperature (top panels). The dynamic uncoupling of Cx45 GJs were sustained at similar levels at all three tested temperatures. While Cx40 GJs showed no change in G_j in any of our tested conditions (bottom panels).

these gating kinetics, but observed a Q10 of coupling conductance changes to be 2.2 in the temperature range of 21–26 °C and a higher Q10 of 6.5 in the temperature range of 14–21 °C [33]. We did not observe any statistically significant temperature-dependent conductance change in either Cx45 or Cx40 GJs (see Fig. 1 and Supplemental Fig. 1), which might be due to the follow reasons: 1) the human Cx45 or Cx40 GJs may have little temperature-dependent conductance (G_j) changes from those GJs in the young chick ventricular myocytes; 2) perhaps that there could be a temperature-dependent change in the G_j of Cx45 or Cx40 GJs, but in our tested temperature range (22–32 °C) the G_j changes could be too small to be detected with our way of measuring G_j , i.e. non-paired data at different temperatures due to limited time window to perform stable dual patch clamp in combination with large variations in the G_j of different cell pairs. Future systematic study on same cell pairs at different temperatures may help to resolve this issue.

Dynamic down regulation of G_j have been observed in vitro on expressed rat Cx43 and Cx40 GJs using a simulated cardiac action potential as V_j [21,22]. Similar GJ uncoupling was also demonstrated in cultured mouse ventricular myocytes using the same V_j protocols [20]. Rotigaptide, an anti-arrhythmia agent, was able to dose-dependently decrease the GJ deactivation extent and kinetics, which could be partially responsible for the reduction in the dynamic uncoupling in mouse ventricular myocytes [34]. It is important to note that the peak reduction in the G_j in these studies was during the plateau phase (~50%) of a cardiac action potential [20–22], unlike the present study the G_j was reduced at the resting level (not during a V_j -protocol) due to an accumulation of deactivated GJs. It would be very interesting to see if rotigaptide is able to modify the dynamic uncoupling of Cx45 GJs.

Our results were obtained using in vitro expression in GJ-deficient model cells, where we are able to have a good control over expressed connexin type. Whether the endogenously expressed Cx40 or Cx45 GJs in various regions of the heart also possess similar temperature dependent V_j -gating kinetic changes remains to be determined.

4.2. Cardiac action potential propagation in different regions of the heart

A cardiac cycle can be described as a sequence of electrical (action potentials, APs) followed by mechanical (contractions) events in different regions of the heart to ensure a rhythmic well-coordinated contractions to pump blood into the circulation system [35]. The APs generated in the SA node propagate rapidly throughout the atria and converge at the AV node, where a much slower propagation velocity is observed forming an apparent delay at the AV node (known as AV delay). After going through the AV node, the AP propagation velocity accelerates into a much faster speed in the ventricular conduction system (his bundle, bundle branches, and Purkinje fibers) to reach ventricular myocardium leading to synchronized activation of ventricles [10,36,37]. There are several factors responsible for different propagation velocity in different regions of the heart, including the cell types and their size and shape, the cell excitability largely determined by the abundance and distribution of ion channels (e.g. Na^+ , Ca^{2+} , and K^+ channels) and transporters, and the effectiveness of gap junctional intercellular communication between cardiomyocytes. Gap junctional intercellular communication is measured quantitatively by coupling conductance (G_j). The higher the G_j , the faster the current spreads from one cell to another resulting faster propagation velocity [38,39]. The G_j is determined by the total number of GJ channels between cells, the single channel conductance of each GJ channel, and their functional states (fully open, subconductance, or closed states). The GJ functional states can be dynamically modulated by chemicals and transjunctional voltage (V_j). Transjunctional voltage-dependent gating (V_j -gating) is an intrinsic property in all characterized GJs. Among the three cardiac connexins, Cx43 GJs showed the lowest V_j -gating extent (reflected by a higher G_{min} , 0.2–0.6, a Boltzmann fitting parameter for $G_{j,ss} - V_j$ relationship), a higher level of V_j to deactivate half GJ channels (the Boltzmann parameter V_0), and much slower deactivation kinetics

comparing to those of Cx40 or Cx45 GJs [40–43]. The recovery from deactivation of Cx43 GJ was also very rapid with 82% recovery observed with only 30 ms interval with a simulated cardiac AP as V_j [22]. These properties make the Cx43 GJ the most robust GJ in the heart in terms of V_j modulation and interestingly the Cx43 is the most abundant connexin subtype in all regions of the heart except in the nodal cells. At individual channel level, Cx43 GJ showed a moderate level of single channel conductance of ~100 pS with multiple levels of sub-conductance states [12]. The second abundant connexin subtypes in the heart is Cx40. Cx40 is expressed together with Cx43 and Cx45 in the atria and the ventricular conduction system [3,5,6]. The GJs formed by Cx40 showed the largest single channel conductance (~160 pS) among cardiac connexins and therefore require a smaller number of GJs to achieve the same level of coupling. Cx40 GJ showed a strong V_j -gating (with $G_{\text{min}} \sim 0.2$ and $V_0 \sim 40$ mV) when studied at room temperature [23]. Here we showed for the first time that elevation of temperatures from 22 °C to 28 °C or 32 °C, had no effect on the coupling conductance (G_j) in our model cells expressing Cx40 (Fig. 1 and Supplemental Fig. 1). The only significant temperature-dependent change was an increased deactivation kinetics of the GJ. However, the recovery from deactivation of Cx40 GJ appear to be very rapid and temperature-insensitive. The least abundant cardiac connexin in the human heart is Cx45, whose distribution is mostly restricted to the nodal cells in SA and AV nodes. The single channel conductance of Cx45 GJ (~35 pS) is the lowest among cardiac connexins [12,44], which means that a much higher number of Cx45 GJs is required to reach the same level of G_j . Interestingly, Cx45 GJs displayed the strongest V_j -gating defined by the following parameters: 1) a very low level of G_{min} (~0.1), which means that about 90% GJs can be closed when sufficient V_j s are provided; 2) lowest level of V_j s required to have 50% V_j -gating (~20 mV for V_0); 3) V_j -dependent deactivation kinetics was the fastest among cardiac connexins and higher temperature accelerated this kinetic process even more (Fig. 4). 4) A much slower recovery from deactivated GJs than that of Cx40 GJ (Fig. 6). These unique properties of Cx45 GJ make it the most vulnerable for V_j -dependent dynamic modulation of the coupling conductance (G_j). Our designed junctional delay derived V_j protocol demonstrated that indeed Cx45 GJs could be dynamically uncoupled when sufficient junctional delays and repeating frequency are provided.

4.3. GJ coupling level is an important contributing factor to alter AV delay

Many structural and functional factors contribute to AV nodal delay, including 1) smaller cell size in the node which increases the number of cell junctions, where the AP propagation is much slower [45]; 2) complex cell architecture and the presence of non-excitabile tissues (working as insulators) that increase the passage length for the propagation in the AV node [10,46]; 3) intrinsic electrical properties of AV nodal cells [47,48], including a relative low expression of the Na^+ channels [49,50] responsible for the onset of AP depolarization which would slow the rate of AP depolarization and reduce AP amplitude [51], different set of K^+ channels from those in atrial/ventricular myocytes which resulted in a more depolarized resting membrane potential and different shape of the APs [10,27,50,52]; 4) a lower GJ coupling in the AV node [37].

Human AV node GJs are mostly composed of Cx45 without Cx31.9, unlike the mouse nodal cells where both Cx45 and a homolog of human Cx31.9, Cx30.2, are expressed and appeared to be redundant [53]. Most of the human AV nodal GJs are predicted to be homotypic Cx45 GJs with possible involvement of heterotypic GJs at the borders linking to atria or His bundle (both tissues expressing Cx43 and Cx40) [3–5,37]. According to a previous study that human Cx40 was unable to form heterotypic GJs with human Cx45 [19], which make two main functional AV nodal GJs being either homotypic Cx45 or heterotypic Cx45/Cx43 GJs. As discussed above, Cx45 GJs showed the lowest level of single channel conductance (γ_j), the most prominent V_j -gating, and the fastest V_j -gating kinetics among the cardiac connexins. In addition,

immunolabeling study showed that Cx45 commonly formed much smaller GJ plaques at the cell junctions, which indicated a lower number of GJs at the nodal junctions [3,8]. For heterotypic cell junctions of expressing Cx45 in one and Cx43 in the other, we have experimental evidence that heterotypic Cx43/Cx45 GJs are functional and displayed asymmetric V_j -gating with gating observed when Cx45 cell was with $-V_j$. The Boltzmann V_j -gating parameters of this heterotypic Cx43/Cx45 GJ were very much similar to those observed with homotypic Cx45 GJs indicating that the gating of the heterotypic GJs was likely due to Cx45 connexon gating not the Cx43 connexon [19]. It is not clear that if heterotypic Cx43/Cx45 GJs are also temperature dependent similar to those observed for Cx45 GJs, this would be an interesting topic for future studies.

In conclusion, increasing in temperature increased deactivation gating kinetics of Cx40 and Cx45 GJs, increased the recovery kinetics of Cx45 GJs from deactivation. However, the extent of V_j -gating of both GJs and the recovery kinetics of Cx40 GJs showed little temperature dependence in the tested temperature range. Sufficiently long junctional delays at regular or elevated heart beating frequency could cause uncoupling of Cx45 GJs, but not Cx40 GJs.

Funding

This work was supported by Canadian Institutes of Health Research (153415 to D.B.). A.S.-M. was supported by a grant from FAPEMIG from Brazil.

Acknowledgments

We thank Honghong Chen for her technical help in amplification of expression vectors.

Conflict of interest

None declared.

Author contributions

A.S.-M. designed and performed most patch clamp experiments, analyzed data, and wrote an early draft of the manuscript. M.N. designed and performed some patch clamp experiments and analyzed data. D.B. designed the project, supervised data analysis and critically revised the manuscript.

Appendix A. Supplementary data

Supplementary data to this article can be found online at <https://doi.org/10.1016/j.yjmcc.2018.12.014>.

References

- G. Sohl, K. Willecke, Gap junctions and the connexin protein family, *Cardiovasc. Res.* 62 (2) (2004) 228–232.
- D. Bai, Structural analysis of key gap junction domains—Lessons from genome data and disease-linked mutants, *Semin. Cell Dev. Biol.* 50 (2016) 74–82.
- L.M. Davis, et al., Gap junction protein phenotypes of the human heart and conduction system, *J. Cardiovasc. Electrophysiol.* 6 (10 Pt 1) (1995) 813–822.
- C. Vozzi, et al., Chamber-related differences in connexin expression in the human heart, *J. Mol. Cell. Cardiol.* 31 (5) (1999) 991–1003.
- P. Kanagaratnam, et al., Relative expression of immunolocalized connexins 40 and 43 correlates with human atrial conduction properties, *J. Am. Coll. Cardiol.* 39 (1) (2002) 116–123.
- D.B. Gros, H.J. Jongsma, Connexins in mammalian heart function, *BioEssays* 18 (9) (1996) 719–730.
- R.G. Gourdie, et al., The spatial distribution and relative abundance of gap-junctional connexin40 and connexin43 correlate to functional properties of components of the cardiac atrioventricular conduction system, *J. Cell Sci.* 105 (1993) 985–991.
- M.R. Boyett, et al., Connexins in the sinoatrial and atrioventricular nodes, *Cardiovasc. Gap Junctions* 42 (2006) 175–197.
- I.R. Efimov, et al., Structure-function relationship in the AV junction, *Anat Rec A Discov Mol Cell Evol Biol* 280 (2) (2004) 952–965.
- I.D. Greener, et al., Molecular architecture of the human specialised atrioventricular conduction axis, *J. Mol. Cell. Cardiol.* 50 (4) (2011) 642–651.
- N. Palacios-Prado, et al., pH-dependent modulation of voltage gating in connexin45 homotypic and connexin45/connexin43 heterotypic gap junctions, *Proc. Natl. Acad. Sci. U. S. A.* 107 (21) (2010) 9897–9902.
- F.F. Bukauskas, et al., Coupling asymmetry of heterotypic connexin 45/connexin 43-EGFP gap junctions: properties of fast and slow gating mechanisms, *Proc. Natl. Acad. Sci. U. S. A.* 99 (10) (2002) 7113–7118.
- A.P. Moreno, et al., Properties of gap junction channels formed of connexin 45 endogenously expressed in human hepatoma (SKHep1) cells, *Am. J. Phys.* 268 (2 Pt 1) (1995) C356–C365.
- G.T. Cottrell, Y. Wu, J.M. Burt, Cx40 and Cx43 expression ratio influences heteromeric/heterotypic gap junction channel properties, *Am. J. Phys. Cell Physiol.* 282 (6) (2002) C1469–C1482.
- G.T. Cottrell, J.M. Burt, Heterotypic gap junction channel formation between heteromeric and homomeric Cx40 and Cx43 connexons, *Am. J. Phys. Cell Physiol.* 281 (5) (2001) C1559–C1567.
- V. Valiunas, et al., Gap junction channels formed by coexpressed connexin40 and connexin43, *Am. J. Physiol. Heart Circ. Physiol.* 281 (4) (2001) H1675–H1689.
- V. Valiunas, R. Weingart, P.R. Brink, Formation of heterotypic gap junction channels by connexins 40 and 43, *Circ. Res.* 86 (2) (2000) E42–E49.
- D.S. He, et al., Formation of heteromeric gap junction channels by connexins 40 and 43 in vascular smooth muscle cells, *Proc. Natl. Acad. Sci. U. S. A.* 96 (11) (1999) 6495–6500.
- W.G. Ye, et al., Junctional delay, frequency, and direction-dependent uncoupling of human heterotypic Cx45/Cx43 gap junction channels, *J. Mol. Cell. Cardiol.* 111 (2017) 17–26.
- X. Lin, et al., Dynamic model for ventricular junctional conductance during the cardiac action potential, *Am. J. Physiol. Heart Circ. Physiol.* 288 (3) (2005) H1113–H1123.
- X. Lin, R.D. Veenstra, Action potential modulation of connexin40 gap junctional conductance, *Am. J. Physiol. Heart Circ. Physiol.* 286 (5) (2004) H1726–H1735.
- X. Lin, M. Crye, R.D. Veenstra, Regulation of connexin43 gap junctional conductance by ventricular action potentials, *Circ. Res.* 93 (6) (2003) e63–e73.
- Y. Sun, et al., Novel germline GJA5/connexin40 mutations associated with lone atrial fibrillation impair gap junctional intercellular communication, *Hum. Mutat.* 34 (4) (2013) 603–609.
- D. Bai, J. Cameron, D. Bai, J.C. Saez (Eds.), Patch Clamp Analysis of Gap Junction Channel Properties. Gap Junction Channels and Hemichannels, CRC Press Taylor & Francis Group, London, UK, 2016, pp. 93–114.
- L. Xin, D. Bai, Functional roles of the amino terminal domain in determining biophysical properties of Cx50 gap junction channels, *Front. Physiol.* 4 (2013) 373.
- X. Tong, et al., Charge at the 46th residue of connexin50 is crucial for the gap-junctional unitary conductance and transjunctional voltage-dependent gating, *J. Physiol.* 592 (Pt 23) (2014) 5187–5202.
- J.M. Nerbonne, R.S. Kass, Molecular physiology of cardiac repolarization, *Physiol. Rev.* 85 (4) (2005) 1205–1253.
- T.E. DeCoursey, V.V. Cherny, Temperature dependence of voltage-gated H⁺ currents in human neutrophils, rat alveolar epithelial cells, and mammalian phagocytes, *J. Gen. Physiol.* 112 (4) (1998) 503–522.
- A.D. Rosen, Nonlinear temperature modulation of sodium channel kinetics in GH(3) cells, *Biochim. Biophys. Acta* 1511 (2) (2001) 391–396.
- R. Wilders, H.J. Jongsma, Limitations of the dual voltage clamp method in assaying conductance and kinetics of gap junction channels, *Biophys. J.* 63 (4) (1992) 942–953.
- H.V. Van Rijen, et al., Quantitative analysis of dual whole-cell voltage-clamp determination of gap junctional conductance, *Arch. Eur. J. Physiol.* 436 (1) (1998) 141–151.
- B. Hille, *Ion Channels of Excitable Membrane*, 3rd ed., Sinauer Associates, Inc., Massachusetts, 2001.
- Y.H. Chen, R.L. DeHaan, Temperature dependence of embryonic cardiac gap junction conductance and channel kinetics, *J. Membr. Biol.* 136 (2) (1993) 125–134.
- X. Lin, et al., Enhancement of ventricular gap-junction coupling by rotigaptide, *Cardiovasc. Res.* 79 (3) (2008) 416–426.
- W.F. Boron, E.L. Boulpaep, *Medical Physiology*, Elsevier, Philadelphia, 2017.
- J.R. de Groot, et al., Conduction slowing by the gap junctional uncoupler carbenoxolone, *Cardiovasc. Res.* 60 (2) (2003) 288–297.
- I.P. Temple, et al., Connexins and the atrioventricular node, *Heart Rhythm.* 10 (2) (2013) 297–304.
- S. Rohr, Role of gap junctions in the propagation of the cardiac action potential, *Cardiovasc. Res.* 62 (2) (2004) 309–322.
- S. Rohr, J.P. Kucera, A.G. Kleber, Slow conduction in cardiac tissue, I - Effects of a reduction of excitability versus a reduction of electrical coupling on micro-conduction, *Circ. Res.* 83 (8) (1998) 781–794.
- F.F. Bukauskas, et al., Gating properties of gap junction channels assembled from connexin43 and connexin43 fused with green fluorescent protein, *Biophys. J.* 81 (1) (2001) 137–152.
- A. Revilla, M.V. Bennett, L.C. Barrio, Molecular determinants of membrane potential dependence in vertebrate gap junction channels, *Proc. Natl. Acad. Sci. U. S. A.* 97 (2002) (2000) 14760–14765.
- K. Banach, R. Weingart, Connexin43 gap junctions exhibit asymmetrical gating properties, *Pflugers Arch.* 431 (5) (1996) 775–785.
- T.W. White, et al., Selective interactions among the multiple connexin proteins expressed in the vertebrate lens: the second extracellular domain is a determinant of

- compatibility between connexins, *J. Cell Biol.* 125 (4) (1994) 879–892.
- [44] S. Elenes, et al., Heterotypic docking of Cx43 and Cx45 connexons blocks fast voltage gating of Cx43, *Biophys. J.* 81 (3) (2001) 1406–1418.
- [45] F.L. Meijler, M.J. Janse, Morphology and electrophysiology of the mammalian atrioventricular node, *Physiol. Rev.* 68 (2) (1988) 608–647.
- [46] R.H. Anderson, et al., The anatomy of the cardiac conduction system, *Clin. Anat.* 22 (1) (2009) 99–113.
- [47] B.F. Hoffman, et al., Electrical activity of single fibers of the atrioventricular node, *Circ. Res.* 7 (1) (1959) 11–18.
- [48] C.A. de, A.D. de, Spread of activity through the atrioventricular node, *Circ. Res.* 8 (1960) 801–809.
- [49] S. Yoo, et al., Localization of Na⁺ channel isoforms at the atrioventricular junction and atrioventricular node in the rat, *Circulation* 114 (13) (2006) 1360–1371.
- [50] I.D. Greener, et al., Ion channel transcript expression at the rabbit atrioventricular conduction axis. *Circulation, Arrhythmia Electrophysiol.* 2 (3) (2009) 305–315.
- [51] E. Patterson, B.J. Scherlag, Decremental conduction in the posterior and anterior AV nodal inputs, *J. Interv. Card. Electrophysiol.* 7 (2) (2002) 137–148.
- [52] L. Marger, et al., Pacemaker activity and ionic currents in mouse atrioventricular node cells, *Channels (Austin)* 5 (3) (2011) 241–250.
- [53] M.M. Kreuzberg, K. Willecke, F.F. Bukauskas, Connexin-mediated cardiac impulse propagation: connexin 30.2 slows atrioventricular conduction in mouse heart, *Trends Cardiovasc. Med.* 16 (8) (2006) 266–272.

Capítulo 3:

EFEITOS DIRETOS DA
HIPERCOLESTEROLEMIA NA
FUNÇÃO CARDÍACA E DE
CARDIOMIÓCITOS

Early stage hypercholesterolemia with increased cardiomyocytes' cholesterol content promoted remodeling of Ca²⁺ handling and excitability in a murine model.

Santos-Miranda A¹; Joviano-Santos JV²; Roman-Campos-D³; Almeida JFQ⁴; Ferraz V⁵; Alvarez-Leite JI¹; Cruz JS¹

¹ Department of Biochemistry and immunology, Federal University of Minas Gerais, Brazil; ² Department of Morphology, Federal University of Minas Gerais, Brazil; ³ Department of Biophysics, Federal University of São Paulo, Brazil; ⁴ Department of Physiology and Biophysics, Federal University of Minas Gerais, Brazil; ⁵ Department of Chemistry, Federal University of Minas Gerais, Brazil.

Corresponding author:

Jader S. Cruz, PhD

Department of Biochemistry and Immunology, Federal University of Minas Gerais, Av. Antônio Carlos, 6627 – 31.270-901 – Belo Horizonte, MG, Brazil. email: jcruz@ufmg.br

All authors declare no conflict of interest.

ABSTRACT

Hypercholesterolemia is a hyperlipidemia disorder characterized by elevated circulating levels of total cholesterol. Hypercholesterolemia-linked increase in the risk to develop cardiovascular diseases has long been investigated, however mostly associated with vascular dysfunction and atherosclerotic lesions, while evidence of direct effects of hypercholesterolemia on heart function is still incomplete and controversial. Manipulation of cell cholesterol content through the use of cyclodextrins and exposure to lipoproteins suggests that cholesterol-enriched domains plays an important role in the function of ion channels and secondary messengers, and therefore could significantly affect cardiomyocytes function. In this study, we assessed the direct effects of hypercholesterolemia in the heart and in isolated cardiomyocytes electrical and contractile functions. After 5 weeks male Swiss mice fed with AIN-93 diet added with 1.25% cholesterol develop an increase in total serum cholesterol levels and in cellular cholesterol content. Isolated cardiomyocytes displayed modulation of action potential waveform, followed by increasing I_K , reducing I_{Ca} and alterations in Ca^{2+} handling. Contractile function was comparable to control mice, fed with AIN-93 without cholesterol supplementation. Ischemia and reperfusion had similar effects on contractile properties of isolated hearts from hypercholesterolemic mice, however, with partial protection against arrhythmias. Electrocardiographic records were similar between experimental groups, apart from a slight shortening of QT interval. Our findings contribute to elucidate the role of high circulating cholesterol in the modulation of cardiac electro-mechanical properties, providing substantial insights to understand hypercholesterolemia-related cardiovascular dysfunctions.

INTRODUCTION

Hypercholesterolemia is a type of hyperlipidemia disorder in which there is elevated circulating levels of total cholesterol. Hypercholesterolemia may arise as a consequence defect in the gene encoding the LDL receptor (for familial hypercholesterolemia), or due to metabolic disorders associated with an unbalanced diet, including obesity and diabetes [1]. Association between hypercholesterolemia and cardiovascular diseases (CVD) has long been investigated [2], [3]. Over the subsequent years, epidemiological data stretched the role of dyslipidemias, particularly hypercholesterolemia playing a crucial role in the establishment and progression of CVD [4], [5], [6], [7], [8] and several trials have demonstrated that lowering cholesterol levels, primarily LDL-containing cholesterol, are effective in ameliorating vascular dysfunction and mortality [9].

The accumulation of LDL-cholesterol over time driving the formation of foam cells with a consecutive proliferation of atherosclerotic lesions is well understood as increasing the risk of CVD [10], [11]. However, apart from vascular-dependent cardiac overload and malfunction, direct effects of hypercholesterolemia on heart mechanic and electrical properties are less abundant and not conclusive. It seems to be a consensus that hypercholesterolemia induces additional myocardial damage and dysfunction during Ischemia/Reperfusion (IR) injury [12], [13] and, turns the heart insensitive to ischemic preconditioning and postconditioning effects [14], [15]. Nonetheless, hypercholesterolemia was also reported to improve myocardial function [16]. In addition, there is evidence suggesting that hypercholesterolemia might protect against ischemia-induced arrhythmias [17].

Cholesterol direct effects on cardiomyocytes function have becoming a target for many studies. Those efforts are substantiated in the evidence that cholesterol-enriched lipid domains can concentrate, through direct interactions with lipids or in association with proteins for example caveolins, signaling molecules [18], [19], [20], [21], [22] and ion channels [23], [24]. However, the majority of experimental design attempting to elucidate cellular cholesterol content modulation direct effects on cardiomyocytes excitation, contraction and signaling pathways, is based o the use of cyclodextrins, liposomes or exposure to isolated lipoproteins. Such approach imposes important limitations, as it excludes the contribution of cell communication with other systems

like the immune system, vasculature, and endocrine system in an environment of hypercholesterolemia. Furthermore, a longitudinal potential is limited since those methodologies promote abrupt depletion/input of cell cholesterol. Therefore, experimental models of hypercholesterolemia with modification on cell cholesterol content would significantly contribute to the elucidation of hypercholesterolemia direct effects on cardiomyocytes function.

It is hypothesized that hypercholesterolemia directly affects cardiomyocytes and heart function. In our study, we assessed the effects of early-stage hypercholesterolemia on cardiomyocytes excitability, contraction, and remodeling of Ca^{2+} handling as well as in *in vivo/ex vivo* hearts using a murine model fed with a cholesterol-enriched diet. After 5 weeks, cholesterol-enriched diet promoted an increase in the total serum cholesterol levels and also increases in cellular cholesterol content. The isolated cardiomyocytes from hypercholesterolemic mice displayed altered action potential (AP) depolarization and repolarization phases, followed by increasing I_K and reducing I_{Ca} and alterations in Ca^{2+} handling. Contractile function, on the contrary, was preserved. Isolated hearts from hypercholesterolemic mice presented similar contraction properties compared to the control group during IR, although hypercholesterolemia was found to partially protect the hearts against arrhythmias. Finally, hypercholesterolemia induced little changes in the electrocardiogram (ECG), particularly a slight shortening of QT interval. Our findings will help to understand direct effects of cholesterol in the modulation of cardiac electromechanical properties and in hypercholesterolemia-related cardiovascular dysfunctions.

METHODS

1- Experimental Models

Male Swiss mice at 6-week age were fed *at libitum* with AIN-93 [25] diet, in the absence (CTR) or added with 1.25% cholesterol (CHO). AIN-93 diet was maintained for 5 consecutive weeks, from which blood samples were collected to evaluate circulating levels of total cholesterol and mice were then euthanatized for use in experiments. Experiments were performed in accordance with guidelines provided by Animal Research: Reporting *In Vivo* Experiments (ARRIVE). All surgical and

management procedures were previously approved by the Institutional Animal Care and Use Committee at Federal University of Minas Gerais (UFMG).

2- Cardiomyocytes isolation

Left ventricle cardiomyocytes were isolated according to a previously described method [26], with minor modifications. Freshly isolated cells were kept in Tyrode solution (containing, in mM: 140 NaCl, 5.4 KCl, 0.5 MgCl₂, 0.33 NaH₂PO₄, 11.0 glucose, 5.0 HEPES, and 1.8 CaCl₂, pH 7.2) at room temperature (22 - 25 °C). Experiments were conducted for at most 3 h after each cell preparation.

3- Gas Chromatography (GC)

Lipid fraction of freshly isolated left ventricle cardiomyocytes pellet extracted following folch method [27], in which a separation solution consisting of chloroform/methanol in a ratio of 2:1 (v/v) was used. Cell sample was sonicated (10 min) and lipid phase (dense) was separated from the water-soluble phase after 30 s centrifugation (2000 rpm). Lipid extracted phase was dried out and submitted to saponification reaction with 25 ml ethanolic sodium hydroxide (1 M) under heating. The unsaponifiable phase (enriched in cholesterol) was extracted with ethyl acetate and dried out overnight. The unsaponifiable matter was treated with *N,O*-Bis(trimethylsilyl)trifluoroacetamide (BSTFA) to obtain trimethyl-silyl (TMS) derivatives. The GC analyses were run using a gas chromatograph HP7820A (Agilent) equipped with a flame ionization detector at 300 °C. To access cholesterol separation from contaminants, sample was submitted to a ramp protocol starting from 250 °C at a rate of 10 °C/min for 5 min, with an injector (split 1:30) at 300 °C, using an HP5 column (Agilent; 30 m x 0.32 mm x 0.25 μm), with hydrogen was used as the carrier gas (3 ml/min). An injection volume of 3 μl was applied to the column. Cholesterol peak identification and concentration were calculated comparing peak areas with a standard curve using known concentration of cholesterol (Sigma Aldrich) analyzed under same conditions as samples. The final content of cholesterol was presented normalized by total protein concentration taken from particle free supernatant obtained before lipid extraction using bovine serum albumin as standard.

4- Patch-Clamp technique

Whole-cell patch clamp was performed using an EPC-10 patch clamp amplifier (HEKA, Holliston, Massachusetts) at room temperature (22 - 25 °C), in voltage-clamp mode for current measurements and in current-clamp mode for AP recordings [28]. Glass pipettes were set with 1-2 MΩ tip resistance. Current measurements were low-pass filtered (Bessel active filter with cutoff frequency of 2.9 kHz) and electronically compensated for series resistance (60 - 80%). After achieving the whole-cell configuration, a 2 - 3 min resting period was waited before any recording takes place, to allow proper dialysis between pipette solution and intracellular media. In addition, cell in which total series resistance reached a value equal or higher than 8 MΩ were excluded from analysis, to prevent exacerbated voltage-clamp errors. In the AP recordings, after achieving the whole-cell configuration, amplifier was immediately switched to current-clamp mode and resting membrane potential was measured before the pipette solution equilibration. Pipettes were filled with an internal solution composed by, in mM: 20 KCl; 130 K-aspartate; 130 KOH; 10 HEPES; 2 MgCl₂; 5 NaCl, pH 7.2, and bathed with Tyrode solution. AP recordings were sampled at 10 kHz. For calcium current (I_{Ca-L}) recordings, pipettes were filled with a solution composed by, in mM: CsCl 140; MgCl₂.6H₂O 1; HEPES 10; EGTA 10; Na₂ATP 5, pH 7.2, and cells were bathed in a solution containing, in mM: TEA-Cl 150; MgCl₂.6H₂O 0.5; Glucose 11; HEPES 10; CaCl₂.2H₂O 1.8. During outward potassium current (I_K) measurements, pipettes were filled with a solution containing, in mM: 140 KCl, 1 MgCl₂, 10 EGTA, 10 HEPES, 5 Glucose, pH 7.2 and cells were bathed in a solution containing, in mM: NMDG 140 KCl 5.6; MgCl₂.6H₂O 0.5; CdCl₂.H₂O 0.1; HEPES 10; Glucose 11; CaCl₂.2H₂O 1.8. Current records were sampled at 10 kHz and 5 kHz, respectively, for I_{Ca-L} and I_K. I_{Ca-L} was fitted with a Boltzmann equation in the form: $I_{(V_m)} = G_{max} * \frac{(V_m - E_i)}{1 + e^{\frac{(V_m - V_{50})}{S}}}$, where G_{max} is the maximal conductance; V_m is the tested membrane potential; E_i , is the calculated electrochemical equilibrium potential for ion i ; V_{50} is the membrane potential where 50% of the channels are activated and S is the slope factor. G/G_{MAX} and I/I_{MAX} plots were fitted using the Boltzmann equation in the form: $X/X_{MAX} = G_{max} * \frac{1}{1 + e^{\frac{(V_{50} - V_m)}{S}}}$, where X/X_{MAX} represents I/I_{MAX} or G/G_{MAX} ; V_{50} is the membrane potential to reach 50% of the maximum conductance (for G/G_{MAX}) or of the maximum current (for I/I_{MAX}) inactivated and S is the slope factor.

5- Sarcomere dynamics measurements

Sarcomere contraction was recorded using a high-speed NTSC camera (MyoCamCCD100V, IonOptix, Milton, MA, USA, 250 Hz) and analyzed based on sarcomere deconvolution through a fast Fourier transform (IonWizard, IonOptix, Milton, MA, USA). Freshly isolated left ventricle cardiomyocytes were left sit in a coverslip assembled into a chamber containing a pair of platinum electrodes. Field stimulation (MyoPacer, IonOptix, Milton, MA, USA) set with 4 ms duration and 60 V biphasic pulses were imposed to cardiomyocytes, bathed in Tyrode solution at a stimulation frequency of 1 Hz. Five consecutive events of sarcomere shortening and re-lengthening were averaged for each cell analysis. Sarcomere sizes were measured using a fast Fourier transform algorithm (IonWizard, IonOptix, Milton, MA, USA), in a relaxed state, without stimulation. All experiments were performed at room temperature (22 - 25 °C).

6- Fluorescence measurements of intracellular Ca^{2+} transients

Cardiomyocytes were loaded with 1 μ M of the dual-excitation fluorescence probe Fura2-AM (Santa Cruz, USA) at room temperature for 20 min under gentle agitation and protected from light exposure. Intracellular Ca^{2+} transients were elicited simultaneously with sarcomere contraction experiments, using the same stimulation protocol. A 340/380 nm dual excitation light source was used through a high-speed shutter (Hyper-Switch, IonOptix, Milton, MA, USA) with a fluorescent bulb and appropriate light cube filter. Fluorescence emission was detected using a photomultiplier tube (PMT), controlled and digitized by a fluorescence system interface (FSI700, IonOptix, Milton, MA, USA). The fluorescence obtained from both excitation light sources was used to calculate Ca^{2+} concentration following the equation: $[Ca^{2+}] = K_d * \frac{R-R_{min}}{R_{max}-R} * \frac{Sf2}{Sb2}$ [29], in which R_{max} and R_{min} are the ratio of fluorescence in depleted and saturated Ca^{2+} condition, obtained during *in vivo* calibration, $Sf2$ and $Sb2$ are the fluorescence arbitrary values for 380 nm excitation wavelength in depleted and saturated Ca^{2+} condition, and K_d is the Ca^{2+} -Fura-2 dissociation constant (assumed as 225 nM). *In vivo* calibration was performed according to manufacturer instructions, using 5 μ M ionomycin to modulate cell calcium concentration. Calibration was performed on each cell pool load, averaging the values from a sample of 3-5 cells, and

used to calculate Ca^{2+} concentration of cells from the same load. Five consecutive events of global calcium transient were averaged for each cell analysis.

7- Protein quantification: Western-Blot

Tissue samples were homogenized in Rippa Lysis Buffer (Millipore, USA) and centrifuged at 10,000 g for 15 min at 4 °C. The protein samples were mixed with denaturing SDS-PAGE buffer, heated at 95 °C for 3 min, fractionated in a 10% polyacrylamide gel, and transferred to a pvdf-transfer membrane. Protein bands on the membrane were stained with Ponceau to check for equal loading. The membranes were incubated with the anti-Cav1.2 primary antibodies (Santa Cruz Biotechnology, USA). The signal was detected using Luminata Western blotting detection system (Millipore, USA) followed by densitometric analyzes with the software ImageQuantTL. GAPDH was used as a control for variations in the protein loading.

8- Ischemia-Reperfusion experiments

Langendorff perfusion system was used to evaluate the effects of hypercholesterolemic diet in heart function. Mice were decapitated 10 min after i.p. injection of 400 IU heparin. Thorax was opened and the heart was rapidly excised and mounted onto the aortic cannula by the Langendorff apparatus (AD Instruments) at a constant pressure of 60 mmHg with oxygenate (95% O_2 , 5% CO_2) and warm (37 °C) Krebs-Ringer buffer (118.4 mmol/L NaCl, 4.7 mmol/L KCl, 1.2 mmol/L KH_2PO_4 , 1.2 mmol/L $\text{MgSO}_4 \cdot 7\text{H}_2\text{O}$, 2.5 mmol/L $\text{CaCl}_2 \cdot 2\text{H}_2\text{O}$, 11.7 mmol/L Glucose e 26.5 mmol/L NaHCO_3). After 30-min stabilization period, the left anterior descending coronary artery was tied to block solution flow as described [30] together with the adjacent veins, under the left auricular appendage. After 30 min, vascular occlusion was released and reperfusion took place for over 90' with Krebs-Ringer solutions. All hemodynamic parameters were measured by using an elastic water-filled balloon placed in left ventricle that was connected to a pressure transducer to record the left ventricular systolic pressure (LVSP), left ventricular end-diastolic pressure (LVEDP), rates of pressure development (dP/dt) and heart rate (HR). In order to obtain a quantitative measurement, arrhythmias were graded arbitrarily according to their duration. Therefore, the occurrence of cardiac arrhythmias for up to 5 min was assigned the factor 1, 10 min was assigned the factor 2, 15 min was assigned the factor 3, 20 min was assigned the factor 6, 25 min was assigned the factor 9, and 30 or more min was

assigned the factor 12. A value of 0-12 was thus obtained in each experiment and was denoted “arrhythmia severity index” (ASI) as previously described [31]. All data were acquired by acquisition data system PowerLab, LabChart 7 (ADInstruments, São Paulo, Brazil). Hearts were maintained in stabilization for 30 min period, 15 min of ischemia and 90 min of reperfusion.

9- Electrocardiography

We used a six-channel non-invasive electrocardiograph (ECG-PC version 2.07, Brazilian Electronic Technology - TEB, Belo Horizonte, MG, Brazil). After sedation (1.5% Isoflurane, vaporized on moisturized compressed air), electrodes were attached on mice limbs skin, and the periphery 6 derivation were simultaneously recorded for 10 min on each animal. Mean wave parameters were obtained from DII, at 50 mm/s, and 2 N, and all 6 derivations were monitored for arrhythmias prospection.

10- Statistical analysis

Data are presented as means \pm standard error (SE), unless when indicated. Statistical significance between groups was determined by the appropriate statistical test according to sample distribution, as indicated for each experiment. Significance was set at $p < 0.05$, while confidence level of significance for rejection of null hypothesis is indicated in each test ($p < 0.05$; $p < 0.01$; $p < 0.001$). Data were analyzed using GraphPad Prism 6.0.

RESULTS

1- High cholesterol-fed mice display increased serum and cellular cholesterol content

Male 8-12 week aged Swiss mice were randomly split into two groups and fed *ad libitum* with AIN-93 diet or AIN-93 added with 1.25% cholesterol. After 5 weeks of treatment, no differences were observed in mean body weight (Fig 1A), nor in the heart weight over tibia length. However, high-cholesterol diet fed mice (denoted as CHO) displayed increased total serum cholesterol levels (Fig 1C, $*p < 0.05$). Cellular cholesterol content was evaluated through gas-chromatography using freshly isolated cardiomyocytes from experimental groups. As demonstrated in Fig 1D, CHO mice had higher cellular cholesterol content ($*p < 0.001$) when compared to regular AIN-93 fed mice (denoted as CTR) In addition, mean cardiomyocyte capacitance was found increased in the high cholesterol fed experimental group. All data described above was

tested with unpaired student's T-test after D'Agostino & Pearson omnibus normality test.

2- High cholesterol-fed mice display increased rates of action potential depolarization and reduced repolarization time

To investigate the effects of a high cholesterol diet on the electrical properties of freshly isolated cardiomyocytes, we elicited left ventricle cells APs through a 1 nA amplitude and 3-5 ms duration depolarization pulses with 1 Hz frequency, and tracked membrane voltage using whole-cell patch-clamp technique in current clamp mode, leaving membrane potential unclamped (i.e. without input of constant current). Representative APs from CTR and CHO isolated cardiomyocytes are shown in Fig 2A. CHO cardiomyocytes had comparable AP amplitude and resting membrane potential to CTR (Fig 2B and Fig 2D, respectively). CHO cardiomyocytes displayed increased maximum rate of AP depolarization (Fig 1C, * $p < 0.05$). Regarding the repolarization phase, CHO isolated cardiomyocytes displayed reduced time to reach 90% of repolarization when compared to CTR (Fig 1G, * $p < 0.05$). Although there is a trend to a lower mean time to reach 10% (Fig 1E) and 50% (Fig 2F) of repolarization, such mean difference was not considered to be significant. The data described above was tested with Mann Whitney test to compare medians after a Gaussian approximation. Normality was tested with D'Agostino & Pearson omnibus test.

3- Characterization of macroscopic K^+ currents in high cholesterol-fed mice

Evaluation of AP waveform demonstrated modulation of repolarization in CHO isolated cardiomyocytes. In order to evaluate macroscopic K^+ currents, isolated cardiomyocytes were stimulated through a series of voltage steps (4 s long, every 15 s) ranging from -60 mV to +60 mV, from a holding potential of -70 mV. Representative traces of K^+ currents are shown in Fig 3A. Peak outward current was normalized by cell capacitance and plotted against membrane voltage (Fig 3B). CHO cardiomyocytes displayed an increased current density when compared to CTR ($p < 0.001$). Peak current at each potential was normalized by the maximum current at +60 mV and plotted against membrane voltage (Fig 3C), in order to evaluate the fractional current to be activated depending on membrane voltage, as a means to reflect the stationary voltage-dependent activation of K^+ channels. As demonstrated, $V_{1/2}$, the voltage at which half of maximum current is achieved, is comparable between CHO and CTR cardiomyocytes.

To evaluate individual contributions of outward K^+ currents, +50 mV stimulation pulse was fitted with an exponential function (refer to methods) and the peak contributions (I_{to} , I_{kur} and I_{ss}) were discriminated based on the time constants for current inactivation. One K^+ current identity that cannot be properly appreciated in the stimulation protocol described above is the inward rectifying K^+ current (I_{K1}), due to inward rectification. An adapted protocol was used, with a series of voltage steps (3 s long, every 15 s) ranging from -140 mV to -60 mV, from a holding potential of -70 mV. Representative traces are presented in Fig 3E. Peak I_{K1} current was normalized by cell capacitance and plotted against membrane voltage (Fig 3B). CHO cardiomyocytes displayed an increased current density when compared to CTR ($p < 0.001$). Fig 3B and Fig 3F were tested with 2-way ANOVA followed by Bonferroni post hoc test. Fig 3C was fitted with a Boltzmann equation and calculated $V_{1/2}$ was tested with unpaired students T-test. Fig 3D was tested with unpaired students T-test. Normality was tested with D'Agostino & Pearson omnibus test.

4- Characterization of L-Type Ca^{2+} currents in high cholesterol-fed mice

Other component highly involved in the progression of AP repolarization in ventricular myocytes is the L-type Ca^{2+} current, as it imposes a resistance to the repolarization. In order to evaluate the L-type Ca^{2+} current, isolated cardiomyocytes were stimulated with a series of voltage steps (500 ms long, every 10 s) ranging from -80 mV to +50mV, from a holding potential of -80 mV. Representative traces of Ca^{2+} currents are shown in Fig 4A. Peak current was normalized by cell capacitance and plotted against membrane voltage (Fig 4B). CHO cardiomyocytes displayed reduced Ca^{2+} current density when compared to CTR ($p < 0.001$). Conductance (G) at each potential was normalized by maximum conductance (G_{MAX}) obtained after fitting the I-V plot from Fig 4B with a Boltzmann equation. G/G_{MAX} plot represents the stationary voltage-dependent activation of Ca^{2+} channels (Fig 4C), in which CHO and CTR cardiomyocytes behave similarly, as indicated by the comparable V_{50} for G/G_{MAX} , the voltage at which half of maximum conductance is achieved (Fig 4E). A second protocol was applied to evaluate the voltage-dependent inactivation of L-type Ca^{2+} current (Fig 4D, H_{∞}). In these experiments, a 0 mV 300 ms testing pulse was applied after each voltage step described before. Peak current of testing pulse after each voltage step was normalized by maximum current that occurs at -80 mV conditioning pulse (from the voltage step protocol) and plotted against membrane voltage from conditioning pulse. CHO and

CTR cardiomyocytes have comparable stationary voltage-dependent inactivation, as indicated by the V_{50} for H_{∞} (Fig 4F). Finally, expression of Cav1.2 is reduced in CHO left ventricle compared to CTR mice left ventricle (Fig 4G) arguing in favor of the reduced current density in isolated cardiomyocytes. Fig 4B was tested with 2-way ANOVA followed by Bonferroni post hoc test. Fig 4C and Fig 4D were fitted with a Boltzmann equation and calculated V_{50} in Fig 4E and Fig 4F were tested with unpaired students T-test. Fig 4G was tested with Mann Whitney test. Normality was tested with D'Agostino & Pearson omnibus test.

5- Ca^{2+} handling properties in high cholesterol-fed mice

Changes in L-type Ca^{2+} current might trigger alterations in cardiomyocytes Ca^{2+} handling as a consequence of the intrinsic association between Ca^{2+} -induced RyR activation with further Ca^{2+} release from SR stores [32], [33], [34]. Global Ca^{2+} transients were elicited through field stimulation (at 1 Hz, 4 ms duration and 60 V bi-phasic pulses) in cardiomyocytes loaded with Fura2-AM probe. Representative Ca^{2+} transients are presented in Fig 5A. Ca^{2+} concentration during peak transient and after full cell relaxation is plotted in Fig 5B and Fig 5C, respectively. CHO cardiomyocytes have lower diastolic Ca^{2+} concentration when compared to CTR (* $p < 0.01$), while peak transient reached similar Ca^{2+} concentrations. When cardiomyocytes were stimulated with the beta-agonist isoproterenol, both diastolic and peak transient Ca^{2+} concentration was increased (* $p < 0.05$ and # $p < 0.001$). In addition, diastolic Ca^{2+} concentration in CHO cardiomyocytes stimulated with isoproterenol was lower compared to isoproterenol-stimulated CTR cells (& $p < 0.05$). The time required to reach peak transient concentration was also evaluated (Fig 5D). CHO cardiomyocytes displayed reduced time to reach peak transient compared to CTR (* $p < 0.05$) and isoproterenol stimulation had no effects on this variable, compared to the respective non-stimulated groups. The decay of Ca^{2+} transients was comparable between CHO and CTR cardiomyocytes, demonstrated by the similar time constant for fluorescence decay (Fig 5E). Exposure to isoproterenol increased the transient decay speed, as evidenced by reduced time constant compared to non-stimulated groups. However, both isoproterenol-stimulated CHO and CTR cells had comparable time constants for Ca^{2+} transient decay. Statistics were performed using Kruskal-Wallis test for Gaussian approximation followed by Dunn's multiple comparison post hoc test. Normality was tested with D'Agostino & Pearson omnibus test.

6- Evaluation of cardiomyocytes' contractile properties of high cholesterol-fed mice

Considering the central role of Ca^{2+} to the proper functioning of the contractile machinery, changes in Ca^{2+} handling might implicate in alterations of cardiomyocytes' contractile properties. We assessed cardiomyocytes contraction through field stimulations (at 1Hz, 4 ms duration and 60 V biphasic pulses) and analyzed sarcomere and cell edges shortening and re-lengthening as a measure of cardiomyocytes contractile function. Fig 6A presents representative traces of CHO and CTR cardiomyocytes contraction, in the absence or presence of isoproterenol stimulation. Sarcomere length during diastole had comparable values in all experimental groups, as demonstrated in Fig 6B. CHO and CTR cells had similar fractional shortening in both non-stimulated and isoproterenol-stimulated groups. However, isoproterenol induced an increase in cell fractional shortening (* $p < 0.001$; # $p < 0.001$). CHO and CTR had similar kinetics for cardiomyocytes' contraction (Fig 6D, Fig 6E) and relaxation (Fig 6F). Isoproterenol promoted a reduction in the time to reach 50% of peak contraction (Fig 6D) in both groups compared to their respective non-stimulated controls (* $p < 0.05$; # $p < 0.001$), but no effect could be observed at 90% of peak contraction. Relaxation speed is also accelerated after isoproterenol administration in both CHO and CTR (* $p < 0.001$; # $p < 0.001$). Statistics were performed using Kruskal-Wallis test for Gaussian approximation followed by Dunn's multiple comparison post hoc test. Normality was tested with D'Agostino & Pearson omnibus test. Overall, the contractile properties of cardiomyocytes are preserved in high cholesterol-fed mice.

7- Evaluation heart electro-mechanical function after Ischemia-Reperfusion in high cholesterol-fed mice

Hypercholesterolaemia imposes a principal risk factor for coronary artery disease (CAD) [3], which could lead to an elevated risk of ischemic events in patients with high end levels of cholesterol, regardless of their genotype [35]. A protocol of 30 min ischemia was induced through occlusion of coronary artery in CHO and CTR isolated hearts mounted in a Langendorff system. CHO and CTR hearts demonstrated similar contractile function, exemplified by the maximum (Fig 7A) rate of pressure (dP/dt), the developed pressure (difference between LVSP and EDP) (Fig 7B) and end diastolic pressure (EDP) (Fig 7C) pressure and intrinsic heart rate (Fig 7D). After 30 min ischemia, CHO and CTR hearts displayed a similar reduction in all parameters described above, without differing among themselves. During reperfusion, CHO heart

tended to recover a little better than CTR hearts in regarding maximum dP/dt, developed pressure and minimum pressure, however, such difference was not considered to be significant from CTR hearts. Overall CHO hearts have slightly better or at least preserved mechanical function compared to CTR hearts. Arrhythmic contractions were quantified and ascribed in an arrhythmic score, as described before [31]. CHO hearts displayed reduced arrhythmogenic profile after reperfusion compared to CTR hearts (*p<0.05). Figs 7A-D were tested with Two-way ANOVA followed by Bonferroni post hoc test. Fig 7E was tested with unpaired students T-test. Normality was tested with D'Agostino & Pearson omnibus test.

8- Evaluation of electrocardiographic profile in the hearts of high cholesterol-fed mice

As described above, modulation of cardiomyocytes' Ca²⁺ handling as well as electrical properties was associated with a reduced arrhythmogenic profile in *ex vivo* experiments. ECG was performed in anesthetized mice in order to investigate the effects of high cholesterol diet on conduction/propagation of electrical stimuli *in vivo*. Fig 8A display representative traces from CTR and CHO mice. Overall, both groups have a similar electrocardiographic profile, with comparable duration of P wave (Fig 8B), PR interval (Fig 8C), QRS interval (Fig 8D) and heart rate (Fig 8F). CHO hearts have a slight shorter QT interval (Fig 8E) when compared to CTR hearts. No arrhythmias were detected in any of the experimental groups. All data were tested with unpaired students T-test. Normality was tested with D'Agostino & Pearson omnibus test.

DISCUSSION

The present study was the first to investigate the effects of early hypercholesterolemic diet on the electro-contractile properties of cardiomyocytes and *in vivo/ex vivo* hearts from Swiss mice. Our results showed that after 5 weeks, Swiss mice fed *ad libitum* with the balanced AIN-93 diet added with 1.25% free cholesterol had increased serum total cholesterol levels that were accompanied by increased cellular cholesterol content. Such dyslipidemic profile was associated with modulation of cardiomyocytes electrical properties, notably by increasing I_K and reducing I_{Ca}, which reflected in the waveform of the AP. In addition, cardiomyocytes isolated from hypercholesterolemic mice displayed alterations in Ca²⁺ handling, although contractile function was preserved. Isolated hearts from hypercholesterolemic mice behave similarly to the control ones during IR, although hearts from hypercholesterolemic mice were less prone to develop arrhythmias

during reperfusion. ECG readings were similar, apart from a slight shortening of QT interval on hypercholesterolemic mice. Understanding the role of cholesterol in the modulation of cardiac electro-mechanical properties is very useful for the complete elucidation of hypercholesterolemia-related cardiovascular dysfunctions.

1- Cholesterol modulation of myocytes electro-mechanical properties

Cholesterol and sphingolipids enriched domains in the plasma membrane are well recognized as lipid rafts [36]. Besides specific lipids, rafts also concentrate several signaling proteins, playing a key role in signaling transduction [37], [24]. Those proteins can be either trapped in the lipid milieu or bound to associated proteins like caveolin [24], which can bring downstream effectors in close proximity with signaling molecules [38], [39], [40]. Among several proteins found to be concentrated in caveolae/raft domains, modulation of endothelial nitric oxide synthase (eNOS) [18], [19], adenilate cyclase [20], PI3K/Akt axis [22], and beta-adrenergic receptors [41] are described, all of which having important roles in cardiomyocyte' electro-mechanical properties. Particularly, several ion channels were found to be selectively target to caveolae/raft domains in the heart, including Nav1.5 [42]; Cav1.2 [43], [44], [45]; HCN4 [46], [47]; Kir6.1 [48], [49] and Kv4.2 as well as the regulatory subunit KChIP2 [50].

In our results, an increase in peak outward K^+ as well as in inward rectifier K^+ (I_{K1}) currents was observed in cardiomyocytes isolated from hypercholesterolemic mice. These findings line up with the evidence of migration of Kv4.2 and KChIP2 towards high density cell fraction with subsequent reduction of outward K^+ current [50]. I_{K1} increase could be assigned to increased K^+ reversal potential as a consequence of K^+ accumulation in T-tubule structure, as already described [51], especially taking in account the observed increase in outward K^+ currents in our model. In addition, we observed reduction in Cav1.2 protein levels and in I_{Ca} current density without modulation of stationary voltage-dependence for activation and inactivation of LCC. Previous evidences have demonstrated that targeting LCC to caveolae was essential for appropriate Ca^{2+} -induced Ca^{2+} release (CICR), and disruption of caveolae with methyl- β -cyclodextrin (B-CD) interferes with CICR without changing I_{Ca} current density and gating properties [52].

The sum of contributions provided by increased I_K and decreased I_{Ca} reflected in a shorter AP repolarization time in CHO cardiomyocytes compared to CTR ones. The

maximum rate of depolarization was increased in CHO ventricular cardiomyocytes. Because Nav1.5 is the primary determinant to AP upstroke phase in ventricular myocytes, this evidence points toward a possible modulation of Na⁺ current in the hypercholesterolemic mice. Indeed other studies have demonstrated targeting of Nav1.5 to caveolae, and that is important for beta-adrenergic modulation of Na⁺ current [42], [45]. Cholesterol was shown to be important to t-tubule structuration, and treatment with B-CD promoted reduced normalized cell capacitance over area, as well as disturbances in Ca²⁺ handling [51], [53]. Cardiomyocytes isolated from our hypercholesterolemic mice that have increased cell cholesterol content displayed increased cell capacitance, which might suggest a higher degree structuration of t-tubule. Strengthening this rationale, despite reduced I_{Ca}, Ca²⁺ transients were found to be comparable to control cardiomyocytes, while time to reach peak Ca²⁺ concentration during intracellular transients pointing to a more synchronic Ca-induced Ca²⁺ release. As previously demonstrated, dyssynchrony of SR Ca²⁺ release contribute to the slowing of SR Ca²⁺ release in congestive heart failure and catecholaminergic polymorphic ventricular tachycardia [54]. In addition, the lower diastolic Ca²⁺ concentration would further prevent SR leakage through Ca²⁺ quarks and Ca²⁺ sub-sparks events [55], rendering a higher fraction of RyR to a more likely synchronic Ca²⁺ release through sparks during an AP. Apart from Ca²⁺ handling, beta-adrenergic signaling is preserved in cardiomyocytes from CHO mice, as evidenced by increase in both diastolic and systolic Ca²⁺ concentration as also in Ca²⁺ transient decay time constant (and therefore SERCA activity). Contrary to our findings, in cholesterol depletion models, beta-adrenergic function is impaired in cardiomyocytes [41] evidence that is supported since several components of beta-adrenergic pathway, including PKA, beta-adrenergic receptors and adenylyl cyclase can be targeted to caveolae [20], [21]. Moreover, in a rabbit model, feeding 0.5% cholesterol suppressed SERCA-2 mRNA levels, associated with enrichment of cholesterol content in PM [56]. In cultured rat neonatal cardiomyocytes, increased PM cholesterol levels through liposomes promoted an increase in intracellular Ca²⁺ concentration, while cholesterol depletion resulted in an increase in intracellular Ca²⁺ concentration [57]. Regarding contractile function, it was demonstrated that depletion of cholesterol by B-CD increases the rate of cell contraction and generates defects in cell relaxation in rat's neonatal cardiomyocytes. Moreover, membrane tension, Ca²⁺ spikes frequency and intracellular Ca²⁺ concentration was found increased under B-CD treatment [58]. In our model, increased concentration of

cell cholesterol content revealed opposite effects, characterized by preserved contractile function, with comparable cell fractional shortening, contraction and relaxation kinetics, as well as preserved beta-adrenergic response. Besides, intracellular Ca^{2+} concentrations was found decreased in CHO cardiomyocytes, as discussed above.

The literature on the effects of cholesterol modulation of cardiomyocytes electromechanical properties as well as in Ca^{2+} handling is still vague and scarce. Most of these studies are conducted through manipulation of PM cholesterol using B-CD saturated or not with cholesterol [53], [41], [43] [59], [58], [60], with abrupt removal and restoration of cholesterol from PM. Use of B-CDs, however, imposes some limitations, since B-CDs may remove cholesterol from both raft and non-raft domains; may alter cholesterol distribution between different cellular membranes. In addition, other hydrophobic molecules such as phospholipids and proteins may also be extracted [61]. Other studies investigated the role of lipoproteins in modulating properties of cardiomyocytes [62], [63], providing a more physiological approach. However, cell exposure to isolated lipoprotein might not provide a reliable estimation of their contribution in an environment of several lipoprotein interactions, as well as the longitudinal experimental design limitation that prevents signaling remodeling dependent of gene expression in freshly isolated primary cells. Our results are evaluated based on a model of hypercholesterolemia with modulation of PM cholesterol content that allows investigation of cholesterol modulation of cardiomyocytes properties in freshly isolated cells with high reliability. That information might contribute to the complete elucidation of cholesterol involvement with heart remodeling during CVDs progression. .

2- Hypercholesterolemia-related role in cardiovascular disease (CVD) and heart function

Hypercholesterolemia is more deeply investigated in the context of CVDs. The relationship between hypercholesterolemia and cardiovascular diseases has long been recognized [2], [3], and hypercholesterolemia, particularly when associated to high LDL cholesterol content, is a major risk factor for the development of atherosclerosis and further ischemic heart disease [64]. Apart from proatherogenic effects on the vascular system, direct effects of hypercholesterolemia in heart mechanical and electrical function, on the other hand, is less understood. Most of evidence agree that hypercholesterolemia aggravates IR injury [12], [13] and abrogates preconditioning and

postconditioning attenuation of IR injury [14], [15], [65]. Besides, hypercholesterolemia-driven heart contractile dysfunction has also been reported [66]. On the other hand, hypercholesterolemia could be protective against ventricular arrhythmias during ischemia [17], [67]. The literature on this subject is still controversial, and other studies reported no additional harm after reperfusion [68] or even a cardioprotective improvement in myocardial function [16] in hypercholesterolemic hearts.

From our results, early stage hypercholesterolemia after 5 weeks of treatment does not impair contractile function in isolated hearts, nor aggravates IR dependent heart dysfunction, as demonstrated by comparable developed pressure, maximum rate of pressure development and end diastolic pressure. In addition, no changes in intrinsic heart frequency were observed. However, stage hypercholesterolemic hearts were less prone to arrhythmias after IR injury, in accordance with previous studies. In anesthetized mice, ECG profile was also similar between control and stage hypercholesterolemic mice, although QT interval was found reduced in stage hypercholesterolemic ones. Reduction in QT interval could be attributed to the observed shortening of AP, as consequence of simultaneous increase in I_K together with decrease in I_{Ca} .

Overall our results demonstrate that early hypercholesterolemia-driven increase in cellular cholesterol content is associated with direct modulation of cardiomyocytes excitability and Ca^{2+} handling, while contractile function is preserved. Heart dysfunction during IR was not modulated by hypercholesterolemia, although hypercholesterolemic hearts were more protected against arrhythmias. These results will contribute to the elucidation of the direct effects of hypercholesterolemia and cell cholesterol content on the progression of CVD.

REFERENCES

- [1] P. Durrington, Dyslipidaemia, *Lancet*. 362 (2003) 717–31. doi:10.1016/S0140-6736(03)14234-1.
- [2] R.B. Shekelle, A.M. Shryock, O. Paul, M. Lepper, J. Stamler, S. Liu, W.J.J. Raynor, Diet, serum cholesterol, and death from coronary heart disease. The Western Electric study, *N Engl J Med*. 304 (1981) 65–70. doi:10.1056/NEJM198101083040201.

- [3] V. Tiwari, M. Khokhar, Mechanism of action of anti-hypercholesterolemia drugs and their resistance, *Eur J Pharmacol.* 741 (2014) 156–170. doi:10.1016/j.ejphar.2014.07.048.
- [4] W.M. Verschuren, D.R. Jacobs, B.P. Bloemberg, D. Kromhout, A. Menotti, C. Aravanis, H. Blackburn, R. Buzina, A.S. Dontas, F. F, Serum total cholesterol and long-term coronary heart disease mortality in different cultures. Twenty-five-year follow-up of the seven countries study, *JAMA.* 274 (1995) 131–136.
- [5] H. Tolonen, U. Keil, M. Ferrario, A. Evans, W.M. Project, Prevalence, awareness and treatment of hypercholesterolaemia in 32 populations: results from the WHO MONICA Project, *Int J Epidemiol.* 34 (2005) 181–192. doi:10.1093/ije/dyh298.
- [6] M.J. McQueen, S. Hawken, X. Wang, S. Ounpuu, A. Sniderman, J. Probstfield, K. Steyn, J.E. Sanderson, M. Hasani, E. Volkova, K. Kazmi, S. Yusuf, Lipids, lipoproteins, and apolipoproteins as risk markers of myocardial infarction in 52 countries (the INTERHEART study): a case-control study, *Lancet.* 372 (2008) 224–233. doi:10.1016/S0140-6736(08)61076-4.
- [7] F. Farzadfar, M.M. Finucane, G. Danaei, P.M. Pelizzari, M.J. Cowan, C.J. Paciorek, G.M. Singh, J.K. Lin, G.A. Stevens, L.M. Riley, M. Ezzati, National, regional, and global trends in serum total cholesterol since 1980: systematic analysis of health examination surveys and epidemiological studies with 321 country-years and 3.0 million participants, *Lancet.* 377 (2011) 578–586. doi:10.1016/S0140-6736(10)62038-7.
- [8] S. Karr, Epidemiology and management of hyperlipidemia, *Am J Manag Care.* 23 (2017) S139–S148.
- [9] C.T.T. (CTT) Collaboration, C. Baigent, L. Blackwell, J. Emberson, L.E. Holland, C. Reith, N. Bhala, R. Peto, E.H. Barnes, A. Keech, J. Simes, R. Collins, Efficacy and safety of more intensive lowering of LDL cholesterol: a meta-analysis of data from 170,000 participants in 26 randomised trials, *Lancet.* 376 (2010) 1670–1681. doi:10.1016/S0140-6736(10)61350-5.
- [10] G.H. Tomkin, D. Owens, LDL as a cause of atherosclerosis, *Open Atheroscler Thromb J.* 5 (2012) 13–21. doi:10.2174/1876506801205010013.
- [11] D. Writing Group Members, Mozaffarian, E.J. Benjamin, A.S. Go, D.K. Arnett, M.J. Blaha, M. Cushman, S.R. Das, S. de Ferranti, J.P. Després, H.J. Fullerton, V.J. Howard, M.D. Huffman, C.R. Isasi, M.C. Jiménez, S.E. Judd, B.M. Kissela, J.H. Lichtman, L.D. Lisabeth, S. Liu, R.H. Mackey, D.J. Magid, D.K. McGuire,

- E.R. 3rd Mohler, C.S. Moy, P. Muntner, M.E. Mussolino, K. Nasir, R.W. Neumar, G. Nichol, L. Palaniappan, D.K. Pandey, M.J. Reeves, C.J. Rodriguez, W. Rosamond, P.D. Sorlie, J. Stein, A. Towfighi, T.N. Turan, S.S. Virani, D. Woo, R.W. Yeh, M.B. Turner, A.H.A.S.C.S.S. Subcommittee., Heart Disease and Stroke Statistics-2016 Update: A Report From the American Heart Association, *Circulation*. 133 (2016) e38-360.
doi:10.1161/CIR.0000000000000350.
- [12] R.M. Osipov, C. Bianchi, J. Feng, R.T. Clements, Y. Liu, M.P. Robich, H.P. Glazer, N.R. Sodha, F.W. Sellke, Effect of hypercholesterolemia on myocardial necrosis and apoptosis in the setting of ischemia-reperfusion, *Circulation*. 120 (2009) S22–S30. doi:10.1161/CIRCULATIONAHA.108.842724.
- [13] N. Wu, X. Zhang, P. Jia, D. Jia, Hypercholesterolemia aggravates myocardial ischemia reperfusion injury via activating endoplasmic reticulum stress-mediated apoptosis, *Exp Mol Pathol*. 99 (2015) 449–454.
doi:10.1016/j.yexmp.2015.08.010.
- [14] P. Ferdinandy, Z. Szilvássy, L. Horváth, T. Csont, C. Csonka, E. Nagy, R. Szentgyörgyi, I. Nagy, M. Koltai, L. Dux, Loss of pacing-induced preconditioning in rat hearts: role of nitric oxide and cholesterol-enriched diet, *J Mol Cell Cardiol*. 29 (1997) 3321–3333. doi:10.1006/jmcc.1997.0557.
- [15] I. Ungi, T. Ungi, Z. Ruzsa, E. Nagy, Z. Zimmermann, T. Csont, P. Ferdinandy, Hypercholesterolemia attenuates the anti-ischemic effect of preconditioning during coronary angioplasty, *Chest*. 128 (2005) 1623–1628.
doi:10.1378/chest.128.3.1623.
- [16] T. Thim, J.F. Bentzon, S.B. Kristiansen, U. Simonsen, H.L. Andersen, K. Wassermann, E. Falk, Size of myocardial infarction induced by ischaemia/reperfusion is unaltered in rats with metabolic syndrome, *Clin Sci*. 110 (2006) 665–671. doi:10.1042/CS20050326.
- [17] A. Baartscheer, C.A. Schumacher, V. Wekker, A.O. Verkerk, M.W. Veldkamp, R.J. van Oort, I. Elzenaar, R. Ottenhoff, C. van Roomen, H. Aerts, R. Coronel, Dyscholesterolemia Protects Against Ischemia-Induced Ventricular Arrhythmias, *Circ Arrhythm Electrophysiol*. 8 (2015) 1481–1490.
doi:10.1161/CIRCEP.115.002751.
- [18] G. García-Cardena, R. Fan, D.F. Stern, J. Liu, W.C. Sessa, Endothelial Nitric Oxide Synthase Is Regulated by Tyrosine Phosphorylation and Interacts with

- Caveolin-1, *J Biol Chem.* 271 (1996) 27237–27241.
- [19] V.J. Venema, H. Ju, R. Zou, R.C. Venema, Interaction of neuronal nitric-oxide synthase with caveolin-3 in skeletal muscle. Identification of a novel caveolin scaffolding/inhibitory domain, *J Biol Chem.* 272 (1997) 28187–28190.
- [20] Y. Toya, C. Schwencke, J. Couet, M.P. Lisanti, Y. Ishikawa, Inhibition of adenylyl cyclase by caveolin peptides, *Endocrinology.* 139 (1998) 2025–2031. doi:10.1210/endo.139.4.5957.
- [21] B. Razani, M.P. Lisanti, Two distinct caveolin-1 domains mediate the functional interaction of caveolin-1 with protein kinase A., *Am J Physiol Cell Physiol.* 281 (2001) C1241-50. doi:10.1152/ajpcell.2001.281.4.C1241.
- [22] L. Zhuang, J. Lin, M.L. Lu, K.R. Solomon, M.R. Freeman, Cholesterol-rich lipid rafts mediate akt-regulated survival in prostate cancer cells, *Cancer Res.* 62 (2002) 2227–31.
- [23] R.C. Balijepalli, T.J. Kamp, Caveolae, ion channels and cardiac arrhythmias, *Prog. Biophys. Mol. Biol.* 98 (2009) 149–160. doi:10.1016/j.pbiomolbio.2009.01.012.
- [24] C. Dart, Lipid microdomains and the regulation of ion channel function, *J Physiol.* 588 (2010) 3169–3178. doi:10.1113/jphysiol.2010.191585.
- [25] P.G. Reeves, F.H. Nielsen, G.J. Fahey, AIN-93 purified diets for laboratory rodents: final report of the American Institute of Nutrition ad hoc writing committee on the reformulation of the AIN-76A rodent diet, *J Nutr.* 123 (1993) 1939–1951.
- [26] T. Shioya, A simple technique for isolating healthy heart cells from mouse models, *J Physiol Sci.* 57 (2007) 327–335. doi:10.2170/physiolsci.RP010107.
- [27] J. FOLCH, M. LEES, G.H. SLOANE STANLEY, A simple method for the isolation and purification of total lipides, *J Biol Chem.* 226 (1957) 497–509.
- [28] O. Hamill, A. Marty, E. Neher, B. Sakmann, F. Sigworth, Improved patch-clamp techniques for high-resolution current recording from cells and cell-free membrane patches, *Pflugers Arch.* 391 (1981) 85–100.
- [29] G. Grynkiewicz, M. Poenie, R.Y. Tsien, A new generation of Ca²⁺ indicators with greatly improved fluorescence properties, *J Biol Chem.* 260 (1985) 3440–3450. doi:3838314.
- [30] W.F. Lubbe, P.S. Daries, L.H. Opie, Ventricular arrhythmias associated with coronary artery occlusion and reperfusion in the isolated perfused rat heart: a

- model for assessment of antifibrillatory action of antiarrhythmic agents, *Cardiovasc Res.* 12 (1978) 212–220.
- [31] L.A. Neves, A.P. Almeida, M.C. Khosla, M.J. Campagnole-Santos, R.A. Santos, Effect of angiotensin-(1-7) on reperfusion arrhythmias in isolated rat hearts, *Braz J Med Biol Res.* 30 (1997) 801–809.
- [32] D. Bers, Cardiac excitation–contraction coupling, *Nature.* 415 (2002) 198–205.
- [33] D.M. Bers, T.A.O. Guo, Calcium Signaling in Cardiac Ventricular Myocytes, 98 (2005) 86–98. doi:10.1196/annals.1341.008.
- [34] D.M. Bers, Calcium cycling and signaling in cardiac myocytes, *Annu Rev Physiol.* 70 (2008) 23–49. doi:10.1146/annurev.physiol.70.113006.100455.
- [35] A.D. Sniderman, S. Tsimikas, S. Fazio, The severe hypercholesterolemia phenotype: clinical diagnosis, management, and emerging therapies, *J Am Coll Cardiol.* 63 (2014) 1935–47. doi:10.1016/j.jacc.2014.01.060.
- [36] L.J. Pike, Lipid rafts: bringing order to chaos, *J Lipid Res.* 44 (2003) 655–667. doi:10.1194/jlr.R200021-JLR200.
- [37] V. Michel, M. Bakovic, Lipid rafts in health and disease, *Biol Cell.* 99 (2007) 129–140. doi:10.1042/BC20060051.
- [38] A.W. Cohen, R. Hnasko, W. Schubert, M.P. Lisanti, Role of caveolae and caveolins in health and disease, *Physiol Rev.* 84 (2004) 1341–1379. doi:10.1152/physrev.00046.2003.
- [39] P.A. Insel, H.H. Patel, Do studies in caveolin-knockouts teach us about physiology and pharmacology or instead, the ways mice compensate for “lost proteins”?, *Br J Pharmacol.* 150 (2007) 251–254. doi:10.1038/sj.bjp.0706981.
- [40] D. Lingwood, K. Simons, Lipid rafts as a membrane-organizing principle, *Science* (80-.). 327 (2010) 46–50. doi:10.1126/science.1174621.
- [41] Y.G. Odnoshivkina, V.I. Sytchev, A.M. Petrov, Cholesterol regulates contractility and inotropic response to β 2-adrenoceptor agonist in the mouse atria: Involvement of Gi-protein–Akt–NO-pathway, *J Mol Cell Cardiol.* 107 (2017) 27–40. doi:10.1016/j.yjmcc.2016.05.001.
- [42] T.L. Yarbrough, T. Lu, H. Lee, E.F. Shibata, Localization of cardiac sodium channels in caveolin-rich membrane domains: regulation of sodium current amplitude, *Circ Res.* 90 (2002) 443–449. doi:10.1161/hh0402.105177.
- [43] S. Calaghan, E. White, Caveolae modulate excitation-contraction coupling and beta2-adrenergic signalling in adult rat ventricular myocytes, *Cardiovasc Res.* 69

- (2006) 816–824. doi:10.1016/j.cardiores.2005.10.006.
- [44] R.C. Balijepalli, J.D. Foell, D.D. Hall, J.W. Hell, T.J. Kamp, Localization of cardiac L-type Ca(2+) channels to a caveolar macromolecular signaling complex is required for beta(2)-adrenergic regulation, *Proc Natl Acad Sci U S A.* 103 (2006) 7500–7505.
- [45] E.F. Shibata, T.L.Y. Brown, Z.W. Washburn, J. Bai, T.J. Revak, C.A. Butters, Autonomic regulation of voltage-gated cardiac ion channels, *J Cardiovasc Electrophysiol.* 17 (2006) 34–42. doi:10.1111/j.1540-8167.2006.00387.x.
- [46] A. Barbuti, B. Gravante, M. Riolfo, R. Milanese, B. Terragni, D. Difrancesco, Localization of pacemaker channels in lipid rafts regulates channel kinetics, *Circ Res.* 94 (2004) 1325–31. doi:10.1161/01.RES.0000127621.54132.AE.
- [47] A. Barbuti, B. Terragni, C. Brioschi, D. Difrancesco, Localization of f-channels to caveolae mediates specific beta2-adrenergic receptor modulation of rate in sinoatrial myocytes, *J Mol Cell Cardiol.* 42 (2007) 71–78. doi:10.1016/j.yjmcc.2006.09.018.
- [48] V. Garg, J. Jiao, K. Hu, Regulation of ATP-sensitive K+ channels by caveolin-enriched microdomains in cardiac myocytes, *Cardiovasc Res.* 82 (2009) 51–58. doi:10.1093/cvr/cvp039.
- [49] V. Garg, W. Sun, K. Hu, Caveolin-3 negatively regulates recombinant cardiac K(ATP) channels, *Biochem Biophys Res Commun.* 385 (2009) 472–477. doi:10.1016/j.bbrc.2009.05.100.
- [50] E. Rudakova, M. Wagner, M. Frank, T. Volk, Localization of Kv4.2 and KChIP2 in lipid rafts and modulation of outward K+ currents by membrane cholesterol content in rat left ventricular myocytes, *Pflugers Arch.* 467 (2015) 299–309. doi:10.1007/s00424-014-1521-3.
- [51] A. Nikouee, K. Uchida, I. Moench, A.N. Lopatin, Cholesterol Protects Against Acute Stress-Induced T-Tubule Remodeling in Mouse Ventricular Myocytes, *Front Physiol.* 9 (2018) 1516. doi:10.1016/j.bpj.2017.11.3348.
- [52] M. Löhn, M. Fürstenau, V. Sagach, M. Elger, W. Schulze, F.C. Luft, H. Haller, M. Gollasch, Ignition of calcium sparks in arterial and cardiac muscle through caveolae, *Circ Res.* 87 (2000) 1034–1039.
- [53] Y. Zhu, C. Zhang, B. Chen, R. Chen, A. Guo, J. Hong, L.S. Song, Cholesterol is required for maintaining T-tubule integrity and intercellular connections at intercalated discs in cardiomyocytes, *J Mol Cell Cardiol.* 97 (2016) 204–212.

doi:10.1016/j.yjmcc.2016.05.013.

- [54] W.E. Louch, H.K. Mørk, J. Sexton, T.A. Strømme, P. Laake, I. Sjaastad, O.M. Sejersted, T-tubule disorganization and reduced synchrony of Ca²⁺ release in murine cardiomyocytes following myocardial infarction, *J Physiol.* 574 (2006) 519–533. doi:10.1113/jphysiol.2006.107227.
- [55] A.P. Wescott, M.S. Jafri, W.J. Lederer, G.S. Williams, Excitation-Contraction Coupling I, *J Mol Cell Cardiol.* 92 (2016) 82–92. doi:10.1016/j.yjmcc.2016.01.024.
- [56] Y. Huang, K.E. Walker, F. Hanley, J. Narula, S.R. Houser, T.N. Tulenko, Cardiac systolic and diastolic dysfunction after a cholesterol-rich diet, *Circulation.* 109 (2004) 97–102. doi:10.1161/01.CIR.0000109213.10461.F6.
- [57] E.M. Bastiaanse, D.E. Atsma, M.M. Kuijpers, A. Van der Laarse, The effect of sarcolemmal cholesterol content on intracellular calcium ion concentration in cultured cardiomyocytes, *Arch Biochem Biophys.* 313 (1994) 58–63.
- [58] B. Hissa, P.W. Oakes, B. Pontes, G.R. Juan, M.L. Gardel, Cholesterol depletion impairs contractile machinery in neonatal rat cardiomyocytes, *Sci Rep.* 7 (2017) 43764. doi:10.1038/srep43764.
- [59] A.J. Carozzi, E. Ikonen, M.R. Lindsay, R.G. Parton, Role of cholesterol in developing T-tubules: analogous mechanisms for T-tubule and caveolae biogenesis, *Traffic.* 1 (2000) 326–341.
- [60] M.Z. Haque, V.J. McIntosh, A.B.A. Samra, M. Mohammad, R.D. Lasley, Cholesterol Depletion Alters Cardiomyocyte Subcellular Signaling and Increases Contractility, *PLoS One.* 11 (2016) e0154151. doi:10.1371/journal.pone.0154151.
- [61] R. Zidovetzki, I. Levitan, Use of cyclodextrins to manipulate plasma membrane cholesterol content: evidence, misconceptions and control strategies, *Biochim Biophys Acta.* 1768 (2007) 1311–1324. doi:10.1016/j.bbamem.2007.03.026.
- [62] M. Barriga, R. Cal, N. Cabello, A. Llach, A. Vallmitjana, R. Benítez, L. Badimon, J. Cinca, V. Llorente-Cortés, L. Hove-Madsen, Low density lipoproteins promote unstable calcium handling accompanied by reduced SERCA2 and connexin-40 expression in cardiomyocytes, *PLoS One.* 8 (2013) e58128. doi:10.1371/journal.pone.0058128.
- [63] K. Schlu, R. Schulz, A. Wolf, M. Weber, R. Schreckenber, Oxidized low-density lipoprotein (oxLDL) affects load-free cell shortening of cardiomyocytes

- in a proprotein convertase subtilisin/kexin 9 (PCSK9)-dependent way, *Basic Res Cardiol.* 112 (2017) 1–11. doi:10.1007/s00395-017-0650-1.
- [64] K.M. Anderson, W.P. Castelli, D. Levy, Cholesterol and mortality. 30 years of follow-up from the Framingham study, *JAMA.* 257 (1987) 2176–2180.
- [65] I. Andreadou, E.K. Iliodromitis, A. Lazou, A. Görbe, Z. Giricz, R. Schulz, P. Ferdinandy, Effect of hypercholesterolaemia on myocardial function, ischaemia-reperfusion injury and cardioprotection by preconditioning, postconditioning and remote conditioning, *Br J Pharmacol.* 174 (2017) 1555–1569. doi:10.1111/bph.13704.
- [66] E. Talini, V. Di, C. Bianchi, C. Palagi, M. Grazia, D. Donne, G. Penno, C. Nardi, M. Laura, S. Del, M. Mariani, R. Miccoli, Early impairment of left ventricular function in hypercholesterolemia and its reversibility after short term treatment with rosuvastatin A preliminary echocardiographic study, *Atherosclerosis.* 197 (2008) 346–354. doi:10.1016/j.atherosclerosis.2007.05.024.
- [67] R. Coronel, The pro- or antiarrhythmic actions of polyunsaturated fatty acids and of cholesterol, *Pharmacol. Ther.* 176 (2017) 40–47. doi:10.1016/j.pharmthera.2017.02.004.
- [68] T. Wang, W. Chen, S.S. Su, S. Lo, W. Lin, Y. Lee, Increased cardiomyocyte apoptosis following ischemia and reperfusion in diet-induced hypercholesterolemia: relation to Bcl-2 and Bax proteins and caspase-3 activity, *Lipids.* 37 (2002) 385–394.

Figure subtitles:

Figure 1: 5-week treatment with high cholesterol diet effects on lipid profile and heart size. A) Mean mice bodyweight B) Heart weight normalized by tibia size C) Total serum cholesterol D) Total cellular cholesterol content E) Left ventricle isolated cardiomyocytes capacitance. * $P < 0.05$, compared to control (CTR). N: number of mice analyzed; n: number of cells.

Figure 2: Early stage hypercholesterolemia effects on cardiomyocytes Action Potential (AP). A) Representative traces of control (left panel-CTR) and a cardiomyocyte isolated from hypercholesterolemic mice (Right panel-CHO). B) AP amplitude, measured from resting potential to peak AP voltage. C) Maximum rate of AP depolarization during the upstroke phase. D) Resting membrane potential, measured at no current being clamped. E) Time required to reach 10%; 50% (F) and 90% (G) of AP full repolarization. * $P < 0.05$, compared to control (CTR). n: number of cells.

Figure 3: Early stage hypercholesterolemia effects on cardiomyocytes K^+ currents. A) Representative traces of outward K^+ currents (I_K) from a control (left panel-CTR) and from a high cholesterol-fed mice isolated cardiomyocyte (Right panel-CHO). B) I-V relationship from peak I_K current density against tested membrane potentials. C) Fraction of maximum current (I/I_{MAX}) reached on each tested potential. D) Contribution of kinetically isolated I_K from total outward current at +50 mV. Numbers above bars indicate current components time constant, in (ms). E) Representative traces of inward rectifier K^+ currents (I_{K1}) from a control (left panel-CTR) and from a high cholesterol-fed mice isolated cardiomyocyte (Right panel-CHO). F) I-V relationship from peak I_{K1} current density against tested membrane potentials. * $P < 0.05$, compared to control (CTR). n: number of cells.

Figure 4: Early stage hypercholesterolemia effects on cardiomyocytes L-type Ca^{2+} currents (I_{Ca-L}). A) Representative traces of outward I_{Ca-L} from control (left panel-CTR) and a cardiomyocyte isolated from a high cholesterol-fed mice (Right panel-CHO). B) I-V relationship from peak I_{Ca-L} current density against tested membrane potentials. C) Fraction of maximum conductance (G/G_{MAX}) reached on each tested potential. G_{MAX} was calculated from I-V curve fitting with a Boltzmann equation. D) Steady-state inactivation of I_{Ca-L} . E) Voltage at which half of G_{MAX} is achieved in steady state activation of channels. F) Voltage at which half of I_{Ca-L} current is blocked by a

depolarizing preconditioning pulse in steady state inactivation of channels. G) Cav1.2 protein levels. * $P < 0.05$, compared to control (CTR). n: number of cells.

Figure 5: Early stage hypercholesterolemia effects on cardiomyocytes intracellular Ca^{2+} handling. A) Representative records of Ca^{2+} transients using dual excitation probe Fura2-AM, from a control (left panel-CTR) and a cardiomyocyte isolated from a high cholesterol-fed mice (Right panel-CHO). Transients under beta-adrenergic stimulation with 100 nM isoproterenol (ISO) is also displayed from both CTR and CHO cardiomyocytes. B) Diastolic intracellular Ca^{2+} concentration in the absence or under beta-adrenergic stimulation. C) Peak systolic intracellular Ca^{2+} concentration in the absence or under beta-adrenergic stimulation. D) Time to reach peak intracellular Ca^{2+} transient in the absence or under beta-adrenergic stimulation. E) Time constant for intracellular Ca^{2+} transient decay in the absence or under beta-adrenergic stimulation. * $P < 0.05$, compared to control (CTR); # $P < 0.05$, compared to CHO; & $P < 0.05$, compared to CTR+ISO. n: number of cells.

Figure 6: Early stage hypercholesterolemia effects on cardiomyocytes contractility. A) Representative records of sarcomere contraction, from control (left panel-CTR) and a cardiomyocyte isolated from a high cholesterol-fed mice (Right panel-CHO). Contractions under beta-adrenergic stimulation with 100 nM isoproterenol (ISO) is also displayed from both CTR and CHO cardiomyocytes. B) Sarcomere length in resting cells C) Sarcomere fractional shortening (FS) as a fractional of resting sarcomere size in peak contraction. D) Time to reach 50% and 90% (E) of peak sarcomere contraction. F) Time to reach 90% of full-relaxed sarcomere size from peak contraction. * $P < 0.05$, compared to control (CTR); # $P < 0.05$, compared to CHO. n: number of cells.

Figure 7: Early stage hypercholesterolemia effects on isolated hearts during ischemia-reperfusion. After 30' to allow stabilization of hearts contraction (CTR indicated in the plots), a 30' ischemia was induced by occlusion of the left anterior descending coronary artery. A) Maximum rate of developed pressure (dP/dt) B) developed pressure, measured as the difference between left ventricular systolic pressure and end-diastolic pressure (EDP). C) Left Ventricle end-diastolic pressure (EDP) D) Heart rate. * $P < 0.05$, compared to control (CTR). N: number of mice used in the experiments.

Figure 8: *Early stage hypercholesterolemia effects on mice Electrocardiogram (ECG)*
A) *Representative ECG records from control (left panel-CTR) and a high cholesterol-fed mice (Right panel-CHO).* B) *P wave duration.* C) *PR interval duration* D) *QRS interval duration* E) *T wave duration* F) *Heart rate.* * $P < 0.05$, compared to control (CTR) N: *number of mice used in the experiments.*

Figure 1

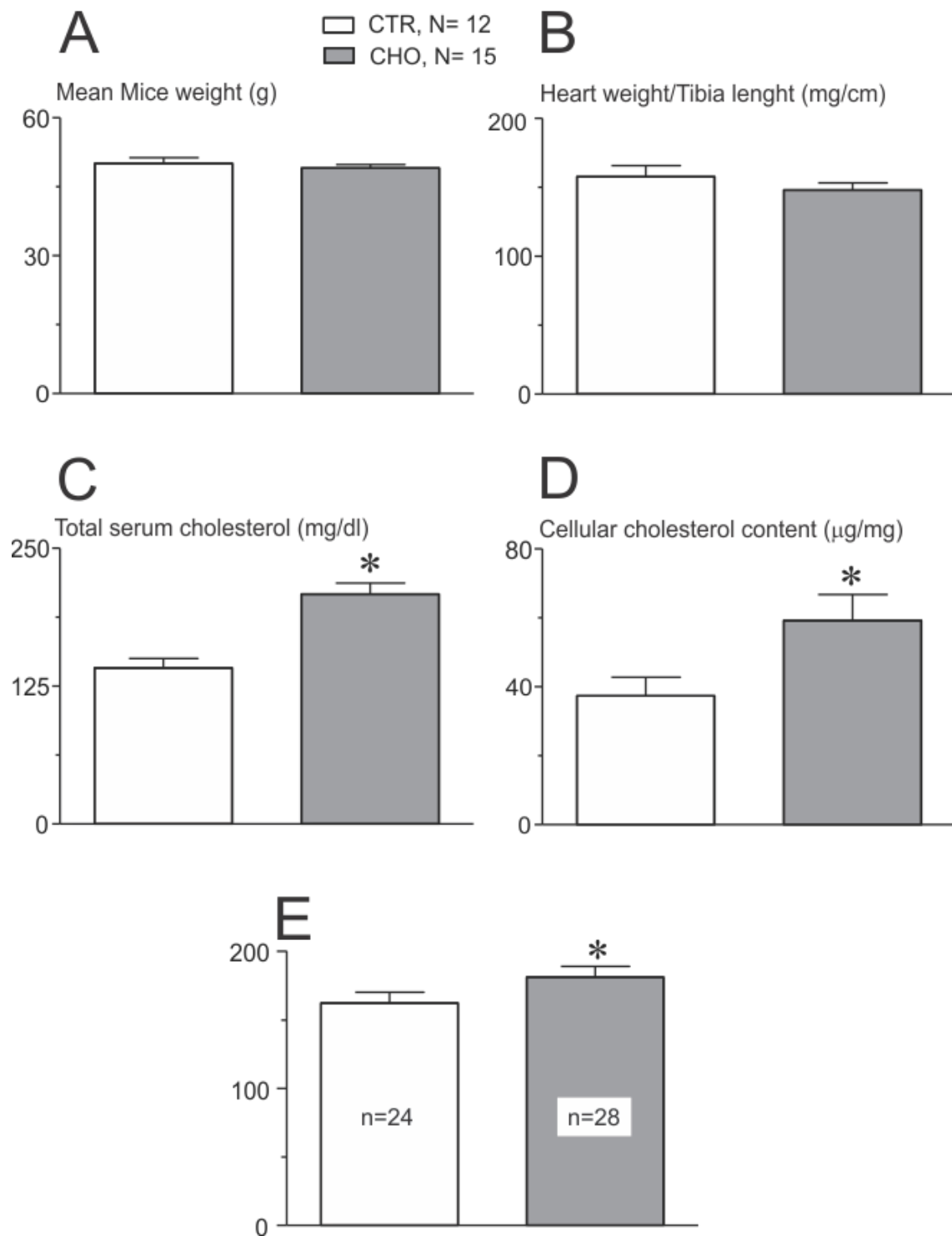
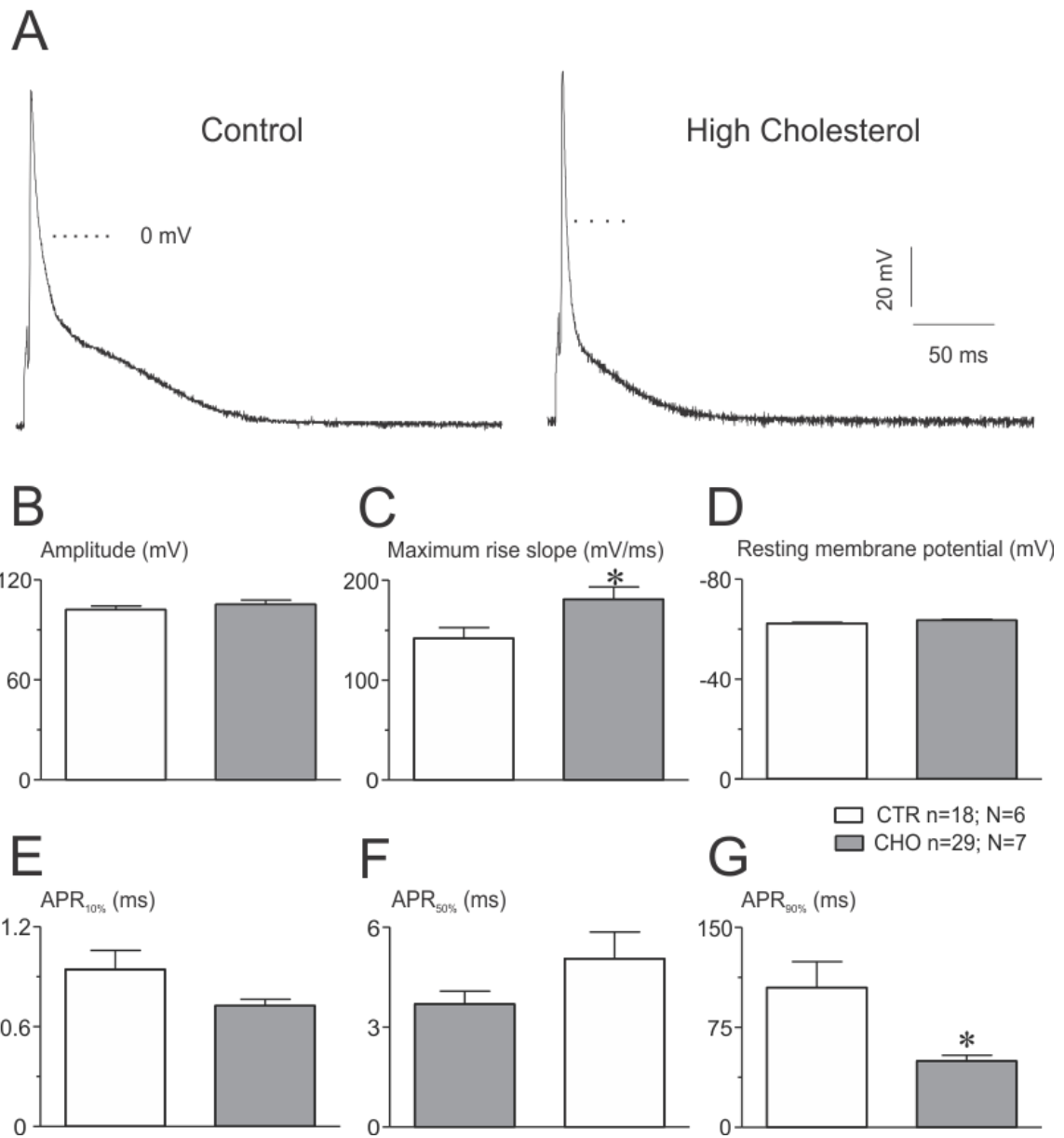


Figure 2



A Figure 3

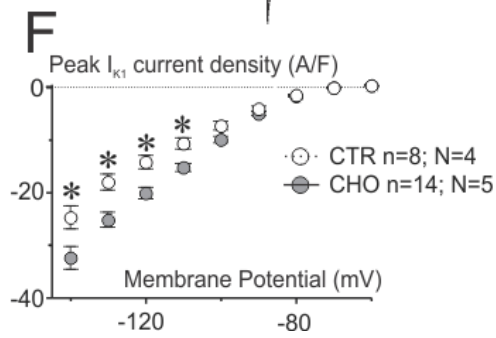
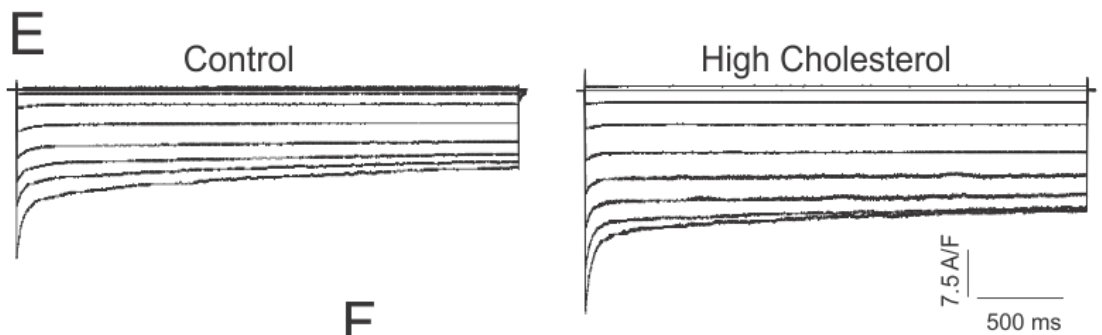
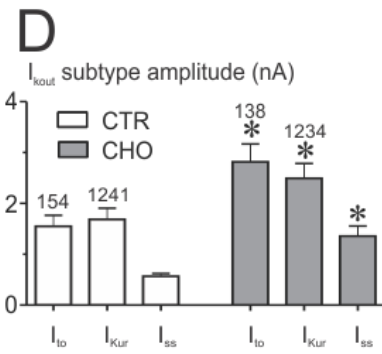
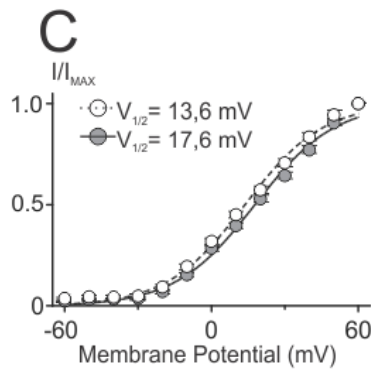
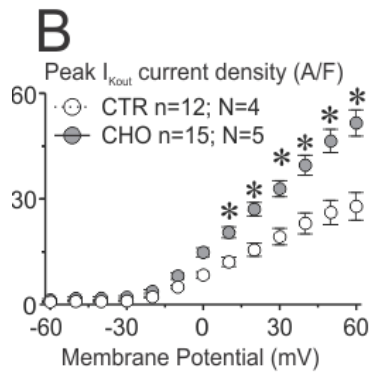
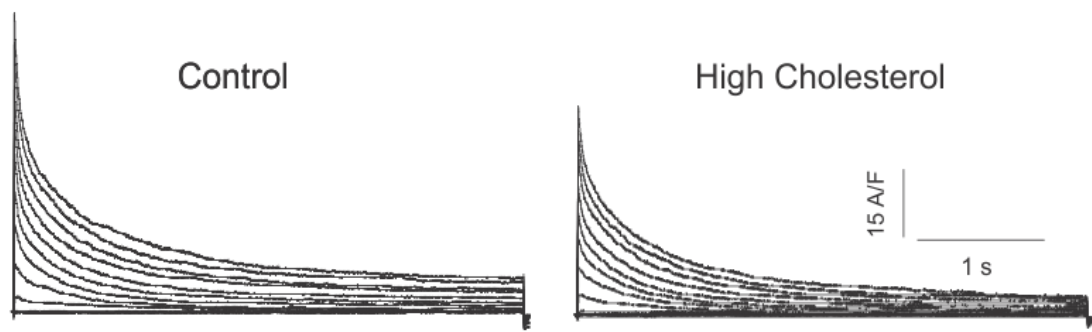


Figure 4

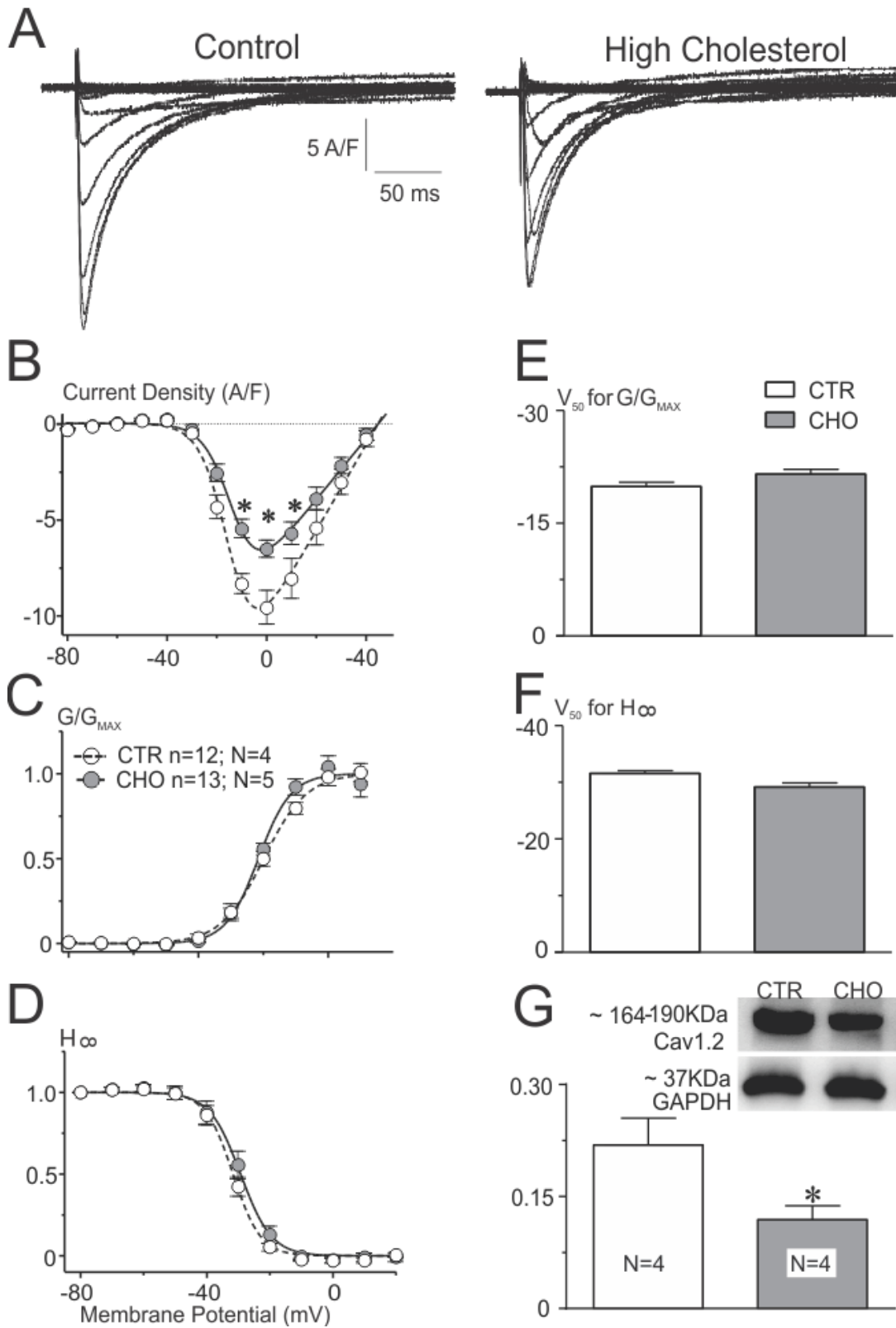


Figure 5

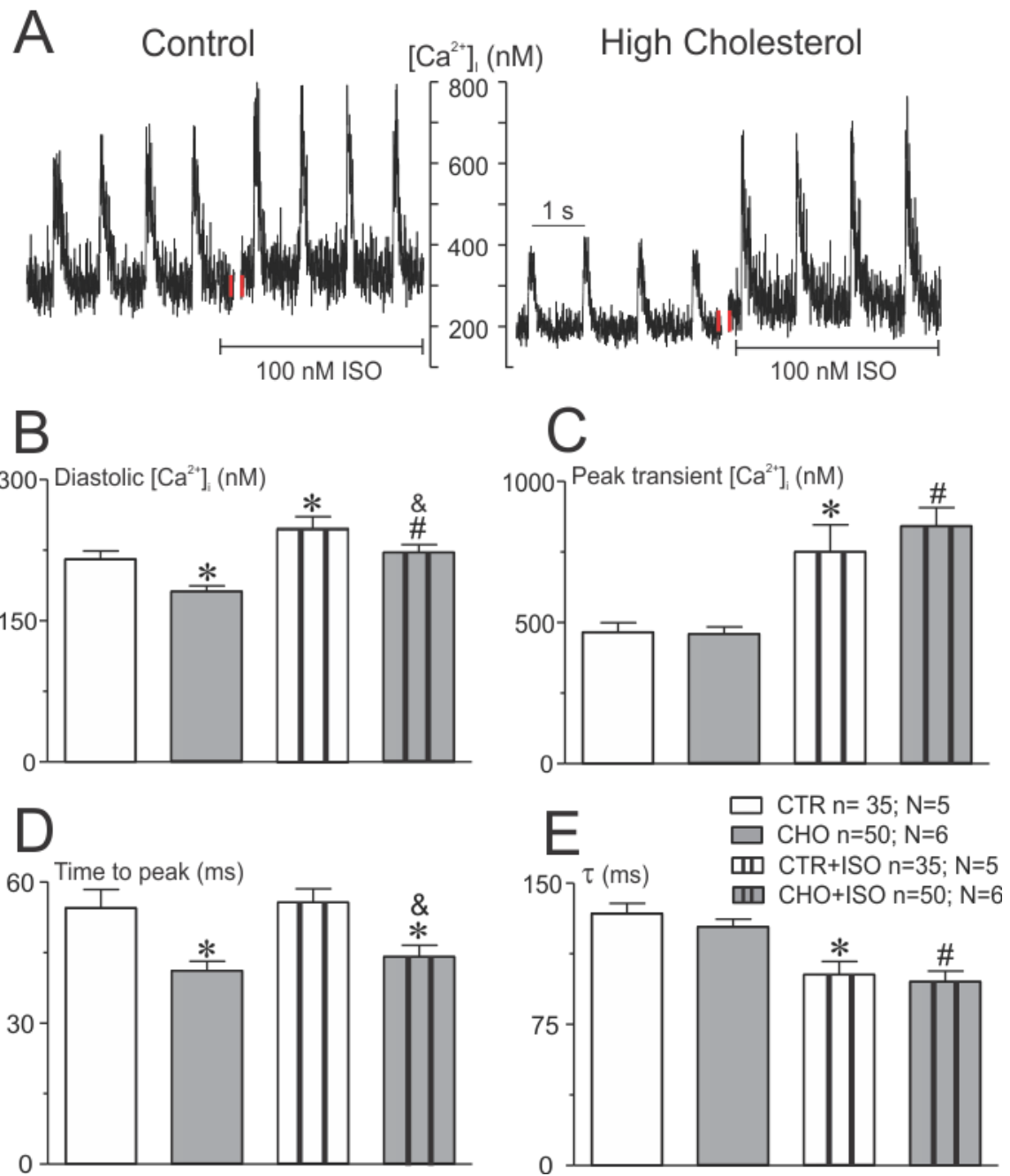


Figure 6

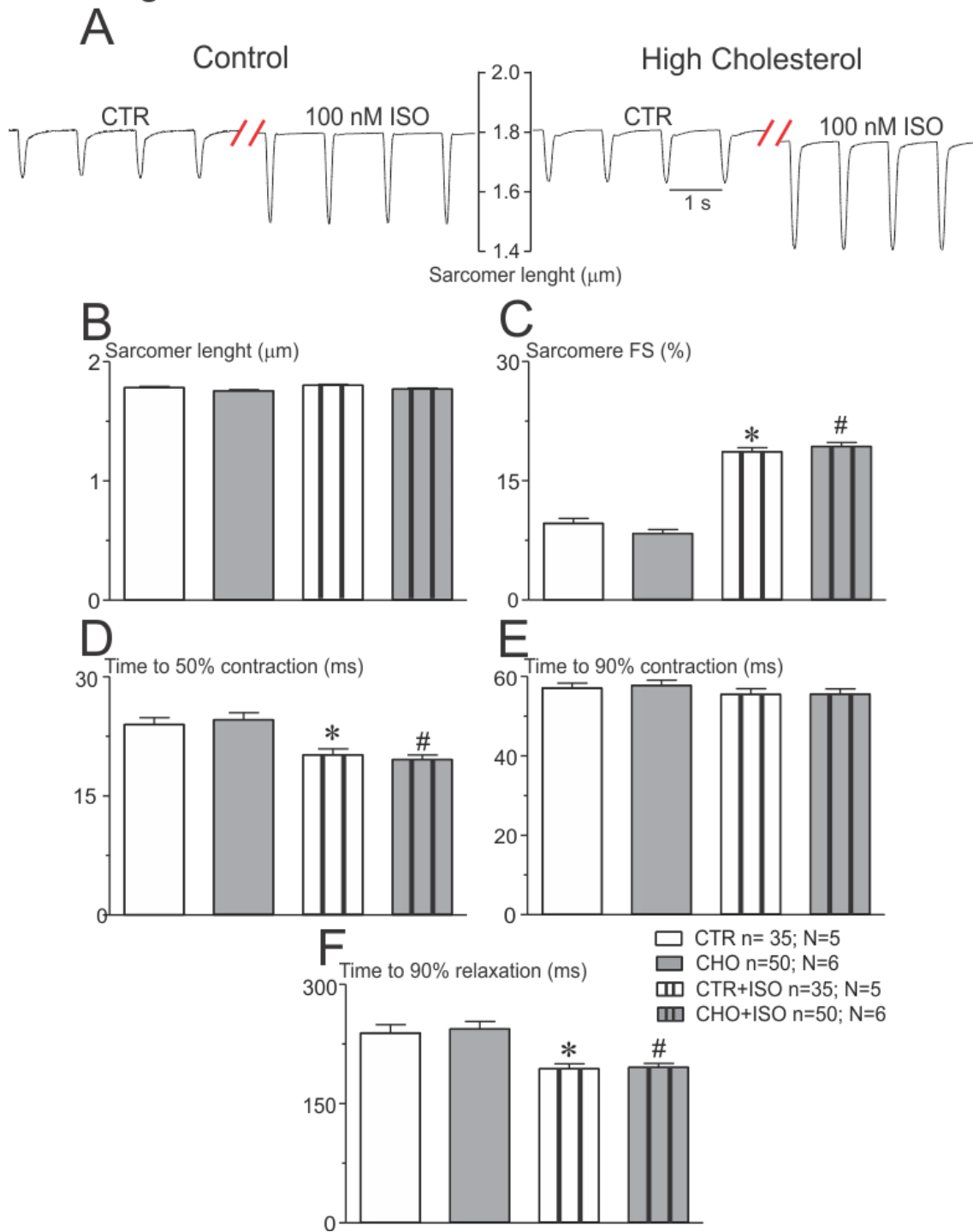


Figure 7

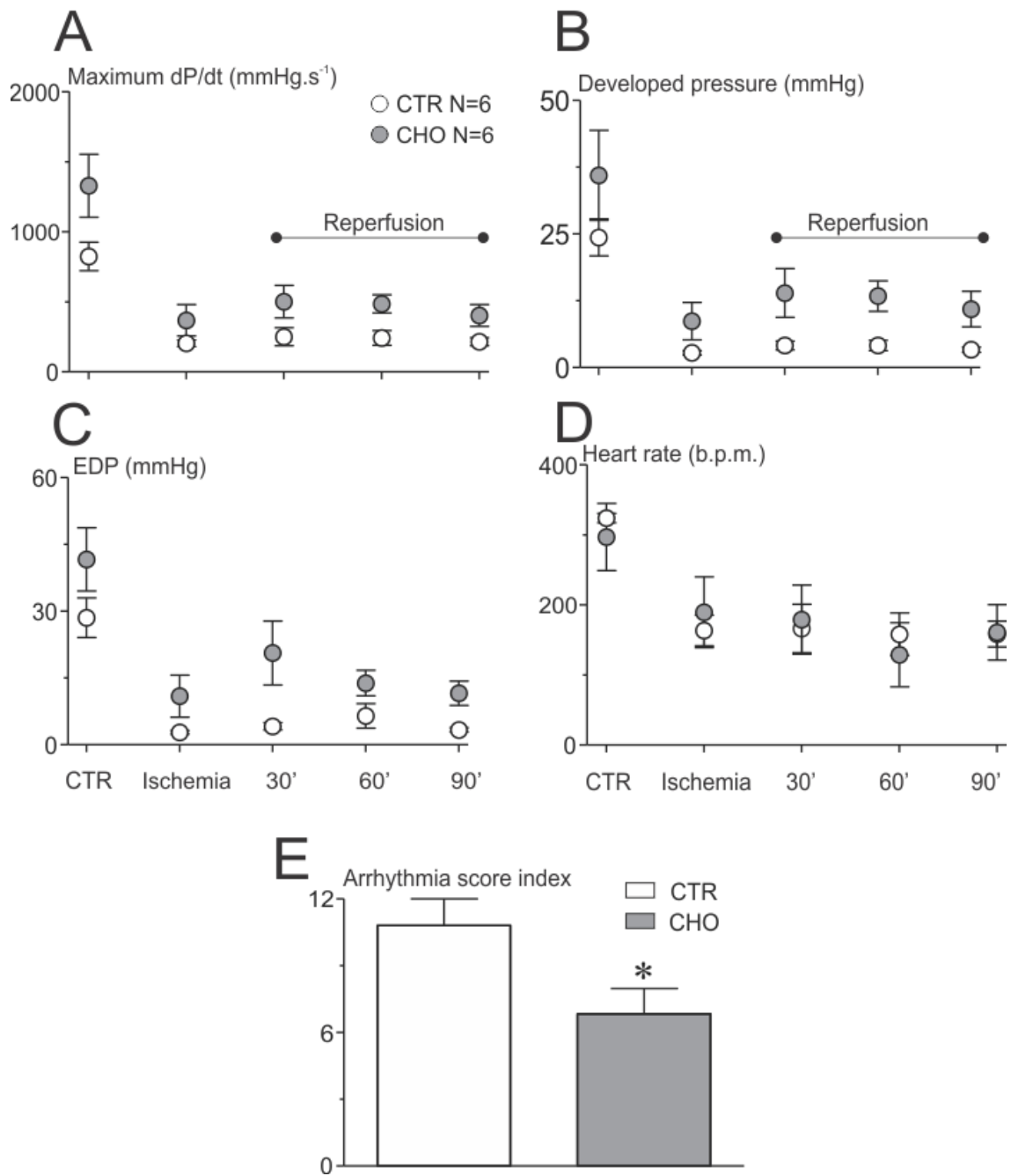
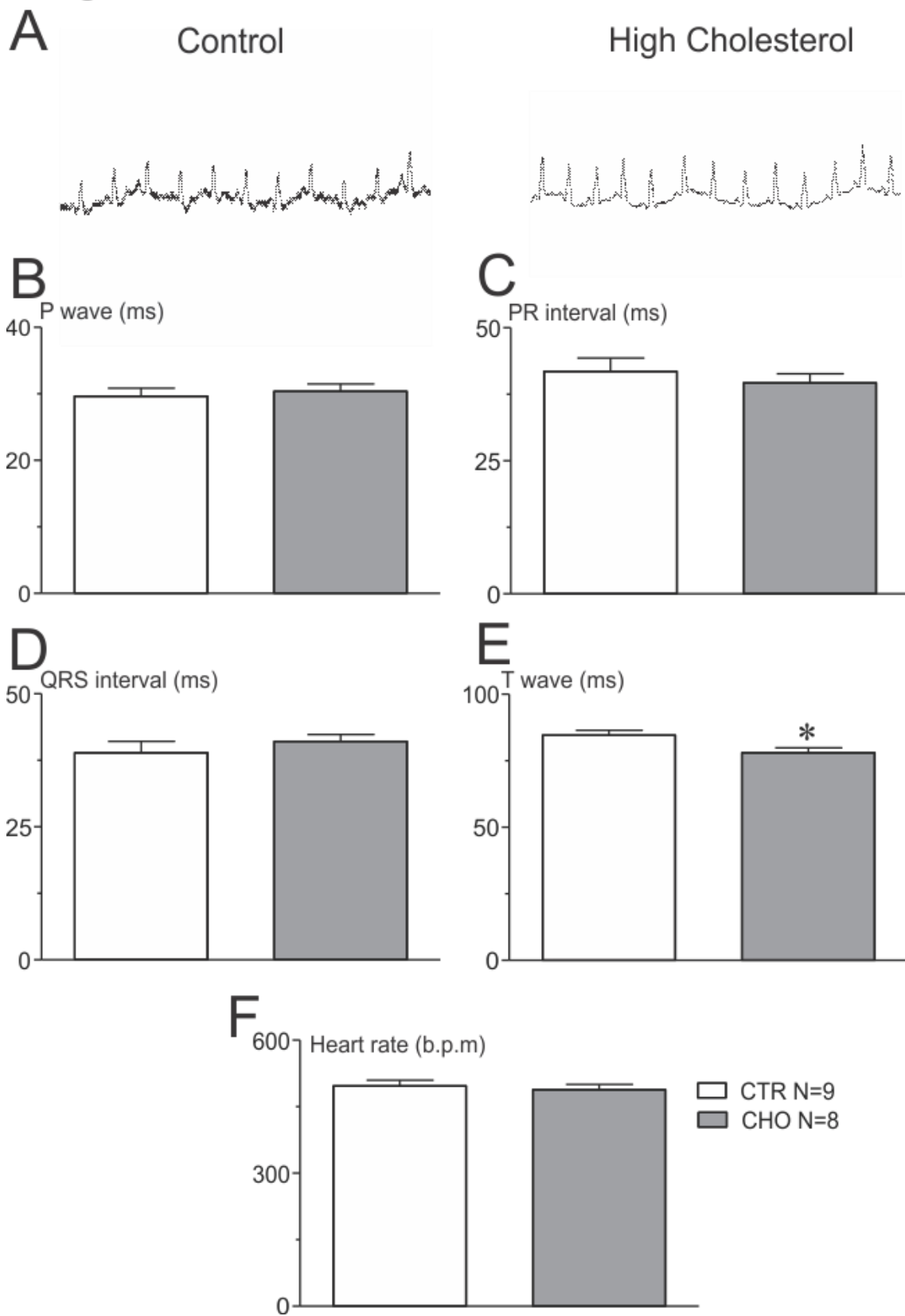


Figure 8



DISCUSSÃO

Durante a execução desse trabalho de doutorado investigamos a associação entre a progressão das alterações teciduais, do perfil inflamatório e da persistência de parasitas no coração durante a transição entre as fases aguda e crônica com as alterações elétricas de cardiomiócitos isolados do ventrículo direito em modelo murino. Além disso, voltamos nossos esforços para o estabelecimento de novas abordagens que complementem o campo de estudo da forma cardíaca da DC, sendo elas: 1- Avaliação funcional das junções GAP expressas no sistema cardiovascular acerca de seus mecanismos regulatórios, dependentes de voltagem, ligantes ou modificações pós-traducionais e como essas alterações interferem com o acoplamento intercelular e 2- Caracterização dos efeitos da hipercolesterolemia na alteração do conteúdo colestérico celular e em nas propriedades elétricas, contráteis e do manejo de Ca^{2+} no coração e em cardiomiócitos isolados. Esperamos que os esforços combinados desse trabalho contribuam significativamente para a ampliação das estratégias para o estudo da forma cardíaca da DC, fornecendo evidências importantes para a consolidação do conhecimento sobre os mecanismos determinantes para a progressão das disfunções cardiovasculares. Finalmente, esperamos que as estratégias propostas possam fornecer ferramentas para a avaliação de novos alvos terapêuticos mais acurados e efetivos no tratamento dessa enfermidade.

Status da pesquisa em alterações eletromecânicas e de mecanismos celulares na fase cardíaca da DC

A DC possui uma progressão complexa, em função da presença de duas fases sintomáticas distintas, aguda e crônica⁶⁵. Além disso, o prognóstico da doença é regido por uma combinação de fatores que envolvem a cepa do parasita, com seus tropismos tecido-específico e virulência característica, o que está correlacionado com a diferença nas manifestações da doença em diferentes regiões endêmicas^{101, 102}. A resposta imune característica do hospedeiro também é fator determinante na progressão da DC. Finalmente, o resultado da doença é influenciado por fatores ambientais, como estado nutricional dos pacientes, de modo que deficiências nutricionais já foram descritas como

determinando prejuízo na progressão de doenças infecciosas ¹⁰³ e particularmente em modelos experimentais de infecção com *T. cruzi* ^{104, 105, 106, 107}.

Em humanos, as manifestações cardíacas observáveis são muito variadas, e depende, além dos fatores citados acima, da forma de infecção ⁶⁶. De maneira simplificada, a progressão da DC entre as fases aguda e crônica é acompanhada por uma piora na fase cardíaca. Na fase aguda, observa-se sintomas não específicos como febre, miocardite e meningocefalite, sendo esses dois últimos sintomas, os principais responsáveis pela mortalidade de 5% associada à fase aguda ⁶⁶. A fase crônica, por outro lado, possui uma variabilidade de sintomas mais acentuados, e pode envolver formas cardíaca, digestiva ou uma combinação dos dois ^{108, 109, 110}. Na fase cardíaca, diversas formas de arritmias são observadas, mas a presença de bloqueio de ramo direito combinado com bloqueio fascicular anterior esquerdo é muito comum, bem como taquicardias ventriculares sustentadas ⁶⁶. Entretanto, outras formas complexas de arritmias, incluindo bloqueios atrioventriculares, batimentos prematuros, em combinação com alteração da duração da onda T e amplitude elevada da onda R, e desnivelamento do intervalo ST são também observáveis ^{111, 109, 110, 112}. A diversidade de disfunções elétricas está correlacionada com alterações estruturais severas no tecido cardíaco, que incluem aneurisma apical, fibrose tecidual, tromboembolismo, regurgitação das valvas cardíacas ¹¹², finalmente culminando para a insuficiência cardíaca nos estágios mais avançados da doença.

Apesar da diversidade dos sintomas apresentados acima, os tratamentos para a DC se concentram na utilização de drogas antiparasitárias ¹¹³ em associação com drogas para a amenização dos sintomas cardíacos ⁶³. Entretanto, os tratamentos não são muito eficazes, principalmente na fase crônica (50-80% na fase aguda e 8-20% na fase crônica) ^{114, 115}. Notoriamente para quadros mais avançados da fase crônica da DC, distúrbios elétricos e contráteis frequentemente aparecem de maneira simultânea, dificultado o tratamento dos sintomas, uma vez que fármacos que beneficiam o desempenho contrátil do coração muitas vezes aumentam o risco de arritmias cardíacas ¹¹⁶.

O uso de modelos animais como estratégia para se recapitular a DC determinou grande avanço no entendimento dos mecanismos celulares e moleculares associados à infecção pelo *T. cruzi*. Diferentes grupos de pesquisa voltaram seus esforços para a caracterização do perfil inflamatório ^{89, 117, 118}, das alterações oxidativas no hospedeiro ^{89, 117}, da variabilidade genética do parasita e hospedeiro como resultante da infecção ¹¹⁹

e de estratégias para o controle do vetor triatomíneo. Particularmente, nosso grupo de pesquisa contribuiu de maneira principal para a caracterização das disfunções elétricas e contráteis do coração e de cardiomiócitos isolados que acompanham as fases aguda e crônica da DC ^{70, 71, 72, 92}. Nesse contexto, os experimentos apresentados no capítulo 1 desse trabalho contribuíram para o entendimento da associação entre alterações elétricas de cardiomiócitos ventriculares com a progressão entre a fase aguda e crônica da doença, no ventrículo direito. Disfunções do ventrículo direito já eram conhecidas na DC ^{120, 121}, entretanto, os mecanismos celulares e moleculares ainda não são bem elucidados. Em nosso trabalho, reportamos uma alteração inflamatória sustentada, com depósito de colágeno no tecido cardíaco, que é acompanhada por alteração nas correntes de K⁺ e Ca²⁺ em cardiomiócitos isolados, as quais também são comparáveis entre as fases aguda e crônica. Essas alterações ocorrem na presença de marcadores para a presença do *T. cruzi* no tecido cardíaco, mesmo na fase crônica.

Naturalmente o avanço em cada uma das esferas descritas acima para o controle da infecção pelo *T. cruzi* culmina para a sobreposição dos mecanismos estudados em outras áreas. O estresse oxidativo associado à DC já foi reportado em diversos estudos, associado a diferentes componentes celulares, incluindo disfunção mitocondrial ^{81, 82, 83, 122}, falha nos sistemas antioxidantes ^{81, 82}; atividade de NADPH oxidases ¹²³. Além disso, tratamentos com antioxidantes foram capazes de prevenir ¹²⁴ e até reverter a doença ⁸⁵. Entretanto, espécies reativas são moduladores importantes da função elétrica e contrátil de cardiomiócitos, alterando diretamente sua função pela oxidação / nitração de resíduos de aminoácidos, ou indiretamente, pela modulação de vias de sinalização intracelular que interfiram com a atividade desses canais ^{12, 86, 87, 125}. Além disso, a magnitude de alterações oxidativas e das propriedades eletrocontráteis cardíacas são ainda moduladas pela resposta inflamatória à infecção, particular a cada paciente.

O status atual da pesquisa para avanços no entendimento dos mecanismos determinantes para a progressão da DC enfrenta um paradoxo inerente da especialização dos grupos de pesquisa nas esferas de atuação descritas acima. Muitos avanços foram realizados para o entendimento dos mecanismos associados ao prognóstico da DC. Entretanto, as contribuições desses estudos ocorrem de maneira isolada, e após mais de 100 anos da identificação da DC por Carlos Chagas, o tratamento dessa patologia é impreciso e ineficiente ¹¹⁴. É necessário, pois que estudos incorporando o conhecimento reportado nas diferentes subáreas de estudo sejam conduzidos com o intuito de se propor

novas estratégias de tratamento, que conciliem a amenização dos sintomas progressivos dessa patologia com o controle da carga parasitária nos pacientes. Além disso, os estudos investigando a participação de componentes isolados da maquinaria e vias de sinalização celular devem ser continuados, enriquecendo o conhecimento da etiologia, da infecção nos modelos experimentais e atribuindo valores relativos das contribuições de cada um desses componentes para o resultado da doença. A soma dessas duas estratégias otimizam as perspectivas para o desenvolvimento de uma abordagem nova e efetiva para o tratamento da DC.

Junções GAP e a DC

Como discutido na seção anteriormente, muitas das manifestações clínicas da DC são derivadas de alterações das propriedades elétricas do coração, bem como de distúrbios de condução ⁶⁶. A nível celular, o principal sistema de comunicação intercelular, que garante a propagação elétrica no miocárdio é formado pelas junções GAP ³³. No coração de mamíferos, tipicamente as junções GAP são formadas por Cx40, Cx43 e Cx45, sendo que Cx40 e Cx43 são preferencialmente expressas nos átrios, Cx43 é dominante nos ventrículos, Cx45 é dominante nas células nodais e as 3 isoformas são encontradas no sistema de condução ventricular ^{25, 34, 126}. Apesar da diversidade de distúrbios de condução comuns na DC, os estudos envolvendo a avaliação das junções GAP nessa patologia são muito limitados. Alteração na distribuição das placas de junções GAP em cardiomiócitos infectados com *T. cruzi* ^{80, 127}, estudada pela marcação de Cx43 e imageamento celular em modelo experimental. Além disso, a magnitude do acoplamento juncional entre pares de células foi encontrado reduzida após 72h de infecção ⁸⁰. A redução de Cx43 e alteração de sua distribuição foi também encontrada em pacientes acometidos pela DC ⁹³. A redução na expressão de Cx43, entretanto, parece estar relacionada majoritariamente às células infectadas, enquanto células vizinhas não infectadas apresentam expressão e distribuição regular de Cx43 ¹²⁷.

Os estudos envolvendo o papel das junções GAP na DC até o momento, no entanto, são limitados em 2 aspectos principais: 1- a maioria deles aborda a expressão e localização das junções GAP, mas desprezam a investigação das propriedades biofísicas do acoplamento juncional intercelular. 2- Os estudos são limitados à Cx43, desprezando a contribuição das outras isoforma cardíacas, Cx40 e Cx45. Entretanto, Cx45 é a isoforma

dominante nas células nodais ²⁵, bem como Cx40 e Cx45 contribuem de maneira importante para as conexinas expressas no sistema de condução ventricular ²⁵. Como descrito anteriormente, a DC apresenta comumente distúrbios de condução como bloqueios de condução do feixe de His e bloqueio atrioventricular ^{66, 109, 110, 111, 112}. É seguro dizer que o papel das junções GAP no estabelecimento das disfunções elétricas da forma cardíaca da DC é, no mínimo, ainda pouco compreendido.

Com o objetivo de nos aprofundarmos no estudo do papel desses canais intercelulares nos distúrbios cardíacos que acometem pacientes com DC, buscamos um aprimoramento técnico para a execução de experimentos e delineamento de estratégias experimentais para o estudo do acoplamento funcional das junções GAP cardíacas. Caracterizamos a capacidade das conexinas expressas no sistema vascular em se agrupar de maneira funcional, bem como investigamos as propriedades funcionais de seu acoplamento. Além disso, investigamos a influência do aumento da temperatura nas propriedades funcionais de junções GAP cardíacas formadas por Cx40 e Cx45. Mostramos que os canais heterotípicos formados por conexinas expressas no sistema vascular são funcionais e possuem um acoplamento junctional muito sensível à voltagem, de modo que alterações muito pequenas de voltagem (da ordem de 5-10mV) promovem significativo desacoplamento intercelular. Esses resultados assumem um papel importante, principalmente considerando a capacidade do *T. cruzi* em infectar células do músculo liso vascular ⁹⁵, e aponta para a importância desses canais na regulação da função vascular durante a DC.

Em um segundo grupo de resultados do capítulo 2 desse trabalho, mostramos que o aumento da temperatura não tem efeito significativo da desativação estacionária e recobro estacionário da desativação de Cx45 e Cx40, ainda que a cinética desses processos seja acelerado pelo aumento da temperatura. A soma da contribuição cinética desses processos antagônicos determina um desacoplamento dinâmico similar para as temperaturas testadas no caso de Cx45, enquanto para Cx40, não ocorre desacoplamento dinâmico para os intervalos testados. Esses resultados apontam para a independência da temperatura para o desacoplamento dinâmico de Cx45. Esse dado é relevante para o estudo da DC por dois fatores principais: 1- o desacoplamento entre células nodais pode ser um fator determinante para bloqueios de condução, uma vez que a presença de tecido não excitável ao redor do NAV converge o impulso elétrico do coração para essa região ^{15, 17} e 2- a DC é uma patologia de caráter inflamatório crônico ^{89, 92}, e o aumento da

temperatura corporal é sintoma inespecífico dessa doença ¹¹⁰ esse sintoma em si não parece ser suficiente para engatilhar o desacoplamento dinâmico funcional em células nodais.

Hipercolesterolemia e a DC

Na primeira seção foi discutido os aspectos clínicos da DC, os avanços obtidos no entendimento da etiologia da doença e as limitações atuais da aplicação desses avanços para a melhora da condição dos pacientes acometidos. Na segunda seção, discutimos o conhecimento atual das junções GAP na DC, bem como as novas estratégias para se abordar a participação desses canais intercelulares no estabelecimento e progressão dessa patologia. Nessa última seção será abordado uma estratégia para se investigar de maneira mais compreensiva os efeitos de desbalanços nutricionais no resultado da DC.

Como descrito anteriormente, deficiências nutricionais afetam de maneira importante a progressão de doenças infecciosas e particularmente a DC ^{104, 105, 106, 107, 106}. Nesse sentido, dislipidemias assumem um papel importante, tanto pelo alta prevalência do consumo de dietas ricas em gorduras no continente americano e europeu, que compreendem a maioria dos casos de DC (*WHO observatory data 2018*) quanto capacidade do *T. cruzi* em infectar adipócitos ¹²⁸ bem como interagir com lipoproteínas ^{98, 99} e seus receptores celulares ⁹⁸.

Dietas ricas em gordura reduziram mortalidade, parasitemia e carga parasitária no coração, ainda que a carga de *T. cruzi* no tecido adiposo tenha aumentado ¹²⁹. Além disso, a infecção pelo *T. cruzi* em associação com dieta hiperlipidêmica e rica em colesterol determina um elevado potencial para o desenvolvimento de aterosclerose. Finalmente, a infecção de células por esse parasita está associada com o aumento do conteúdo de colesterol intracelular. A soma dessas evidências aponta para a importância de dislipidemias na infecção pelo *T. cruzi*. O último capítulo desse trabalho foi baseado na caracterização dos efeitos diretos da hipercolesterolemia no coração e em cardiomiócitos isolados em modelo murino. Observamos que mesmo em estágios iniciais da hipercolesterolemia é possível observar aumento no conteúdo de colesterol dos cardiomiócitos. Esse aumento é acompanhado por alterações nas correntes de K^+ e Ca^{2+} dos cardiomiócitos, o que reflete encurtamento do PA e uma redução do intervalo QT desses animais. As alterações elétricas parecem estar correlacionadas com uma proteção

parcial para o desenvolvimento de arritmias cardíacas durante a isquemia / reperfusão de corações isolados desses animais. Finalmente, ao contrário da excitabilidade cardíaca, aspectos contráteis do coração e de cardiomiócitos isolados encontram-se preservados após tratamento com dieta rica em colesterol. De porte desses resultados, espera-se contribuir com a literatura da DC através do delineamento de infecções experimentais em conjunto com a administração de dieta rica em colesterol, de modo a esclarecer a participação dessa dislipidemia no resultado da DC.

CONCLUSÕES

Diante dos resultados apresentados nesse trabalho, conclui-se que a investigação do papel das junções GAP e de dislipidemias como determinantes da progressão da DC são perspectivas importantes para estudos posteriores, e nesse trabalho apresentamos um embasamento teórico e prático que nortearão esses estudos. Além disso, esforços coletivos em diferentes esferas do estudo dos determinantes para o resultado da DC devem ser continuados, enriquecendo o volume de informação disponível acerca dessa complexa patologia. Entretanto, deve-se buscar uma associação entre essas esferas de estudo com o propósito de desenvolver estratégias mais efetivas para o tratamento da DC, tanto no controle parasitário quando para a melhora da qualidade de vida dos pacientes acometidos.

REFERÊNCIAS

1. Romer, A. & Parsons, T. *Anatomia Comparada dos Vertebrados*. (1985).
2. Randall, D., Burggren, W. & French, K. *Eckert Fisiologia Animal: Mecanismos e Adaptações*. (2011).
3. Guyton, A. & Hall, J. *Tratado de fisiologia médica*. (2006).
4. Katz, A. M. *Physiology of the heart*. Ed. Raven Press, 4 ed. (2006).
5. Berne, R., Levy, M., Koeppen, B. & Stanton, B. *Fisiologia*. (2009).
6. Heneine, I. F. *Biofísica básica. Rio de Janeiro: Atheneu, 1984-2000. 391p*. (2010).
7. Chaui-berlinck, J. G., Henrique, L. & Monteiro, A. Frank-Starling Mechanism and Short-Term Adjustment of Cardiac Flow. *J. Exp. Biol.* **220**, 4391–4398 (2017).
8. Bers, D. *Excitation-contraction coupling and cardiac contractile force*. (2001).
9. Bers, D. Cardiac excitation–contraction coupling. *Nature* **415**, 198–205 (2002).
10. Bers, D. M. & Guo, T. Calcium signaling in cardiac ventricular myocytes. *Ann. N. Y. Acad. Sci.* **1047**, 86–98 (2005).
11. Bers, D. M. Calcium cycling and signaling in cardiac myocytes. *Annu Rev Physiol* **70**, 23–49 (2008).
12. Aggarwal, N. T. & Makielski, J. C. Redox control of cardiac excitability. *Antioxid Redox Signal* **18**, 432–468 (2013).
13. Malmivuo, J. & Plonsey, R. *Bioelectromagnetism - Principles and Applications of Bioelectric and Biomagnetic Fields*. (1995).
14. Fabiato, A. & Fabiato, F. Calcium and cardiac excitation-contraction coupling. *Annu Rev Physiol* 473–484 (1979).
15. Anderson, R. H., Gianni, J., Boyett, M. R., Chandler, N. J. & Dobrzynski, H. The Anatomy of the Cardiac Conduction System. *Clin Anat.* **22**, 99–113 (2009).
16. Greener, I. D. *et al.* Molecular architecture of the human specialised atrioventricular conduction axis. *J. Mol. Cell. Cardiol.* **50**, 642–651 (2011).
17. Meijler, F. & Janse, M. Morphology and electrophysiology of the mammalian atrioventricular node. *Physiol Rev.* **68**, 608–647 (1988).
18. Yoo, S. *et al.* Localization of Na⁺ channel isoforms at the atrioventricular junction and atrioventricular node in the rat. *Circulation* **114**, 1360–1371 (2006).
19. Greener, I. D. *et al.* Ion channel transcript expression at the rabbit atrioventricular conduction axis. *Circ Arrhythm Electrophysiol* **2**, 305–315 (2009).
20. Temple, I. P., Inada, S., Dobrzynski, H. & Boyett, M. R. Connexins and the atrioventricular node. *Hear. Rhythm* **10**, 297–304 (2013).
21. Conde-Garcia, E. *Biofísica*. (1998).

22. Nerbonne, J. M. & Kass, R. S. Molecular physiology of cardiac repolarization. *Physiol Rev* **85**, 1205–1253 (2005).
23. Marger, L. *et al.* Pacemaker activity and ionic currents in mouse atrioventricular node cells. *Channels (Austin)* **5**, 241–250 (2011).
24. Barr, L., Dewey, M. M. & Berger, W. Propagation of action potentials and the structure of the nexus in cardiac muscle. *J Gen Physiol* **48**, 797–823 (1965).
25. Davis, L. M., Rodefeld, M. E., Green, K., Beyer, E. C. & Saffitz, J. E. Gap Junction Protein Phenotypes of the Human Heart and Conduction System. *J Cardiovasc Electrophysiol.* **6**, 813–822 (1995).
26. Kumar, N. M. & Gilula, N. B. The gap junction communication channel. *Cell* **84**, 381–388 (1996).
27. Goldberg, G. S., Lampe, P. D. & Nicholson, B. J. Selective transfer of endogenous metabolites through gap junctions composed of different connexins. *Nat Cell Biol.* **1**, 457–459 (1999).
28. Goodenough, D. A. & Paul, D. L. Gap Junctions. *Cold Spring Harb Perspect Bio* **1**, 1–19 (2009).
29. Saez, J. C., Berthoud, V. M., Branes, M. C., Martinez, A. D. & Beyer, E. C. Plasma membrane channels formed by connexins: their regulation and functions. *Physiol Rev* **88**, 1359–1400 (2003).
30. Sohl, G. & Willecke, K. Gap junctions and the connexin protein family. *Cardiovasc. Res.* **62**, 228–232 (2004).
31. Bai, D., Yue, B. & Aoyama, H. Crucial motifs and residues in the extracellular loops influence the formation and specificity of connexin docking. *Biochim Biophys Acta Biomembr.* **1860**, 9–21 (2018).
32. Milks, L. C., Kumar, N. M., Houghten, R., Unwin, N. & Gilula, N. B. Topology of the 32-kd liver gap junction protein determined by site-directed antibody localizations. *EMBO J* **7**, 2967–2975 (1988).
33. Gros, D. B. & Jongsma, H. J. Connexins in mammalian heart. *BioEssays* **18**, 719–730 (1996).
34. Vozzi, C., Dupont, E., Coppen, S. R., Yeh, H. & Severs, N. J. Chamber-related Differences in Connexin Expression in the Human Heart. *J Mol Cell Cardiol* **31**, 991–1003 (1999).
35. Kim, N. K., Santos-Miranda, A., Chen, H., Aoyama, H. & Bai, D. Heterotypic docking compatibility of human connexin37 with other vascular connexins. *J. Mol. Cell. Cardiol.* **127**, 194–203 (2019).
36. de Wit, C., Boettcher, M. & Schmidt, V. J. Signaling across myoendothelial gap junctions--fact or fiction? *Cell Commun Adhes* **15**, 231–245 (2008).
37. Johnson, R., Hammer, M., Sheridan, J. & Revel, J. Gap junction formation between reaggregated Novikoff hepatoma cells. *Proc Natl Acad Sci U S A* **71**, 4536–4540 (1974).
38. Sandow, S. L. & Hill, C. E. Incidence of myoendothelial gap junctions in the

- proximal and distal mesenteric arteries of the rat is suggestive of a role in endothelium-derived hyperpolarizing factor-mediated responses. *Circ Res* **86**, 341–346 (2000).
39. Bergoffen, J. *et al.* Connexin mutations in X-linked Charcot-Marie-Tooth disease. *Science (80-.)*. **262**, 2039–2042 (1993).
 40. Liu, X. Z. *et al.* Mutations in the myosin VIIA gene cause non-syndromic recessive deafness. *Nat Genet* **16**, 188–190 (1997).
 41. Shiels, A. *et al.* A missense mutation in the human connexin50 gene (GJA8) underlies autosomal dominant ‘zonular pulverulent’ cataract, on chromosome 1q. *Am J Hum Genet.* **62**, 526–532 (1998).
 42. Laird, D. W. Life cycle of connexins in health and disease. *Biochem J* **394**, 527–543 (2006).
 43. Bukauskas, F. F. & Verselis, V. K. Gap junction channel gating. *Biochim Biophys Acta* **1662**, 42–60 (2004).
 44. González, D., Gómez-Hernández, J. M. & Barrio, L. C. Molecular basis of voltage dependence of connexin channels: an integrative appraisal. *Prog Biophys Mol Biol* **94**, 66–106 (2007).
 45. Tejada, M. G. *et al.* Variants with increased negative electrostatic potential in the Cx50 gap junction pore increased unitary channel conductance and magnesium modulation. *Biochem J* **475**, 3315–3330 (2018).
 46. Peracchia, C. Chemical gating of gap junction channels Roles of calcium , pH and calmodulin. *Biochim Biophys Acta* **1662**, 61–80 (2004).
 47. Leithe, E., Mesnil, M. & Aasen, T. The connexin 43 C-terminus: A tail of many tales. *Biochim Biophys Acta Biomembr* **1860**, 48–64 (2018).
 48. Singer, S. & Nicolson, G. The fluid mosaic model of the structure of cell membranes. *Science (80-.)*. **175**, 720–731 (1972).
 49. Nicolson, G. L. The Fluid-Mosaic Model of Membrane Structure: still relevant to understanding the structure, function and dynamics of biological membranes after more than 40 years. *Biochim Biophys Acta* **1838**, 1451–66 (2014).
 50. Karnovsky, M. J., Kleinfeld, A. M., Hoover, R. L. & Klausner, R. D. The concept of lipid domains in membranes. *J Cell Biol* **94**, 1–6 (1982).
 51. Simons, K. & Ikonen, E. Functional rafts in cell membranes. *Nature* **387**, 569–572 (1997).
 52. Ikonen, E. Cellular cholesterol trafficking and compartmentalization. *Nat Rev Mol Cell Biol* **9**, 125–138 (2008).
 53. Dupree, J. L. & Pomicter, A. D. Prostaglandins and other lipid mediators myelin, DIGs, and membrane rafts in the central nervous system. *Prostaglandins Other Lipid Mediat.* **91**, 118–129 (2010).
 54. Pike, L. J. Lipid rafts: heterogeneity on the high seas. *Biochem J* **378**, 281–292 (2004).

55. Simons, K. & Toomre, D. Lipid rafts and signal transduction. *Nat Rev Mol Cell Biol* **1**, 31–39 (2000).
56. Dart, C. Lipid microdomains and the regulation of ion channel function. *J Physiol* **588**, 3169–3178 (2010).
57. Maguy, A., Hebert, T. E. & Nattel, S. Involvement of lipid rafts and caveolae in cardiac ion channel function. *Cardiovasc. Res.* **69**, 798–807 (2006).
58. Balijepalli, R. C. & Kamp, T. J. Caveolae , ion channels and cardiac arrhythmias. *Prog. Biophys. Mol. Biol.* **98**, 149–160 (2009).
59. Beigi, F. *et al.* Cardiac Nitric Oxide Synthase-1 Localization Within the Cardiomyocyte is Accompanied by the Adaptor Protein, CAPON. *Nitric Oxide* **21**, 226–233 (2012).
60. Coura, J. R. & Viñas, P. A. Chagas disease: a new worldwide challenge. *Nature* **465**, 6–7 (2010).
61. Andrade, L. O. & Andrews, N. W. The Trypanosoma cruzi-host-cell interplay: location, invasion, retention. *Nat Rev Microbiol* **3**, 819–823 (2005).
62. Strasen, J. *et al.* Epidemiology of Chagas disease in Europe: many calculations, little knowledge. *Clin Res Cardiol* **103**, 1–10 (2014).
63. Nunes, M. C., Dones, W., Morillo, C. A., Encina, J. J. & Ribeiro, A. L. Chagas Disease An Overview of Clinical and Epidemiological Aspects. *J Am Coll Cardiol* **62**, 767–776 (2013).
64. Bocchi, E. A. *et al.* The reality of heart failure in Latin America. *J Am Coll Cardiol* **62**, 949–958 (2013).
65. Prata, A. Clinical and epidemiological aspects of Chagas disease. *Lancet Infect Dis* **1**, 92–100 (2001).
66. Rassi, A. J., Rassi, A. & Marin-Neto, J. Chagas disease. *Lancet* **375**, 1388–1402 (2010).
67. Cunha-Neto, E. & Chevillard, C. Chagas disease cardiomyopathy: immunopathology and genetics. *Mediat. Inflamm* **2014**, 1–11 (2014).
68. Paula, V. A. *et al.* Prevalence of CD8(+)alpha beta T cells in Trypanosoma cruzi-elicited myocarditis is associated with acquisition of CD62L(Low)LFA-1(High)VLA-4(High) activation phenotype and expression of IFN-gamma-inducible adhesion and chemoattractant molecules. *Microbes Infect* **3**, 971–984 (2001).
69. Pacioretty, L., Barr, S., Han, W. & Gilmour, R. J. Reduction of the transient outward potassium in a canine model of Chagas' disease. *Am J Physiol* **268**, H1258-64 (1995).
70. Roman-Campos, D. *et al.* Changes in cellular contractility and cytokines profile during Trypanosoma cruzi infection in mice. *Basic Res Cardiol* **104**, 19190953 (2009).
71. Roman-Campos, D. *et al.* Cardiomyocyte dysfunction during the chronic phase of Chagas disease. *Mem Inst Oswaldo Cruz* **108**, 243–245 (2013).

72. Roman-Campos, D. *et al.* Novel insights into the development of chagasic cardiomyopathy: Role of PI3Kinase/NO axis. *Int J Cardiol* **167**, 3011–3020 (2013).
73. Machado, C. R. & Ribeiro, A. L. Experimental American trypanomiasis in rats: sympathetic denervation, parasitism and inflammatory process. *Mem Inst Oswaldo Cruz* **84**, 549–556 (1989).
74. Brener, Z., Andrade, Z. A. & Barral-Netto, M. *Trypanosoma cruzi e Doença de Chagas*. Editora Guanabara-Koogan, 2 ed, 2000. (2000).
75. Ribeiro, A. L. & Rocha, M. O. Indeterminate form of Chagas disease: considerations about diagnosis and prognosis. *Rev Soc Bras Med Trop* **31**, 301–314 (1998).
76. Postan, M., Cheever, A. W., Dvorak, J. A. & McDaniel, J. P. A histopathological analysis of the course of myocarditis in C3H/He mice infected with *Trypanosoma cruzi* clone Sylvio-X10/4. *Trans R Soc Trop Med Hyg* **80**, 50–55 (1986).
77. Andrade, Z. A., Andrade, S. G., Oliveira, G. B. & Alonso, D. R. Histopathology of the conducting tissue of the heart in Chagas' myocarditis. *Am Hear. J* **95**, 316–324 (1978).
78. Ribeiro, A. L. *et al.* Electrocardiographic abnormalities in *Trypanosoma cruzi* seropositive and seronegative former blood donors. *PLoS Negl Trop Dis* **7**, e2078 (2013).
79. Maguire, H. *et al.* Cardiac morbidity and mortality due to Chagas' disease: prospective electrocardiographic study of a Brazilian community. *Circulation* **75**, 1140–1145 (1987).
80. Carvalho, A. C. C. De *et al.* Gap junction distribution is altered between cardiac myocytes infected with *Trypanosoma cruzi*. *Circ Res* **70**, 733–742 (1992).
81. Wen, J., Vyatkina, G. & Garg, N. Oxidative damage during chagasic cardiomyopathy development: role of mitochondrial oxidant release and inefficient antioxidant defense. *Free Radic Biol Med* **37**, 1821–1833 (2004).
82. Wen, J. J. & Garg, N. Oxidative modification of mitochondrial respiratory complexes in response to the stress of *Trypanosoma cruzi* infection. *Free Radic Biol Med* **37**, 2072–2081 (2004).
83. Gupta, S. *et al.* *Trypanosoma cruzi* infection disturbs mitochondrial membrane potential and ROS production rate in cardiomyocytes. *Free Radic Biol Med* **47**, 1414–1421 (2009).
84. Paiva, C. N. *et al.* Oxidative stress fuels *Trypanosoma cruzi* infection in mice. *J Clin Invest* **122**, 2531–2542 (2012).
85. Vilar-Pereira, G. *et al.* Resveratrol reverses functional Chagas Heart Disease in mice. *PLoS Pathog* **12**, 1–19 (2016).
86. Massion, P., Feron, O., Dessy, C. & Balligand, J.-L. Nitric oxide and cardiac function: ten years after, and continuing. *Circ Res* **93**, 388–398 (2003).
87. Prosser, B. L., Ward, C. W. & Lederer, W. J. X-ROS Signaling: Rapid Mechano-Chemo Transduction in Heart. *Science* (80-.). **333**, 1440–1445 (2011).

88. Massion, P. & Balligand, J. Modulation of cardiac contraction, relaxation and rate by the endothelial nitric oxide synthase (eNOS): lessons from genetically modified mice. *J Physiol* **546**, 63–75 (2003).
89. Paiva, C., Medei, E. & Bozza, M. ROS and Trypanosoma cruzi: Fuel to infection, poison to the heart. *PLoS Pathog* **14**, e1006928 (2018).
90. Lee, B., Bacon, K., Bottazzi, M. & Hotez, P. Global economic burden of Chagas disease: a computational simulation model. *Lancet Infect Dis* **13**, 342–348 (2013).
91. Jannin, J. & Villa, L. An overview of Chagas disease treatment. *Mem Inst Oswaldo Cruz* **102**, 95–97 (2007).
92. Cruz, J. S. *et al.* Altered Cardiomyocyte Function and Trypanosoma cruzi Persistence in Chagas Disease. *Am J Trop Med Hyg* **94**, 1028–1033 (2016).
93. Waghbi, M. C. *et al.* Gap junction reduction in cardiomyocytes following transforming growth factor- β treatment and Trypanosoma cruzi infection. *Mem Inst Oswaldo Cruz* **104**, 1083–1090 (2009).
94. dos Santos, V. M. *et al.* Functional and histopathological study of the pancreas in hamsters (*Mesocricetus auratus*) infected and reinfected with Trypanosoma cruzi. *Parasitol Res* **94**, 125–133 (2004).
95. Hassan, G. S. *et al.* Trypanosoma cruzi infection induces proliferation of vascular smooth muscle cells. *Infect Immun* **74**, 152–159 (2006).
96. Bouzahzah, B. *et al.* Regulation of host cell cyclin D1 by Trypanosoma cruzi in myoblasts. *Cell Cycle* **7**, 500–3 (2008).
97. Barrias, E. S., Reignault, L. C., Souza, W. De & Carvalho, T. M. Trypanosoma cruzi uses macropinocytosis as an additional entry pathway into mammalian host cell. *Microbes Infect.* **14**, 1340–1351 (2012).
98. Nagajyothi, F. *et al.* Trypanosoma cruzi utilizes the host low density lipoprotein receptor in invasion. *PLoS Negl Trop Dis* **5**, e953 (2011).
99. Prioli, P., Rosenberg, I. & Pereira, M. E. High- and low-density lipoproteins enhance infection of Trypanosoma cruzi in vitro. *Mol Biochem Parasitol* **38**, 191–198 (1990).
100. Johndrow, C., Nelson, R., Tanowitz, H., Weiss, L. M. & Nagajyothi, F. Trypanosoma cruzi infection results in an increase in intracellular cholesterol. *Microbes Infect* **16**, 337–344 (2014).
101. Miles, M. A., Feliciangeli, M. D. & Arias, A. R. De. American trypanosomiasis (Chagas' disease) and the role of molecular epidemiology in guiding control strategies. *BMJ* **326**, 1444–1448 (2003).
102. Campbell, D. A., Westenberger, S. J. & Sturm, N. R. The determinants of Chagas disease: connecting parasite and host genetics. *Curr Mol Med* **4**, 549–562 (2004).
103. Keusch, G. T. & Farthing, M. J. G. Nutrition and infection. *Annu Rev Nutr* **6**, (1986).
104. Yaeger, R. G. & Miller, O. N. Effect of Lysine Deficiency on Chagas' Disease

- in Laboratory Rats. *J Nutr* **81**, 169–174 (1963).
105. Carlomagno, M. A., Riarte, A., Moreno, M. & Segura, E. L. Effects of calorie restriction on the course of *Trypanosoma cruzi* infection. *Nutr. Res* **7**, 1031–1040 (1987).
 106. Cintra, I. P. *et al.* Influence of dietary protein content on *Trypanosoma cruzi* infection in germfree and conventional mice. *Rev Inst Med Trop Sao Paulo* **40**, 355–362. (1998).
 107. Geraix, J., Ardisson, L. P., Marcondes-Machado, J. & Pereira, P. C. Clinical and nutritional profile of individuals with Chagas disease. *Braz J Infect Dis* **11**, 411–414 (2007).
 108. Acquatella, H. Echocardiography in Chagas heart disease. *Circulation* **115**, 1124–1131 (2007).
 109. Marin Neto, J. A., Simões, M. V & Sarabanda, A. V. Chagas' heart disease. *Arq Bras Cardiol* **72**, 247–280 (1999).
 110. Marin-Neto, J. A., Rassi, A. J., Maciel, B. C., Simões, M. V & Schmidt, A. Chagas heart disease. In: Yusuf S, Cairns JA, Camm AJ, Fallen EL, Gersh BJ, eds. *Evidence-based cardiology, 3rd edn.* London: BMJ Books. (2010).
 111. Rassi, A. J., Rassi, A. & Little, W. C. Chagas' heart disease. *Clin Cardiol* **23**, 883–889 (2000).
 112. Rassi, A., Rassi, A. J. & Rassi, S. G. *Doença de Chagas.* In: Lopes AC, ed. *Tratado de clínica médica, 2nd edn.* São Paulo: Editora Roca. (2009).
 113. Bern, C. Antitrypanosomal therapy for chronic Chagas' disease. *N Engl J Med* **364**, 2527–2534 (2011).
 114. Bermudez, J., Davies, C., Simonazzi, A., Real, J. P. & Palma, S. Current drug therapy and pharmaceutical challenges for Chagas disease. *Acta Trop* **156**, 1–16 (2016).
 115. Rodrigues, C. J. & de Castro, S. L. A critical review on Chagas disease chemotherapy. *Mem Inst Oswaldo Cruz* **97**, 3–24 (2002).
 116. Krell, M. J. *et al.* Intermittent, ambulatory dobutamine infusions in patients with severe congestive heart failure. *Am Hear. J* **112**, 787–791 (1986).
 117. Santiago, H. *et al.* NADPH phagocyte oxidase knockout mice control *Trypanosoma cruzi* proliferation, but develop circulatory collapse and succumb to infection. *PLoS Negl Trop Dis* **6**, e1492 (2012).
 118. Esper, L. *et al.* Role of SOCS2 in modulating heart damage and function in a murine model of acute Chagas disease. *Am J Pathol* **181**, 130–140 (2012).
 119. Macedo, A. M., Machado, C. R., Oliveira, R. P. & Pena, S. D. *Trypanosoma cruzi*: genetic structure of populations and relevance of genetic variability to the pathogenesis of chagas disease. *Mem Inst Oswaldo Cruz* **99**, 1–12 (2004).
 120. Souza, A. P. De *et al.* The benefits of using selenium in the treatment of Chagas disease : prevention of right ventricle chamber dilatation and reversion of *Trypanosoma cruzi* -induced acute and chronic cardiomyopathy in mice. *Mem*

Inst Oswaldo Cruz **105**, 746–751 (2010).

121. Chen, G. *et al.* Cardioprotective actions of verapamil on the beta-adrenergic receptor complex in acute canine Chagas' disease. *J Mol Cell Cardiol* **28**, 931–941 (1996).
122. Vyatkina, G., Bhatia, V., Gerstner, A., Papaconstantinou, J. & Garg, N. Impaired mitochondrial respiratory chain and bioenergetics during chagasic cardiomyopathy Impaired mitochondrial respiratory chain and bioenergetics during chagasic cardiomyopathy development. *Biochim Biophys Acta* **1689**, 162–173 (2004).
123. Dhiman, M. & Garg, N. J. NADPH oxidase inhibition ameliorates Trypanosoma cruzi- induced myocarditis during Chagas disease. *J Pathol* **225**, 583–596 (2011).
124. Wen, J. *et al.* Phenyl-alpha-tert-butyl-nitron and benzonidazole treatment controlled the mitochondrial oxidative stress and evolution of cardiomyopathy in chronic chagasic Rats. *J Am Coll Cardiol* **55**, 2499–2508 (2010).
125. Erickson, J. R., He, B. J., Grumbach, I. M. & Anderson, M. E. CaMKII in the cardiovascular system: sensing redox states. *Physiol Rev* **91**, 889–915 (2011).
126. Kanagaratnam, P., Rothery, S., Patel, P., Severs, N. J. & Peters, N. S. Relative Expression of Immunolocalized Connexins 40 and 43 Correlates With Human Atrial Conduction Properties. *J. Am. Coll. Cardiol.* **39**, 116–123 (2002).
127. Adesse, D. *et al.* *Gap junctions and chagas disease. Chagas Disease* **76**, (Elsevier Ltd., 2011).
128. Nagajyothi, F. *et al.* Trypanosoma cruzi infection of cultured adipocytes results in an inflammatory phenotype. *Obes. (Silver Spring)* **16**, 1992–7 (2008).
129. Nagajyothi, F. *et al.* High fat diet modulates Trypanosoma cruzi infection associated myocarditis. *PLoS Negl Trop Dis* **8**, e3118 (2014).